THE UNIVERSITY OF CHICAGO

METAL-ORGANIC FRAMEWORKS FOR ENERGY APPLICATIONS

A DISSERTATION SUBMITTED TO
THE FACULTY OF THE DIVISION OF THE PHYSICAL SCIENCES
IN CANDIDACY FOR THE DEGREE OF
DOCTOR OF PHILOSOPHY

DEPARTMENT OF CHEMISTRY

BY
DANIEL MICHERONI

CHICAGO, ILLINOIS
JUNE 2019

TABLE OF CONTENTS

LIST OF TABLES

LIST OF FIGURES

LIST OF SCHEMES

LIST OF ABBREVIATIONS

1-D	One Dimensional
2-D	Two Dimensional
3-D	Three Dimensional
˚C	Degrees Celsius
Å	Angstrom
ΔR	Change in Scattering Half-Path Length
σ^2	Mean Standard Relative Deviation of a Scatter
AFM	Atomic Force Microscopy
ACN	Acetonitrile
BET	Borne-Emmett-Teller Theory
bpy	2,2'-bipyridine
CNTs	Carbon Nanotubes
CV	Cyclic Voltammetry
DDQ	2,3-dichloro-5,6-dicyano-1,4benzoquinone
DFT	Density Functional Theory
EXAFS	Extended X-ray Absorption Fine Structure
eV	Electronvolt

F.E	Faradaic Efficiency
GC	Gas Chromatography
GCE	Glassy Carbon Electrode
H_2DBP	5, 15-di(*p*-benzoato)porphyrin
H_2DPDBP	5,15-di(*p*-benzoato)-10,20-diphenyl-porphyrin
H_3TPY	4'-(4-carboxyphenyl)-[2,2':6',2"-terpyridin]-4'-yl)-5,5"-dicarboxylic acid
HER	Hydrogen Evolution Reaction
^{1}H-NMR	Proton Nuclear Magnetic Resonance
HOMO	Highest Occupied Molecular Orbital
ICP-MS	Inductively Coupled Mass Spectrometry
ISC	Inter-System Crossing
LUMO	Lowest Occupied Molecular Orbital
Me_2DBP	5,15-di(p-methyl-benzoato)porphyrin
Me_2DPDBP	5,15-di(*p*-methyl-benzoato)-10,20-diphenyl-porphyrin
^{1}MLCT	Singlet Metal-to-Ligand Charge Transfer
^{3}MLCT	Triplet Metal-to-Ligand Charge Transfer
MOF	Metal-Organic Framework
MOL	metal-organic layer

NHE	Normal Hydrogen Electrode
OER	Oxygen Evolution Reaction
PCET	Proton Coupled Electron Transfer
Photo-XTAL	Photo-X-Ray Crystallography
PL	Photoluminescence
PSM	Post-Synthetic Modification
PXRD	Powder X-Ray Diffraction
py	pyridine
RDE	Rotating Disc Electrode
SBU	Secondary Building Unit
TEA	Triethylammine
TEM	Transmission Electron Microscopy
TFA	Trifluoroacetic Acid
TGA	Thermogravimetric Analysis
TON	Turnover Number
TOF	Turnover Frequency
tpy	terpyridine
UV-VIS	Ultraviolet and Visible

XANES	X-ray Absorption Near Edge Structure

ABSTRACT

Daniel Micheroni: Metal-Organic Frameworks for Solar Energy Applications

Under the Direction of Professor Wenbin Lin

This dissertation presents the photochemical (Chapter 2), electrochemical (Chapters 3, 5), and photophysical (Chapter 4) properties of light harvesting and catalytic molecules incorporated into metal-organic frameworks (MOFs). Chapter 1 presents an overview of the goals, purposes, and background materials for the subsequent chapters. Chapter 2 reports cobalt-porphyrin moieties incorporated into two MOF architectures and their catalytic activities for photochemical hydrogen production in an aqueous media. By inserting zinc and cobalt ions into the porphyrin centers to serve as the photosensitizer and catalyst respectively, MOFs capable of hydrogen generation were developed within a single material without the need of a separate co-catalyst. The resulting assemblies give TONs as high as 75 after five hours irradiation in an acidic medium through a putative Co(III)-H intermediate, outperforming their homogenous counterparts by up to 15 times.

Chapter 3 presents electrocatalytic proton reduction with Hf_{12}-porphyrin MOFs covalently tethered to carbon nanotubes (CNTs). Covalent attachment of the MOF nanoplates to conductive CNTs improves electron transfer from the electrode to the Co-porphyrin active sites, leading to effective proton reduction. The Hf_{12}-CoDBP/CNT assembly afforded a turnover number of 32,000 in 30 minutes with an average turnover frequency of 17.7 s^{-1}, placing it among the most active Co-based molecular catalysts.

Chapter 4 describes the photophysical and photochemical properties of a $[Ru(bpy)_2(py)_2]^{2+}$ complex confined within a zinc-oxalate MOF (Ru@MOF). The MOF perfectly encapsulates $[Ru(bpy)_2(py)_2]^{2+}$ complexes, thereby altering their vibrational and electronic states through sterics and by removing the effects of solvents. As a result, the photoluminescence lifetime and quantum

yield of the material significantly increase, likely through the destabilization the dd-state. The photochemical stability of $[Ru(bpy)_2(py)_2]^{2+}$ in Ru@MOF also significantly increases due to the shutdown of photosubstitution processes. This stability can be leveraged into further studies including transient absorption and photocrystallography among other spectroscopic techniques.

Chapter 5 describes the incorporation of a precious metal free cobalt-terpyridine catalyst into two-dimensional metal organic layers (MOLs) for hydrogen production in acidic media. The Co-TPY MOL effectively stabilizes ultrasmall cobalt nanoparticles for hydrogen production with TOFs as high as 4300 hr^{-1} in pH=1 at a low overpotential of 715 mV.

ACKNOWLEDGEMENTS

I would like to thank my advisor, Professor Wenbin Lin, for his support and guidance during my graduate career. Meeting with Professor Lin as a first year, I remember his enthusiasm for his science and the broad and inherent utility I saw in all his work. His passion and pragmatism led me to joining his lab. Five years later and nothing has changed. His passion is unwavering and he remains a constant bedrock in my academic progress. His continued pursuit of excellence has fostered my growth as a scientist, forcing me to analyze, ask questions, and move outside of my comfort zone within the realm of my projects. I am grateful for his experience and aid throughout my journey.

I would like to thank my committee, Professors Dmitri Talapin and John Anderson. Both of you are tremendous scientists and citizens of the University of Chicago Chemistry Department. It has been an honor to work with you both and to have you on my defense committee.

Though our lab remains broad in scope, I would like to thank all group members past and present in my research. None of this work would have been possible without you as you played important roles in discussion, mentorship, synthesis, and analytical methods for all my projects. I would like to especially thank Dr. Teng Zhang, Dr. Kuangda Lu, Dr. Xin Zhou, Dr. Zekai Lin, Dr. Nathan Thacker, Dr. Chris Poon, Dr. Carter Abney, Dr. Yuanyuan Zhu, Guangxu Lan, Dr. Pengfei Ji, Marek Piechowitz, Kaiyuan Ni, Christina Chan, and Wenbo Han. Each of these individuals helped me succeed by contributing directly and indirectly to all my research.

I would also like to thank the support staff here at the University of Chicago, particularly Dr. Alex Filatov, Dr. Justin Jureller, and Dr. Antoni Jurkowitz. Your assistance here was vital as I would be woefully inept at using any of the facilities without you. Outside of UChicago, I would

like to express my gratitude to Dr. Yusheng Chen at Argonne National Labs as well, whose x-ray crystallographic expertise was necessary for many of my projects.

To my friends here at the University of Chicago, especially those in my graduate year, thank you. You made my life here not just bearable but wonderful. I love the culture we built and the fun that we had in and out of the confines of GCIS and Searle.

Most importantly, I would like to thank my family, though none of you have visited me outside of James as I write this paragraph. To my parents, Vinny and Diane, you have been supportive of me as only parents can throughout my entire life, in and out of academics. You provided me with love, encouragement, and freedom, allowing me to make my own choices and explore my own avenues. This work is a culmination of everything you have taught me throughout my life. To my siblings James and Nicole, I have learned my entire life from you both as the youngest child. Your lives have served as a wonderful example for me as I grew. Thank you all for always being there for me.

CHAPTER 1

Introduction

Energy is the bedrock of civilization. The transformation and storage of energy drive innovation and maintain our quality of life. Presently, fossil fuels dominate the energy supplies due to their high energy density and availability. However, oil, gas, and coal are finite and come with the cost of releasing greenhouse and toxic gases into the atmosphere upon their combustion, which can have major impacts on climate and environment as well as detrimental effects to our health.[1, 2] As a result, scientists and engineers are working to create materials which can use readily available and innocuous energy sources in closed loops to store and transform energy. Primarily, these renewable energy sources are sunlight, wind, and water. The development and understanding of functional materials to drive or assist in water splitting to form hydrogen, whether actuated by sunlight or electrical bias is the primary focus of my graduate work.

1.1. Current Energy Landscape

In 2017 the United States consumed 103.08 x 10^{15} kJ of energy. Of this, nearly 80% of energy consumption came from fossil fuels with 37%, 29%, and 14% from petroleum, natural gas, and coal, respectively.[3] This roughly 80 quadrillion kJ of energy results in the release of 6.5 x 10^{9} metric tons of carbon dioxide.[4] As a direct result of burning fossil fuels, the concentration of carbon dioxide in the atmosphere has reached 405 parts per million (ppm) in 2017, up from 330 ppm in 1975. This inauspicious trend has been estimated to cause 6.5 million premature deaths globally (11.5 % of all premature deaths)[5] and is as predicted to cause billions of dollars of economic damage in the near future.[1]

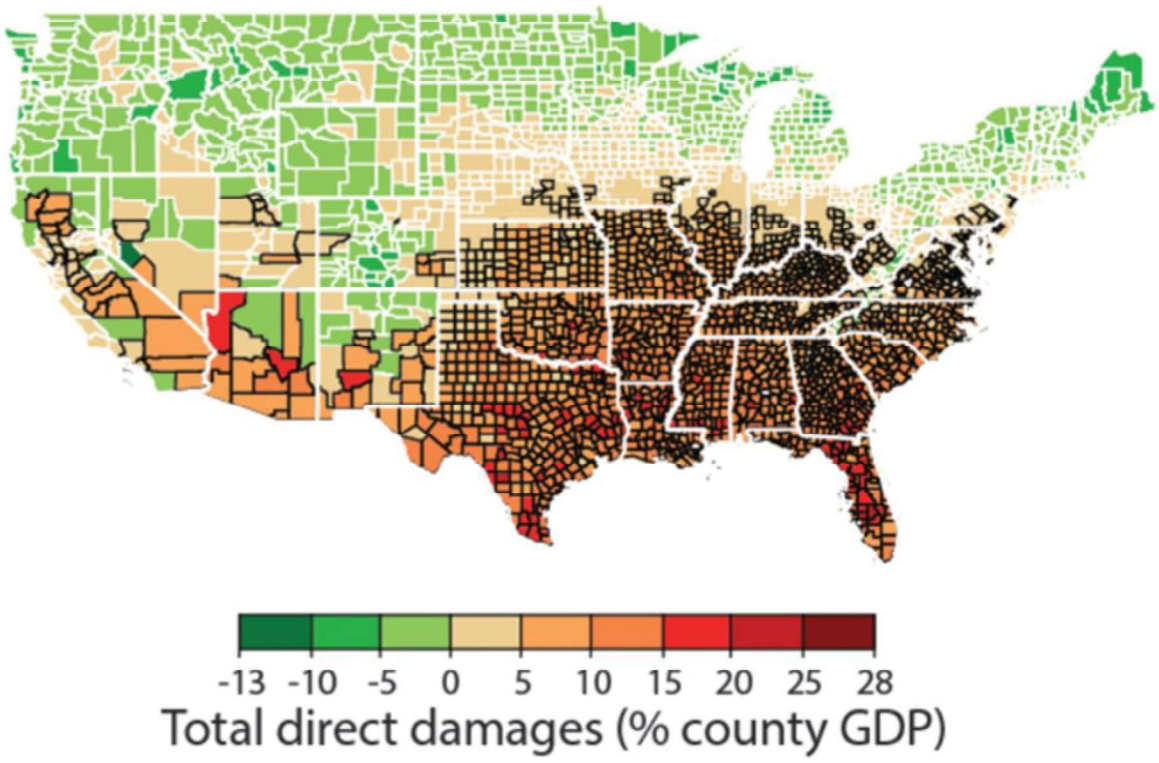

Figure 1-1. The projected total economic impact of climate change in 2099 relative to predictions with no additional climate impact trajectories. Factors include projected agricultural yields, mortality rates, coastal damage, and energy expenditures among others. Used with permission from the *Science* **2017**, *356*, 1362. Copyright 2017 American Association for the Advancement of Science.

These large numbers beg the question, why is US energy policy committed to fossil fuels? The quickest answer is that technological breakthroughs to make alternative energy economically competitive with fossil fuels do not yet exist. To overtake fossil fuels, a clean energy technology must be energy dense, safe, widely available, scalable, and be compatible with present infrastructures. Solar and wind technologies at present work outside the current energy grid, rely on intermittent weather patterns, and require scalable energy storage solutions to be developed. Both presently provide no solution to supplanting half of fossil fuel production in heavy industries and transportation such as concrete, shipping, and aviation. The input energy source is just too diffuse. A hydrogen economy can solve many of these problems, but still needs breakthroughs in

its production, its associate technologies including fuel cells, and its transport as liquid fuels. No one technology can overcome all of these problems, however, a hydrogen economy is still worth pursuing because it is clean, energy dense, and scalable in theory. It is for this reason that I developed chemical systems with the goal to improve and study hydrogen production in this thesis.

1.2 The Water Splitting Reaction

The water splitting reaction has garnered interest because of its ability to produce hydrogen. Hydrogen is a clean burning and energy dense material which can be burned directly to form water, reacted with carbon dioxide to produce liquid organic fuels, or used directly in fuel cells. [6] The water splitting reaction is a simple but difficult to achieve reaction consisting of two halves as defined below.

$$2H^+ + 2e^- \rightarrow H_2(g) \qquad E^0 = 0.00\ kJ\ mol^{-1}$$

$$H_2O \rightarrow \frac{1}{2}O_2(g) + 2H^+ + 2e^- \qquad E^0 = 227.35\ kJ\ mol^{-1}$$

$$H_2O \rightarrow H_2(g) + \tfrac{1}{2}O_2(g) \qquad E^0_{cell} = -237.35\ kJ\ mol^{-1}$$

Being an uphill reaction with a $\Delta G^0 = 237.35\ kJ/mol$, the reaction must be energetically driven by sustainable methods for it to be commercially viable. This can be achieved either by electrolysis via a renewable sources like hydroelectric power and solar cells or it must be converted directly by sunlight via a photocatalytic system.[7] Electrolysis of water is an old method with its origins dating back to 1800 as discovered by Nicholson and Carlisle. [8] Since then, the field has been expanded upon by developing and improving catalysts to increase efficiency, to lower cost, and to increase the lifetime of the material. The most important parameters for determining the quality of electrocatlysts are overpotential, Faradaic efficiency, and current density. Overpotential is defined as the increase in potential that must be applied for the reaction to take place above the

thermodynamic limit. It is a result of increased resistance and the production of heat during electrolysis. Faradaic efficiency (F.E.) is a measure of the percent of electrons that carry out the desired reactions as described in Equation 1.1 where n is the number of electrons transferred in the reaction, f is Faraday's constant, Q is the moles of product produced, and C is the charge transferred during electrolysis. A decrease in Faradaic efficiency is a result of competing reactions and a lack of selectivity by the catalytic species. Current density is defined as the current transferred per cm^2 of the electrode at a given potential.[9] It is limited by diffusion, either by the catalyst and or the reactant, to the electrode surface and the reactivity of the catalyst for the desired reaction. Unfortunately, the materials that achieve the best results within these metrics are usually comprised of precious metals including platinum,[10-13] ruthenium,[14-17] and iridium[18-21] making their implementation prohibitively expensive and unrealistic. As a result, there has been a strong incentive to create materials which are metal-free or comprised of Earth-abundant metals such as cobalt,[22-27] iron,[28-31] and nickel.[32-34] However, most materials developed can only perform a single half of the water splitting reaction and nearly all materials have inefficiencies as a result of charge recombination. Because of back electron transfer and charge recombination, sacrificial agents, in the case of half reactions, and electron/hole relays, in the case of total water splitting, are often employed to mitigate this phenomenon

$$F.E = \frac{nfQ}{C} * 100\% \qquad \textbf{1-1}$$

Photocatalytic hydrogen production was first reported by Fujishima in 1972. [35] Good photocatalysts should all have the same energetic profile; the energy level of the LUMO or conduction band must be higher in energy than the cathodic reaction while the energy level of the HOMO or valence band must be lower in energy than the anodic reaction so electron transfer can occur downhill in an energetically favorable manner (Figure 1-2). In terms of efficacy, a good

photocatalyst is measured by its turnover number (TON) and its turnover frequency (TOF). TON is defined as the moles of product produced per mole of active catalyst and TOF is defined as TON per unit time.

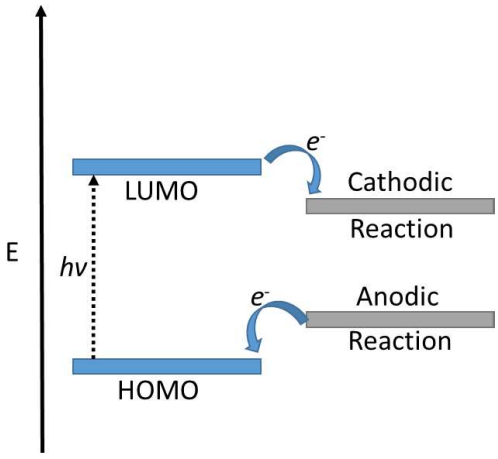

Figure 1-2. A simple schematic for photocatalytic processes.

1.3 Photocatalytic Systems

The absorption of sunlight by a molecule to achieve an excited state capable of work is of the utmost importance for photocatalysis, artificial photosynthesis, and dye sensitized solar cells. Photocatalytic systems require at least three major steps to achieve functionality: absorption of light by a photosensitizer (PS) to create an electron-hole pair, charge migration to the catalyst, and catalysis to form the desired product (Figure 1-3).[36] Molecular photosensitizers are either based on highly conjugated organic dyes or transition metal complexes. For transition metal photosensitizers, the metal is usually bound to an imine or diimine such as pyridine or bipyridine (bpy), as shown by numerous works in the field, specifically those containing ruthenium or iridium as a transition metal.[17, 18, 37-40] In addition to diimines, porphyrins are a common molecular based photosensitizer which can accommodate numerous transition metals, including first row transition metals, to alter its redox chemistry. The best photosensitizers of these metal-ligand complexes

have strong absorbances in visible or ultra-violet spectra due to symmetry-allowed singlet metal-to-ligand charge transfer (^{1}MLCT) or a mixing of MLCT and ligand-to-ligand charge transfer (Figure 1-4). The resulting excited states then probabilistically undergo inter-system crossing (ISC) to a long lived triplet metal-to-ligand charge transfers (^{3}MLCT) excited state due to the heavy atom effect enhanced by the transition metal center.[41] The triplet state improves the effectiveness of redox reactions by increasing the distance travelled and probability for both inter- and intramolecular charge transfer due to the long lived excited state lifetime.

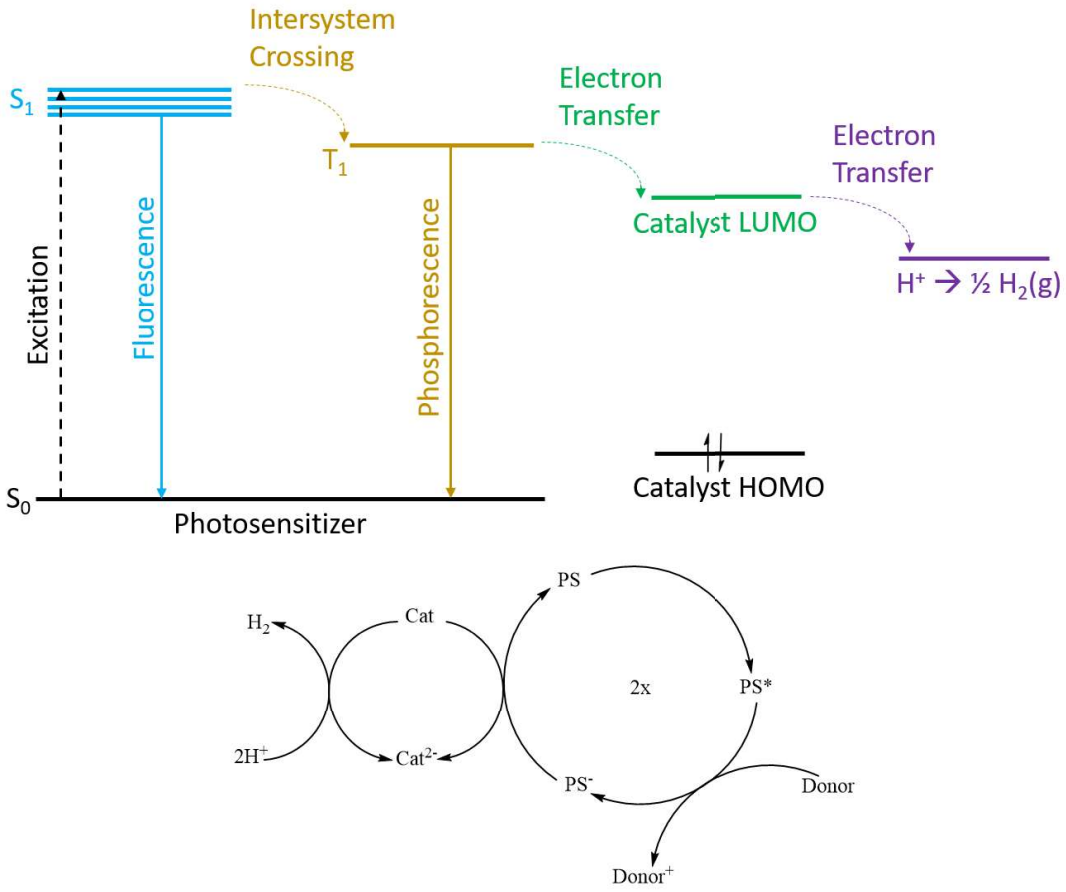

Figure 1-3. A simplified Jablonski diagram showing the energetic pathway for photocatalytic systems from absorption of light to the catalytic reaction. (Top). A generalized mechanistic pathway for the production of hydrogen using a photocatalytic system (bottom).

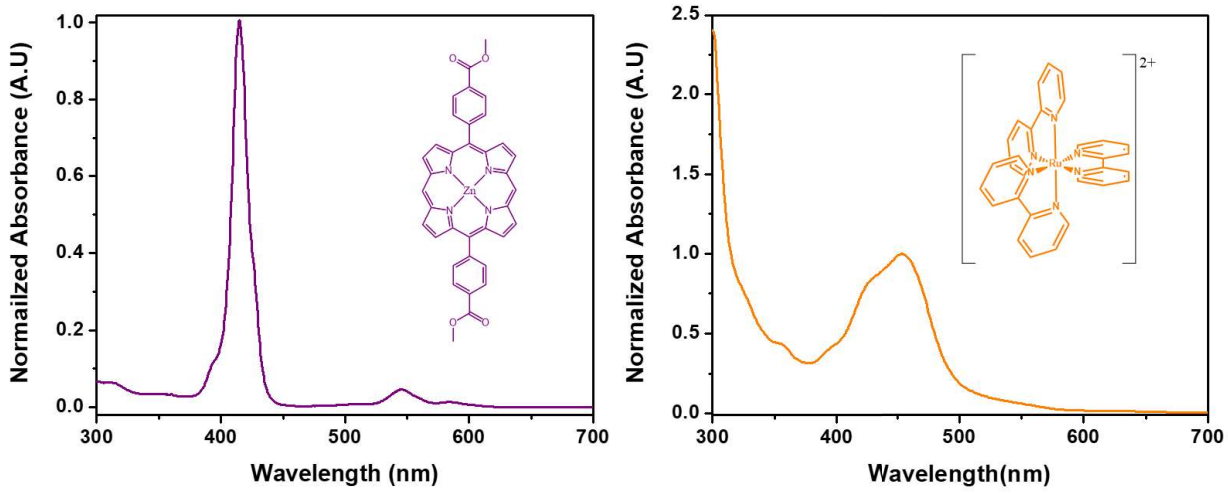

Figure 1-4. The UV-Vis spectra and structure of the two major classes of photosensitizer in this work: Zn-porphyrins (left) and ruthenium tris-bipyridine (right).

The use of light as driving force in photocatalytic systems allows for the production of thermodynamically uphill products inaccessible to most catalytic systems. The reduction potentials of excited states are governed by equations 1.2 and 1.3 making them significantly easier to reduce or oxidize than their ground state counterparts. This allows for highly reducing states to be accessed within the photosensitizer to drive the overall reaction.

$$E(PS^{+}/PS^{*}) = E^{0}(PS^{+}/PS) - E_{hv} \qquad \textbf{1.2}$$

$$E(PS^{*}/PS^{-}) = E^{0}(PS/PS^{-}) + E_{hv} \qquad \textbf{1.3}$$

However, the photocatalytic system's efficiency is often limited by fluorescence and phosphorescence from the excited state as well as back electron transfer between the active catalyst and photosensitizer. As a result, a sacrificial electron donor is generally incorporated into the

system to drive the reaction forward, as electron injection into the hole of the photosensitizer prevents radiative recombination as well as prevents the photosensitizer from entering its highly oxidative PS^+ state.

1.4 Electrocatalytic systems

Electrocatalytic systems complement photocatalytic systems very well for driving uphill chemical reactions, including those for energy purposes. By using electrical bias as its driving force, electrocatalytic systems do not inherently require light. In terms of truly green chemical prospects, this has a few distinct advantages compared to their photochemical counterparts: there is no need to concentrate diffuse solar radiation, photochemical degradation is removed, and the overall efficiency of the system is generally improved. The improvement in efficiency is the most attractive aspect of electrocatalytic systems as many materials can achieve high Faradaic efficiencies of close to 100% while the ratio of photons absorbed to electrons transferred in photosensitizers is usually at least one order of magnitude less.

Despite these advantages, molecular based electrocatalysts for alternate energy applications are often hindered by a small available surface area of the electrode, poor aqueous stability, high overpotential, and slow diffusion. Strictly inorganic materials are often examined to solve these problems as their overpotentials are lower and their stability is better than molecular species, however, they are often developed from precious metals like platinum, iridium, and ruthenium. Therefore, the need for electrocatalytic systems based on Earth-abundant metals is strong. Molecular materials provide a unique platform to fill this gap due to their ability to incorporate a bevy of cheaper metal centers and tune their reduction potentials by the attachment of simple electron donating or withdrawing groups.

In molecular species, the mechanism for the HER is less clear than that of heterogeneous species which often proceed via absorption of protons onto the electrode, reduction of hydrogen atoms to form H_2, and desorption of hydrogen. Instead, homogenous systems can achieve hydrogen production with the combination of two proton transfers, two electron transfers, or one of each with proton coupled electron transfer (PCET) in any order. Furthermore, the difficulty of ascertaining the exact mechanism is exacerbated by the ability for homogenous materials to form bimolecular assemblies. The ability to site-isolate the metal centers by restricting their degrees of freedom or through the use of bulky protecting groups coupled with rigorous electrochemical studies is often employed to determine the mechanism.

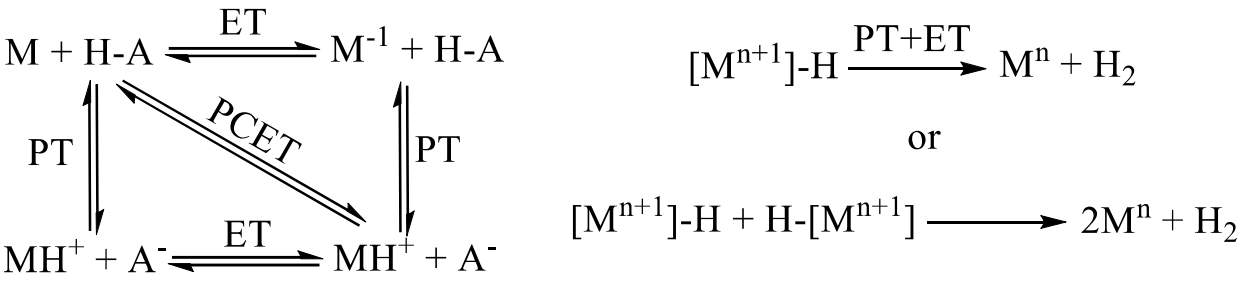

Scheme 1-1. The possible pathways a homogenous complex (M) can undertake to reach a metal-hydride intermediate in an electrochemical process (left). From this intermediate, hydrogen can be evolved from a single metal center in the hemolytic pathway or from two metal-hydride intermediates in the bimolecular pathway (right).

1.5 Metal-Organic Frameworks

The first examples of metal-organic frameworks (MOFs) or coordination polymers date back to the 1950's, however, due to limitations of the characterization techniques available then, specifically x-ray crystallography, their unique properties remained unexamined. [42-44] It was not until 1980's when Robson and coworkers synthesized and analyzed a series of coordination

polymers constructed from copper and cyano ligands that MOFs began to be studied and its applications explored. [45, 46]

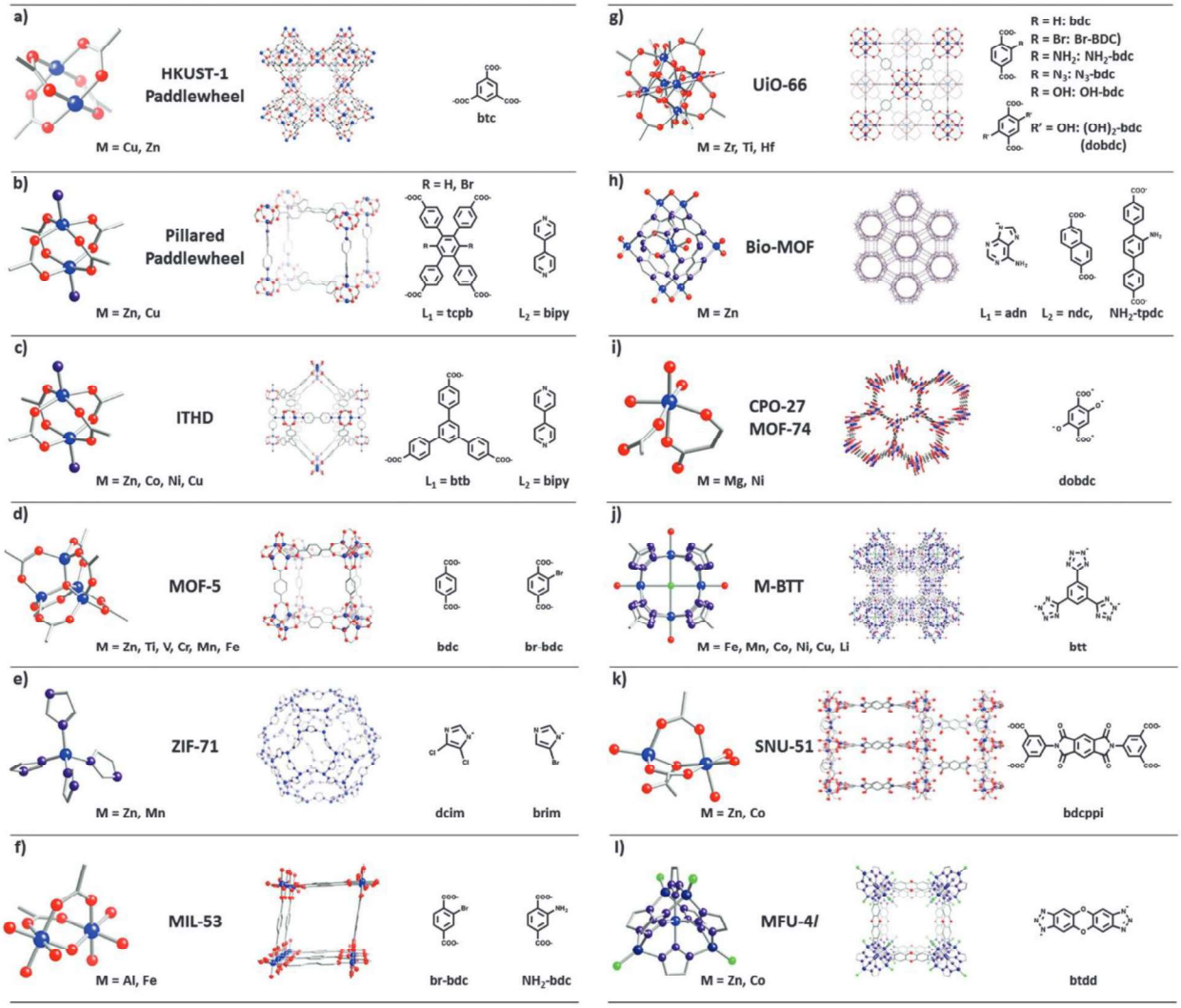

Figure 1-5. SBUs (left), lattice structures (middle), and linkers (right) of various classes of MOFs highlight the diversity of the field and its numerous permutations. Atom color designations are: carbon – grey, nitrogen- purple, oxygen – red, metal – blue, and chlorine – green. Used with permission from the *Chem. Soc. Rev*. **2014**, *43*, 5896. Copyright 2014 the Royal Society of Chemistry.

MOFs refer to porous inorganic/organic hybrid materials comprised of metal or metal cluster nodes also referred to as secondary building units (SBUs) bound to organic linkers to form 1-, 2-,

or 3-dimensional crystalline networks. The fixed geometry of the SBUs coupled with the symmetrical binding motifs of the organic linkers gives rise to MOFs most prominent properties: their porosity and their crystallinity. The high porosity and surface-area of MOFs make them ideal candidates for numerous chemical applications while their crystallinity allows for facile determination of structure function relationships through X-ray characterization methods. However, what truly makes MOFs interesting is their versatility and predictability. The bevy of available metals, organic linkers, and reaction conditions leads to countless permutations and geometries which can be optimized for specific applications. The geometries can be reasonably predicted based upon SBU geometrical precedent independent of the choice of linker assuming the linkers are of the same symmetry. This is referred to as reticular synthesis. Reticular synthesis is a wonderful tool because it allows for specific engineering of the material. The linker is usually chosen with specific functionalities in mind and can be directly installed or can be chemically modified through post-synthetic modification (PSM) of the MOF species to achieve the desired functionality. [47] Because of these features, MOFs have been studied and designed for potential applications in chemical sensing,[48, 49] non-linear optics, gas-storage,[50-52] solar-energy conversion,[53-55] catalysis,[56-59] chemical separation,[60, 61] and drug delivery.[62-64]

The SBU organic linker bond is only of moderate strength as it results from modest Lewis acid Lewis base interactions. As a result, long term stability, particularly in aqueous environments, are usually lacking for MOF materials and limits their applications. The first MOF to show very good stability in aqueous environments was the UiO family of MOFs pioneered by Lillerud and coworkers.[65] The UiO MOF is comprised of $Zr_6O_4(OH)_4(RCO_2)_{12}$ SBUs where the R-group is linear dicarboxylate bridging ligands. The UiO family of MOFs owes its stability to the strong Lewis-acid Lewis-base interaction between the electronic deficient Zr^{4+} metals and the carboxylic

acid. Since this discovery, numerous other SBUs with strong Lewis-Acid base interactions based on Group 4 metals with the coordination environment M_6, M_8, or M_{12} (where M = Zr, Hf, and Ti) have been developed. All show good water stability with slightly different geometries and pore sizes making each suitable for varying applications.

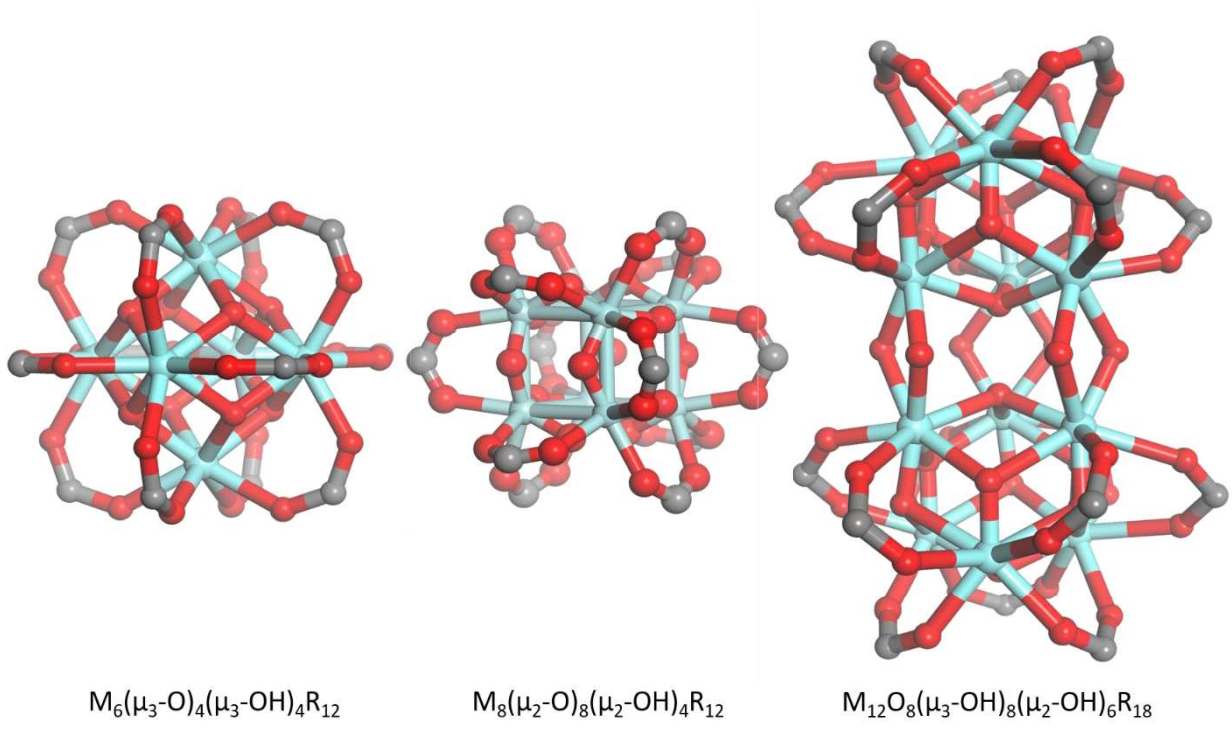

Figure 1-6. The structure model of Group 4 metal containing SBUs, shown here with zirconium as its metal; red- oxygen, grey- carbon, cyan – zirconium

The unique properties of MOFs have made them ideal platforms to study photophysical phenomena. When photophores are used as the bridging ligands in MOFs, the dense packing of chromophores in an organized arrangements resembles that of the chloroplast assemblies in green plants needed to achieve photosynthesis.[66] Because the distance and orientation of chromophores to each other is known in MOFs, MOFs have been utilized as a platform to study short and long range energy transfer phenomenon.[67-69] From these studies it can be seen that both Forster type

and Dexter type energy transfer are significant pathways in porphyrin as well as metal bipyridyl based MOFs through photoluminescent lifetime measurements in the presence of known densities of quenchers installed in the lattice and from theoretical models.

Additionally, the versatility of MOFs allows them to serve as platforms to carry out the hydrogen evolution reaction (HER), oxygen evolution reaction (OER), and carbon dioxide reduction. Despite the fact that the ligands within the MOF framework are close enough together to interact and often exhibit strong and broad absorption spectra over traditional bandgap values, typical MOFs are not semiconductors. The metal SBU bond is inherently insulating and the ligands, though close enough to interact, do not exhibit strong orbital-orbital overlap and can be viewed as isolated systems. Instead, the ability of a MOF to perform photocatalytic reactions depends on the reduction potential of the ligand in the excited state as well as the necessary geometry to facilitate electron and energy transfer. When these properties are met, MOFs can be very successful photocatalysts. Their high porosity and open channels within MOFs allow the diffusion of substrates to reactive centers within the lattice. Furthermore, catalytic centers can be integrated into either the SBUs or the metal centers in MOFs, which allows MOFs to serve as single platform capable of both light harvesting and catalysis for both the HER [70-72], OER [55, 73, 74], and CO_2 reduction.[53, 75, 76]

1.6 Scope of my Thesis

My graduate studies have focused primarily on the design of MOF materials for solar energy applications. I have developed MOFs to serve as photo and electro-catalysts for the hydrogen evolution reaction in acidic media using relatively simple inorganic ligands as my active catalysts such as porphyrin, bipyridine, and terpyridine. Furthermore, the unique ability of MOFs to

physically anchor substrates in repeatable and static physical environments, has allowed me to study their fundamental photophysical and catalytic properties.

Chapter 2 encompasses the use of three highly stable porphyrin-based zirconium MOFs for photocatalytic proton reduction. This system is free of precious metals and shows hydrogen production activity greater than that of the homogenous samples. This is a result of the proximal nature of the photosensitizer and ligand in the MOF material.

Chapter 3 will use a Hf-derived porphyrin MOF as an electrocatalyst for proton reduction in water. The material's catalytic properties are enhanced through covalent tethering to carbon nanotubes (CNTs), forming a unique heterostructure which improves conductivity and available surface area of the MOF/electrode assembly.

Chapter 4 will explore the photophysical properties of a photolabile ruthenium complex trapped within the confines of a metal-organic framework. The tightfitting network perfectly encompasses the ruthenium complex, providing a solvent free environment with imposed physical rigidity. This confinement improves the luminescent properties the ruthenium complex and prevents photosubstitution issues that are observed in the homogenous complex.

Chapter 5 will use a single-layer terpyridine and bipyridne MOLs as an electrocatalyst for proton reduction in water. The metal center was found to be labile in acid media, leading to reduction of the metal centers to form ultrasmall nanoparticles. The agglomeration of the nanoparticles is inhibited by the MOL as a physical barrier and likely due to the sigma-donating properties of the imine functionality. The resultant ultrasmall metal nanoparticles are in close proximity to the electrode surface and highly active for proton reduction.

1.7 References

1. Hsiang, S.; Kopp, R.; Jina, A.; Rising, J.; Delgado, M.; Mohan, S.; Rasmussen, D. J.; Muir-Wood, R.; Wilson, P.; Oppenheimer, M.; Larsen, K.; Houser, T., Estimating economic damage from climate change in the United States. *Science (Washington, DC, U. S.)* **2017,** *356* (6345), 1362-1369.

2. Kampa, M.; Castanas, E., Human health effects of air pollution. *Environ. Pollut. (Amsterdam, Neth.)* **2008,** *151* (2), 362-367.

3. Monthly Energy Review, April 2018. US Energy Information Association: 2018.

4. Blunden, J.; Arndt, D. S.; Hartfield, G., State of the Climate in 2017. Bull. Amer. Meteor. Soc., 2017; Vol. 99, pp Si-S332.

5. Landrigan Philip, J.; Fuller, R.; Hanrahan, D.; Sandilya, K.; Acosta Nereus, J. R.; Adeyi, O.; Arnold, R.; Basu Niladri, N.; Balde Abdoulaye, B.; Bertollini, R.; Bose-O'Reilly, S.; Boufford Jo, I.; Breysse Patrick, N.; Chiles, T.; Mahidol, C.; Coll-Seck Awa, M.; Cropper Maureen, L.; Fobil, J.; Fuster, V.; Greenstone, M.; Haines, A.; Hunter, D.; Khare, M.; Krupnick, A.; Lanphear, B.; Lohani, B.; Martin, K.; Mathiasen Karen, V.; McTeer Maureen, A.; Murray Christopher, J. L.; Ndahimananjara Johanita, D.; Perera, F.; Potocnik, J.; Preker Alexander, S.; Ramesh, J.; Rockstrom, J.; Salinas, C.; Samson Leona, D.; Sly Peter, D.; Smith Kirk, R.; Steiner, A.; Stewart Richard, B.; Suk William, A.; van Schayck Onno, C. P.; Yadama Gautam, N.; Yumkella, K.; Zhong, M., The Lancet Commission on pollution and health. *Lancet* **2018,** *391* (10119), 462-512.

6. Armor, J. N., Catalysis and the hydrogen economy. *Catal. Lett.* **2005,** *101* (3-4), 131-135.

7. Kudo, A.; Miseki, Y., Heterogeneous photocatalyst materials for water splitting. *Chem. Soc. Rev.* **2009,** *38* (1), 253-278.

8. Kreuter, W.; Hofmann, H., Electrolysis: the important energy transformer in a world of sustainable energy. *Int. J. Hydrogen Energy* **1998,** *23* (8), 661-666.

9. Gong, M.; Wang, D.-Y.; Chen, C.-C.; Hwang, B.-J.; Dai, H., A mini review on nickel-based electrocatalysts for alkaline hydrogen evolution reaction. *Nano Res.* **2016,** *9* (1), 28-46.

10. McGarrah, J. E.; Kim, Y.-J.; Hissler, M.; Eisenberg, R., Toward a Molecular Photochemical Device: A Triad for Photoinduced Charge Separation Based on a Platinum Diimine Bis(acetylide) Chromophore. *Inorg. Chem.* **2001,** *40* (18), 4510-4511.

11. Santos, D. M. F.; Sequeira, C. A. C.; Maccio, D.; Saccone, A.; Figueiredo, J. L., Platinum-rare earth electrodes for hydrogen evolution in alkaline water electrolysis. *Int. J. Hydrogen Energy* **2013,** *38* (8), 3137-3145.

12. Wu, J.; Yang, H., Platinum-Based Oxygen Reduction Electrocatalysts. *Acc. Chem. Res.* **2013,** *46* (8), 1848-1857.

13. Dasgupta, N. P.; Liu, C.; Andrews, S.; Prinz, F. B.; Yang, P., Atomic Layer Deposition of Platinum Catalysts on Nanowire Surfaces for Photoelectrochemical Water Reduction. *J. Am. Chem. Soc.* **2013,** *135* (35), 12932-12935.

14. Koetz, E. R.; Stucki, S., Ruthenium dioxide as a hydrogen-evolving cathode. *J. Appl. Electrochem.* **1987,** *17* (6), 1190-7.

15. Lee, Y.; Suntivich, J.; May, K. J.; Perry, E. E.; Shao-Horn, Y., Synthesis and Activities of Rutile IrO2 and RuO2 Nanoparticles for Oxygen Evolution in Acid and Alkaline Solutions. *J. Phys. Chem. Lett.* **2012,** *3* (3), 399-404.

16. Reier, T.; Oezaslan, M.; Strasser, P., Electrocatalytic Oxygen Evolution Reaction (OER) on Ru, Ir, and Pt Catalysts: A Comparative Study of Nanoparticles and Bulk Materials. *ACS Catal.* **2012,** *2* (8), 1765-1772.

17. Gersten, S. W.; Samuels, G. J.; Meyer, T. J., Catalytic oxidation of water by an oxo-bridged ruthenium dimer. *J. Am. Chem. Soc.* **1982,** *104* (14), 4029-30.

18. Thomsen, J. M.; Huang, D. L.; Crabtree, R. H.; Brudvig, G. W., Iridium-based complexes for water oxidation. *Dalton Trans.* **2015,** *44* (28), 12452-12472.

19. Goldsmith, J. I.; Hudson, W. R.; Lowry, M. S.; Anderson, T. H.; Bernhard, S., Discovery and High-Throughput Screening of Heteroleptic Iridium Complexes for Photoinduced Hydrogen Production. *J. Am. Chem. Soc.* **2005,** *127* (20), 7502-7510.

20. McDaniel, N. D.; Coughlin, F. J.; Tinker, L. L.; Bernhard, S., Cyclometalated iridium(III) aquo complexes: efficient and tunable catalysts for the homogeneous oxidation of water. *Prepr. Symp. - Am. Chem. Soc., Div. Fuel Chem.* **2008,** *53* (1), 4-5.

21. Gottesfeld, S.; Srinivasan, S., Electrochemical and optical studies of thick oxide layers on iridium and their electrocatalytic activities for the oxygen evolution reaction. *J. Electroanal. Chem. Interfacial Electrochem.* **1978,** *86* (1), 89-104.

22. Sun, Y.; Bigi, J. P.; Piro, N. A.; Tang, M. L.; Long, J. R.; Chang, C. J., Molecular Cobalt Pentapyridine Catalysts for Generating Hydrogen from Water. *J. Am. Chem. Soc.* **2011,** *133* (24), 9212-9215.

23. Zhou, W.; Zhou, J.; Zhou, Y.; Lu, J.; Zhou, K.; Yang, L.; Tang, Z.; Li, L.; Chen, S., N-Doped Carbon-Wrapped Cobalt Nanoparticles on N-Doped Graphene Nanosheets for High-Efficiency Hydrogen Production. *Chem. Mater.* **2015,** *27* (6), 2026-2032.

24. Losse, S.; Vos, J. G.; Rau, S., Catalytic hydrogen production at cobalt centers. *Coord. Chem. Rev.* **2010,** *254* (21-22), 2492-2504.

25. Connolly, P.; Espenson, J. H., Cobalt-catalyzed evolution of molecular hydrogen. *Inorg. Chem.* **1986,** *25* (16), 2684-8.

26. McCrory, C. C. L.; Uyeda, C.; Peters, J. C., Electrocatalytic Hydrogen Evolution in Acidic Water with Molecular Cobalt Tetraazamacrocycles. *J. Am. Chem. Soc.* **2012,** *134* (6), 3164-3170.

27. Kellett, R. M.; Spiro, T. G., Cobalt(I) porphyrin catalysts of hydrogen production from water. *Inorg. Chem.* **1985,** *24* (15), 2373-7.

28. Gong, M.; Dai, H., A mini review on NiFe-based materials as highly active oxygen evolution reaction electrocatalysts. *arXiv.org, e-Print Arch., Condens. Matter* **2014**, 1-31, arXiv:1411 4677v1 [cond-mat mtrl-sci].

29. Felton, G. A. N.; Glass, R. S.; Lichtenberger, D. L.; Evans, D. H., Iron-Only Hydrogenase Mimics. Thermodynamic Aspects of the Use of Electrochemistry to Evaluate Catalytic Efficiency for Hydrogen Generation. *Inorg. Chem.* **2006,** *45* (23), 9181-9184.

30. Wu, G.; More, K. L.; Johnston, C. M.; Zelenay, P., High-performance electrocatalysts for oxygen reduction derived from polyaniline, iron, and cobalt. *Science (Washington, DC, U. S.)* **2011,** *332* (6028), 443-447.

31. Kaur-Ghumaan, S.; Schwartz, L.; Lomoth, R.; Stein, M.; Ott, S., Catalytic Hydrogen Evolution from Mononuclear Iron(II) Carbonyl Complexes as Minimal Functional Models of the [FeFe] Hydrogenase Active Site. *Angew. Chem., Int. Ed.* **2010,** *49* (43), 8033-8036, S8033/1-S8033/12.

32. Bianchini, C.; Fornasiero, P., A Synthetic Nickel Electrocatalyst with a Turnover Frequency above 100 000 s-1 for H2 Production. *ChemCatChem* **2012,** *4* (1), 45-46.

33. Arana, C.; Keshavarz, M.; Potts, K. T.; Abruna, H. D., Electrocatalytic reduction of CO2 and O2 with electropolymerized films of vinyl-terpyridine complexes of Fe, Ni and Co. *Inorg. Chim. Acta* **1994,** *225* (1-2), 285-95.

34. Greeley, J.; Jaramillo, T. F.; Bonde, J.; Chorkendorff, I.; Norskov, J. K., Computational high-throughput screening of electrocatalytic materials for hydrogen evolution. *Nat. Mater.* **2006,** *5* (11), 909-913.

35. Fujishima, A.; Honda, K., Electrochemical photolysis of water at a semiconductor electrode. *Nature (London)* **1972,** *238* (5358), 37-8.

36. Purchase, R. L.; de Groot, H. J. M., Biosolar cells: global artificial photosynthesis needs responsive matrices with quantum coherent kinetic control for high yield. *Interface Focus* **2015,** *5* (3), 20150014.

37. Barigelletti, F.; Juris, A.; Balzani, V.; Belser, P.; Von Zelewsky, A., Temperature dependence of the luminescence emission of ruthenium(II) complexes containing the ligands 2,2'-bipyridine and dipyrido[3,2-c:2',3'-e]pyridazine. *J. Phys. Chem.* **1986,** *90* (21), 5190-3.

38. Hou, C.-C.; Li, T.-T.; Cao, S.; Chen, Y.; Fu, W.-F., Incorporation of a [Ru(dcbpy)(bpy)2]2+ photosensitizer and a Pt(dcbpy)Cl2 catalyst into metal-organic frameworks for photocatalytic hydrogen evolution from aqueous solution. *J. Mater. Chem. A* **2015,** *3* (19), 10386-10394.

39. Belser, P.; von Zelewsky, A.; Frank, M.; Seel, C.; Vogtle, F.; De Cola, L.; Barigelletti, F.; Balzani, V., Supramolecular ruthenium and/or osmium complexes of tris(bipyridine) bridging ligands. Syntheses, absorption spectra, luminescence properties, electrochemical behavior, intercomponent energy, and electron transfer. *J. Am. Chem. Soc.* **1993,** *115* (10), 4076-86.

40. Chen, C.-Y.; Wang, M.; Li, J.-Y.; Pootrakulchote, N.; Alibabaei, L.; Ngoc-Le, C.-H.; Decoppet, J.-D.; Tsai, J.-H.; Gratzel, C.; Wu, C.-G.; Zakeeruddin, S. M.; Gratzel, M., Highly Efficient Light-Harvesting Ruthenium Sensitizer for Thin-Film Dye-Sensitized Solar Cells. *ACS Nano* **2009,** *3* (10), 3103-3109.

41. LI, X.; Wen, J.; Low, J.; Fang, Y.; Yu, J., Design and Fabrication of semiconductor photocatalyst for the photocatalytic reduction of CO2 to solar fuel. *Science China Materials* **2014,** *57* (1), 70-100.

42. Knobloch, F. W.; Rauscher, W. H., Cöordination polymers of copper(II) prepared at liquid-liquid interfaces. *J. Polym. Sci.* **1959,** *38*, 261-2.

43. Berlin, A. A.; Matveeva, N. G., Polymeric chelate compounds. *Usp. Khim.* **1959,** *29*, 277-97.

44. Kubo, M.; Kishita, M.; Kuroda, Y., Polymer molecules involving co-ordination links in the crystals of cupric oxalate and related compounds. *Mezhdunarod. Simpozium po Makromol. Khim., Doklady, Moscow* **1960,** (Sektsiya 1), 185-90.

45. Hoskins, B. F.; Robson, R., Infinite polymeric frameworks consisting of three dimensionally linked rod-like segments. *J. Am. Chem. Soc.* **1989,** *111* (15), 5962-4.

46. Kepert, D. L., Design and construction of a new class of scaffolding-like materials comprising infinite polymeric frameworks of 3D-linked molecular rods. A reappraisal of the zinc cyanide and cadmium cyanide structures and the synthesis and structure of the diamond-related frameworks [N(CH3)4][CuIZnII(CN)4] and CuI[4,4',4",4"'-tetracyanotetraphenylmethane]BF4.xC6H5NO2. *Chemtracts Anal., Phys., Inorg. Chem.* **1990,** *2* (4), 328-32.

47. Yuan, S.; Feng, L.; Wang, K.; Pang, J.; Bosch, M.; Lollar, C.; Sun, Y.; Qin, J.; Yang, X.; Zhang, P.; Wang, Q.; Zou, L.; Zhang, Y.; Zhang, L.; Fang, Y.; Li, J.; Zhou, H.-C., Stable Metal-Organic Frameworks: Design, Synthesis, and Applications. *Adv. Mater. (Weinheim, Ger.)* **2018**, Ahead of Print.

48. Kreno, L. E.; Leong, K.; Farha, O. K.; Allendorf, M.; Van Duyne, R. P.; Hupp, J. T., Metal-Organic Framework Materials as Chemical Sensors. *Chem. Rev. (Washington, DC, U. S.)* **2012,** *112* (2), 1105-1125.

49. Xie, Z.; Ma, L.; de Krafft, K. E.; Jin, A.; Lin, W., Porous Phosphorescent Coordination Polymers for Oxygen Sensing. *J. Am. Chem. Soc.* **2010,** *132* (3), 922-923.

50. Morris, R. E.; Wheatley, P. S., Gas storage in nanoporous materials. *Angew. Chem., Int. Ed.* **2008,** *47* (27), 4966-4981.

51. Farha, O. K.; Oezguer Yazaydin, A.; Eryazici, I.; Malliakas, C. D.; Hauser, B. G.; Kanatzidis, M. G.; Nguyen, S.-B. T.; Snurr, R. Q.; Hupp, J. T., De novo synthesis of a metal-organic framework material featuring ultrahigh surface area and gas storage capacities. *Nat. Chem.* **2010,** *2* (11), 944-948.

52. Sumida, K.; Rogow, D. L.; Mason, J. A.; McDonald, T. M.; Bloch, E. D.; Herm, Z. R.; Bae, T.-H.; Long, J. R., Carbon Dioxide Capture in Metal-Organic Frameworks. *Chem. Rev. (Washington, DC, U. S.)* **2012,** *112* (2), 724-781.

53. Xu, H.-Q.; Hu, J.; Wang, D.; Li, Z.; Zhang, Q.; Luo, Y.; Yu, S.-H.; Jiang, H.-L., Visible-Light Photoreduction of CO2 in a Metal-Organic Framework: Boosting Electron-Hole Separation via Electron Trap States. *J. Am. Chem. Soc.* **2015,** *137* (42), 13440-13443.

54. Li, S.-L.; Xu, Q., Metal-organic frameworks as platforms for clean energy. *Energy Environ. Sci.* **2013,** *6* (6), 1656-1683.

55. Wang, C.; Xie, Z.; de Krafft, K. E.; Lin, W., Doping Metal-Organic Frameworks for Water Oxidation, Carbon Dioxide Reduction, and Organic Photocatalysis. *J. Am. Chem. Soc.* **2011,** *133* (34), 13445-13454.

56. Ma, L.; Falkowski, J. M.; Abney, C.; Lin, W., A series of isoreticular chiral metal-organic frameworks as a tunable platform for asymmetric catalysis. *Nat. Chem.* **2010,** *2* (10), 838-846.

57. Sawano, T.; Thacker, N. C.; Lin, Z.; McIsaac, A. R.; Lin, W., Robust, Chiral, and Porous BINAP-Based Metal-Organic Frameworks for Highly Enantioselective Cyclization Reactions. *J. Am. Chem. Soc.* **2015,** *137* (38), 12241-12248.

58. Manna, K.; Ji, P.; Lin, Z.; Greene, F. X.; Urban, A.; Thacker, N. C.; Lin, W., Chemoselective single-site Earth-abundant metal catalysts at metal-organic framework nodes. *Nat. Commun.* **2016,** *7*, 12610.

59. Furukawa, H.; Cordova, K. E.; O'Keeffe, M.; Yaghi, O. M., The Chemistry and Applications of Metal-Organic Frameworks. *Science (Washington, DC, U. S.)* **2013,** *341* (6149), 974.

60. Li, J.-R.; Kuppler, R. J.; Zhou, H.-C., Selective gas adsorption and separation in metal-organic frameworks. *Chem. Soc. Rev.* **2009,** *38* (5), 1477-1504.

61. Li, J.-R.; Sculley, J.; Zhou, H.-C., Metal-Organic Frameworks for Separations. *Chem. Rev. (Washington, DC, U. S.)* **2012,** *112* (2), 869-932.

62. Horcajada, P.; Chalati, T.; Serre, C.; Gillet, B.; Sebrie, C.; Baati, T.; Eubank, J. F.; Heurtaux, D.; Clayette, P.; Kreuz, C.; Chang, J.-S.; Hwang, Y. K.; Marsaud, V.; Bories, P.-N.; Cynober, L.; Gil, S.; Ferey, G.; Couvreur, P.; Gref, R., Porous metal-organic-framework nanoscale carriers as a potential platform for drug delivery and imaging. *Nat. Mater.* **2010,** *9* (2), 172-178.

63. Lin, W., Nanoscale metal-organic frameworks for biomedical imaging and drug delivery. *Abstracts of Papers, 248th ACS National Meeting & Exposition, San Francisco, CA, United States, August 10-14, 2014* **2014**, PHYS-101.

64. Huxford Rachel, C.; Della Rocca, J.; Lin, W., Metal-organic frameworks as potential drug carriers. *Curr Opin Chem Biol* **2010,** *14* (2), 262-8.

65. Hafizovic Cavka, J.; Jakobsen, S.; Olsbye, U.; Guillou, N.; Lamberti, C.; Bordiga, S.; Lillerud, K. P., A
New Zirconium Inorganic Building Brick Forming Metal Organic Frameworks with Exceptional Stability. *J. Am. Chem. Soc.* **2008,** *130* (42), 13850-13851.

66. Zhang, T.; Lin, W., Metal-organic frameworks for artificial photosynthesis and photocatalysis. *Chem. Soc. Rev.* **2014,** *43* (16), 5982-5993.

67. Lin, J.; Hu, X.; Zhang, P.; Van Rynbach, A.; Beratan, D. N.; Kent, C. A.; Mehl, B. P.; Papanikolas, J. M.; Meyer, T. J.; Lin, W.; Skourtis, S. S.; Constantinou, M., Triplet Excitation Energy Dynamics in Metal-Organic Frameworks. *J. Phys. Chem. C* **2013,** *117* (43), 22250-22259.

68. Zhang, Q.; Zhang, C.; Cao, L.; Wang, Z.; An, B.; Lin, Z.; Huang, R.; Zhang, Z.; Wang, C.; Lin, W., Förster Energy Transport in Metal-Organic Frameworks Is Beyond Step-by-Step Hopping. *J. Am. Chem. Soc.* **2016,** *138* (16), 5308-5315.

69. Lee, C. Y.; Farha, O. K.; Hong, B. J.; Sarjeant, A. A.; Nguyen, S. B. T.; Hupp, J. T., Light-Harvesting Metal-Organic Frameworks (MOFs): Efficient Strut-to-Strut Energy Transfer in Bodipy and Porphyrin-Based MOFs. *J. Am. Chem. Soc.* **2011,** *133* (40), 15858-15861.

70. Horiuchi, Y.; Toyao, T.; Saito, M.; Mochizuki, K.; Iwata, M.; Higashimura, H.; Anpo, M.; Matsuoka, M., Visible-Light-Promoted Photocatalytic Hydrogen Production by Using an Amino-Functionalized Ti(IV) Metal-Organic Framework. *J. Phys. Chem. C* **2012,** *116* (39), 20848-20853.

71. Kataoka, Y.; Sato, K.; Miyazaki, Y.; Masuda, K.; Tanaka, H.; Naito, S.; Mori, W., Photocatalytic hydrogen production from water using porous material [Ru2(p-BDC)2]n. *Energy Environ. Sci.* **2009,** *2* (4), 397-400.

72. Pullen, S.; Fei, H.; Orthaber, A.; Cohen, S. M.; Ott, S., Enhanced photochemical hydrogen production by a molecular diiron catalyst incorporated into a metal-organic framework. *J. Am. Chem. Soc.* **2013,** *135* (45), 16997-17003.

73. Wang, C.; Wang, J.; Lin, W., Elucidating Water Oxidation Pathways of Iridium Complexes Using Metal-Organic Frameworks: A Comprehensive Structural, Catalytic, Spectroscopic, and Kinetic Study. *Abstracts, 64th Southeast Regional Meeting of the American Chemical Society, Raleigh, NC, United States, November 14-17* **2012**, SERM-125.

74. Lu, X.-F.; Liao, P.-Q.; Wang, J.-W.; Wu, J.-X.; Chen, X.-W.; He, C.-T.; Zhang, J.-P.; Li, G.-R.; Chen, X.-M., An Alkaline-Stable, Metal Hydroxide Mimicking Metal-Organic Framework for Efficient Electrocatalytic Oxygen Evolution. *J. Am. Chem. Soc.* **2016,** *138* (27), 8336-8339.

75. Kornienko, N.; Zhao, Y.; Kley, C. S.; Zhu, C.; Kim, D.; Lin, S.; Chang, C. J.; Yaghi, O. M.; Yang, P., Metal-Organic Frameworks for Electrocatalytic Reduction of Carbon Dioxide. *J. Am. Chem. Soc.* **2015,** *137* (44), 14129-14135.

76. Fu, Y.; Sun, D.; Chen, Y.; Huang, R.; Ding, Z.; Fu, X.; Li, Z., An Amine-Functionalized Titanium Metal-Organic Framework Photocatalyst with Visible-Light-Induced Activity for CO2 Reduction. *Angew. Chem., Int. Ed.* **2012,** *51* (14), 3364-3367, S3364/1-S3364/25.

CHAPTER 2

Photocatalytic Hydrogen Evolution with Earth-Abundant Metal-Porphyrin Based Metal-Organic Frameworks

2.1 Introduction

With an average irradiance of 1000 W m^{-2}, solar energy is the most abundant source of clean and renewable energy available.[1] Solar energy can be harvested and converted to electricity by photovoltaic devices, yet the application is limited due to the difficulty of storing electrical energy. Using sunlight to drive energetically uphill chemical reactions and producing storable fuels has thus become an important alternative strategy for solar energy utilization.[2] Photo-driven splitting of water into hydrogen and oxygen is one of the most promising candidates for such photochemical processes. Hydrogen is a clean and efficient energy source upon combustion and is an important reagent in industrial processes such as the Haber-Bosch reaction.[3] Unfortunately, platinum and other precious metals are often used as photochemical hydrogen evolution catalysts, and their high costs and scarcity impede further implementation in large scale industrial applications.[4-6]

Metal-organic frameworks (MOFs) provide an alternative material platform for photocatalytic applications. MOFs are highly crystalline and porous materials constructed from metal ions or clusters bonded to organic linkers forming one-, two-, or three-dimensional structures. Because of their ultra-high surface area and customizable diversity, MOFs have served as functional materials for a bevy of applications including but not limited to gas storage,[7] chemical separation,[8] luminescence,[9] catalysis,[10] and drug delivery.[11]

Photoactive MOF materials can be used to integrate different functional components that are needed for solar energy conversion in one system. The photochemical reduction of protons

requires at least two components, a photosensitizer to harvest sunlight and create an electron-hole pair and a catalyst to use the electron to actively reduce protons in solution to afford hydrogen.[12] MOFs have been previously shown to promote effective electron and energy transfer within their frameworks comprised of light harvesting organic linkers and have been combined with co-catalysts such as platinum nanoparticles and polyoxometalates to carry out proton reduction.[13-15] Herein, we study photocatalytic hydrogen evolution reactions (HERs) with water-stable Earth-abundant metal (EAM)-porphyrin based MOFs built from Zr_6 and Zr_{12} secondary building units (SBUs). These MOFs contain Zn-porphyrin photosensitizers and Co-porphyrin catalysts within the same framework for effective HER.

2.2 Results and Discussion

2.2.1 Material Synthesis and Characterization

Three porphyrin-based MOFs were constructed from $Zr_6(\mu_3\text{-}O_4)(\mu_3\text{-}OH)_4(RCO_2)_{12}$ (Zr_6) and $Zr_{12}(\mu_3\text{-}O)_8(\mu_3\text{-}OH)_8(\mu_2\text{-}OH)_6(RCO_2)_{18}]$ (Zr_{12}) SBUs in good yields and used for photochemical reduction of protons. Zr_6-DBP and Zr_6-DPDBP were prepared through solvothermal reactions of either 5, 15-di(*p*-benzoato)porphyrin (H_2DBP)[16] or 5,15-di(*p*-benzoato)-10,20-diphenyl-porphyrin (H_2DPDBP)[17] with $ZrCl_4$ in a dimethylformamide (DMF) solution containing a small amount of trifluoroacetic acid. Zr_{12}-DBP was synthesized by heating a mixture of H_2DBP, $ZrCl_4$, water, and acetic acid in DMF at 85 °C. For each MOF, post-synthetic metalation of the porphyrin ligands was achieved through the one-pot reaction of the MOFs with $ZnCl_2$ and $CoCl_2 \cdot 6H_2O$ in DMF at 100 °C overnight. By varying the ratios of the zinc and cobalt salts, precise doping ratios of the metals were achieved.

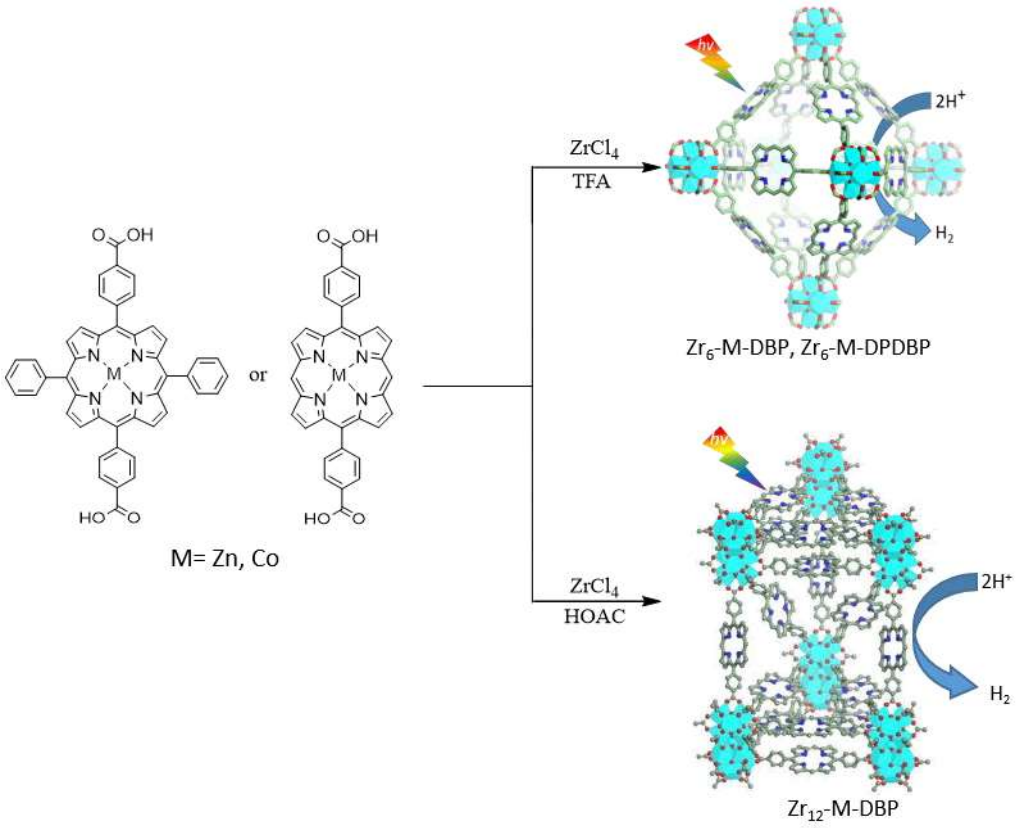

Scheme 2-1. The active materials Zr_6-M-DBP, Zr_6-M-DPDBP, and Zr_{12}-M-DBP and their reaction conditions.

Zr_6-DBP and Zr_6-DPDBP as well as their metalated derivatives crystalize in the cubic space group $Fm\bar{3}m$ and retain crystallinity as judged by the similarity of their PXRD patterns in Figure 2.1. The Zr_6 MOFs have triangular channels of 1.6 nm and octahedral and tetrahedral cavities of 2.8 and 2.0 nm in dimensions, respectively. The shortest distance between metal centers within porphyrin sites was measured to be 13.7 Å, which should allow for effective electron transfer between adjacent M-porphyrin species. Zr_{12}-DBP and its metalated derivative crystallize in the hexagonal space group $P6_3/mmc$ with a shortest distance between metal centers of 6.77 Å measured along the equatorial plane of the Zr_{12} cluster. The ligand to ligand distance within the

triangular pores is slightly longer at 14.2 Å which is still short enough for efficient electron transfer.[18]

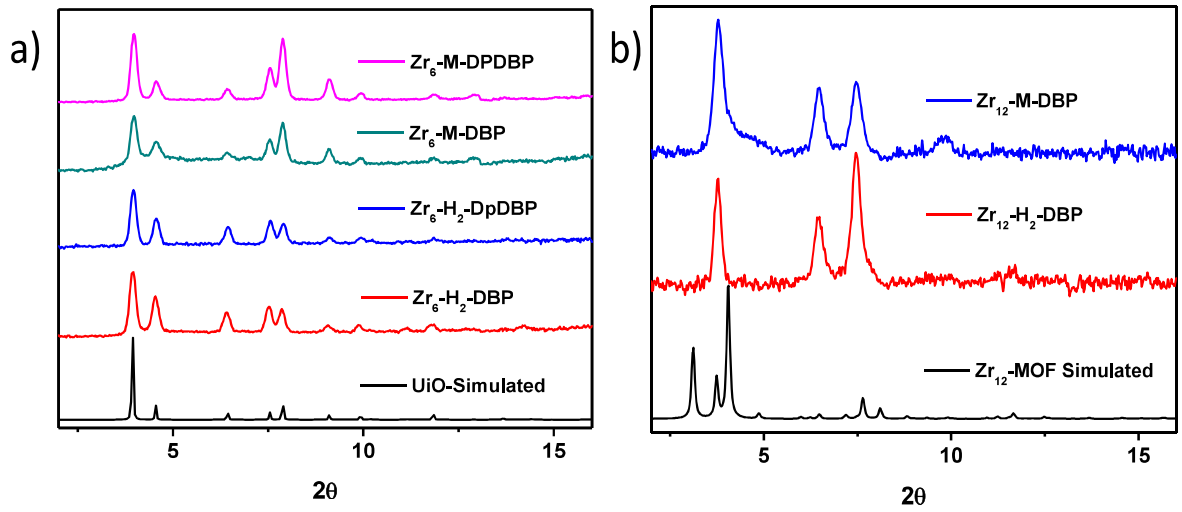

Figure 2-1. a) PXRD patterns of Zr_6 MOFs with free-base and metalated porphyrins along with the simulated pattern based on the UiO structure. b) PXRD patterns of Zr_{12} MOFs with free-base and metalated porphyrins along with the simulated pattern based on the Zr_{12} structure.

The coordination environment of the catalytically active Co-porphyrin species in Zr_6-M-DBP was determined through X-ray Absorption Fine Structure (XAFS) spectroscopy (Figure 2-2). XAFS data was processed and analyzed using the Athena and Artemis programs of the IFEFFIT package based on FERR 6.[19] The X-ray absorption near edge structure (XANES) region indicated a mixed valent cobalt(III)/cobalt(II) oxidation state with a peak centered at 7.712 keV as compared to 7.711keV for a Co(II) oxidation state as well as a slight shoulder observed at 7716 keV (Figure 2-2). The XAFS region reveals a five coordinate cobalt species with degenerate basal Co-N bonds from the porphyrin ring and one apical Co-Cl bond of 2.06 Å. The five coordinate geometry and Co(III) oxidation state led to the Soret band absorbance at 418 nm, which is in contrast to the Soret band at 408 nm for typical four-coordinate Co(II)-porphyrin species (Figure 2-3).[20]

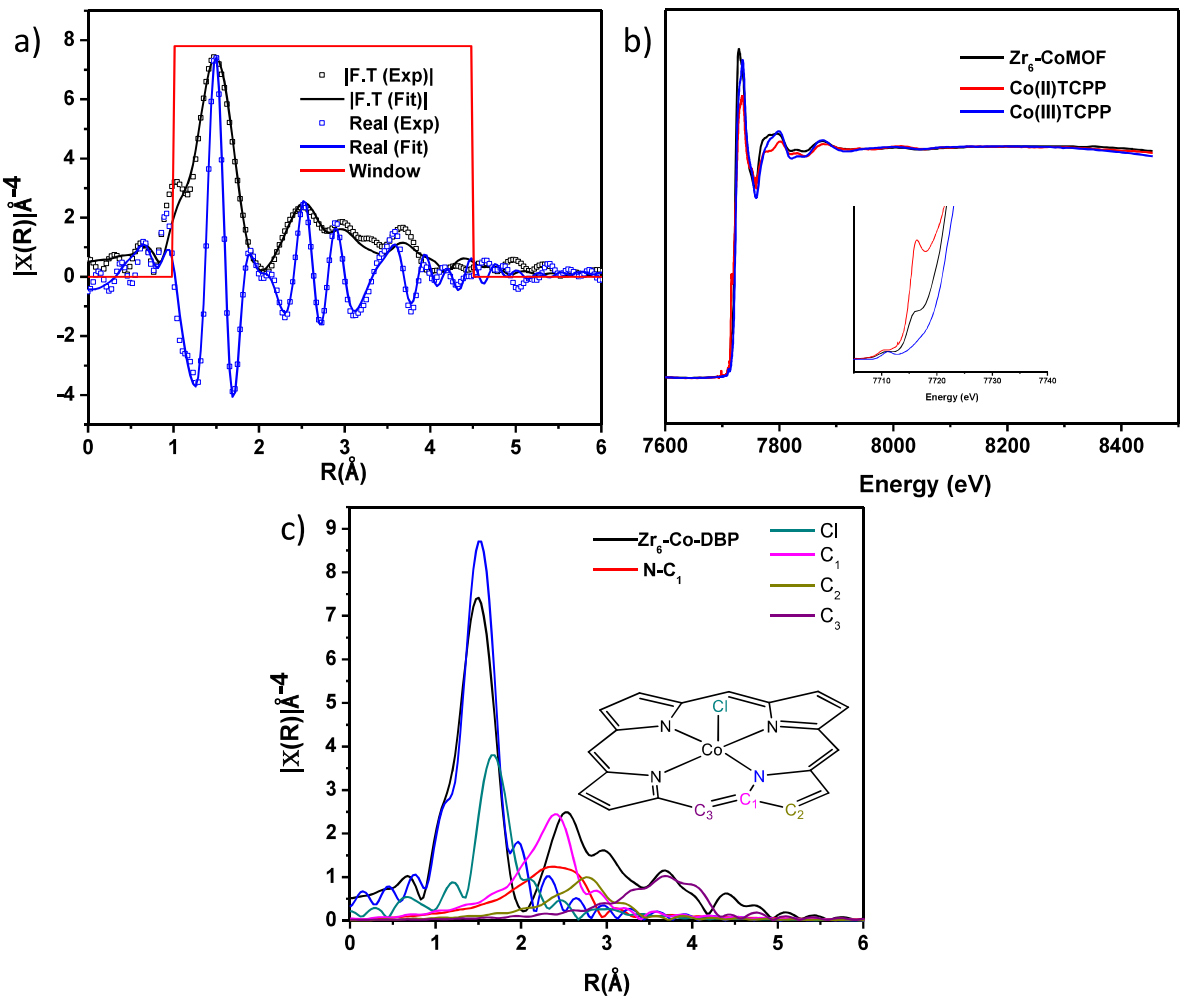

Figure 2-2. a) The fitting of Zr_6-Co-DBP EXAFS at the Cobalt K-edge to the PCN-222 model.[2] b) The XANES region of Zr_6-Co-DBP compared to other Co-porphyrin species at the cobalt k-edge. c) The EXAFS fits of Zr_6-Co-DBP and its composite scattering intensities.

Table 2-1. The parameters used for fitting the EXAFS of Zr_6-M-DBP to a the PCN-222 model.[2]

Parameter	Value	Error
Amp	1.0773	0.0838
E_0	-1.7685	1.5084
delR_N	-0.0257	0.0085
ss_N	0.0043	0.0016
delR_Cl	-0.0098	0.0146
ss_Cl	0.0016	fixed
delR_C_1	-0.0195	0.0129
ss_C_1	0.0087	0.0014
delR_C_2	-0.0487	0.0228
ss_C_2	0.0068	0.0027
delR_C_3	0.1226	0.0218
ss_C_3	0.0051	0.0018
delR_C_4	-0.013	0.0382
ss_C_4	0.0028	0.0039
Reduced X^2	91.76	n/a
R-Factor	0.0158	n/a

The MOFs were rationally designed for the photochemical reduction of protons in the aqueous environment. MOFs comprised of a zirconium-carboxylate SBUs are among the most stable MOF classes reported, particularly in aqueous media, owing to the strong Lewis-acidity of the Zr(IV) ions.[21] Zn- and Co-porphyrins were chosen as the organic linkers for all three MOFs because of their intense absorption in the visible spectrum from their Soret bands (Figure 2-3). Furthermore, Zn-porphyrin has a comparatively long-lived singlet excited state compared to the Co-porphyrin species.[22] The relatively long lived excited state allows the Zn-porphyrin struts to be preferentially reduced by a sacrificial electron donor from its excited state, thereby preventing electron hole-recombination and facilitating electron transfer throughout the MOF to the catalytically active cobalt species.

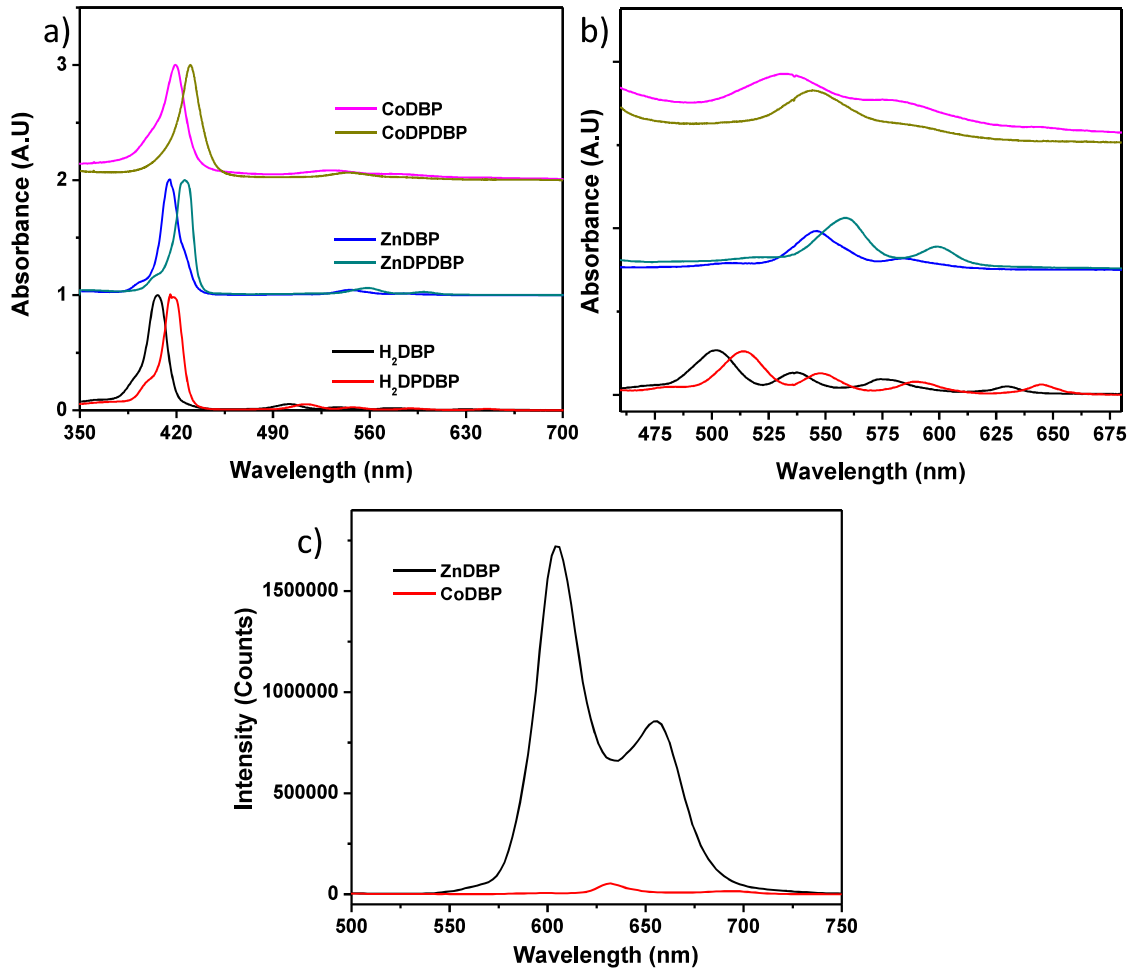

Figure 2-3. a) The normalized UV-VIS spectra of free-base and metalated DBP and DPDBP ligands in DMF. b) Zoomed-in views of the UV-VIS spectra for free-base and metalated DBP and DPDBP ligands. c) Steady-state photoluminescence spectra of 3μM ZnDBP and CoDBP ligands in DMF excited at 420 nm.

2.2.2 Photochemical Properties

Previous studies have shown that Co-porphyrins can be effective proton reduction catalysts when coupled with a photosensitizer such as tris(bipyridine)ruthenium(II) ($[Ru(bpy)_3]^{2+}$).[23] We proposed that the incorporation of Zn-porphyrin as the photosensitizer and Co-porphyrin as the

HER catalyst in the same framework would lead to enhanced electron transfer between the two to facilitate proton reduction.

To achieve active proton reduction in the assembly, the photo-activated photosensitizers must be able to inject electrons into the catalysts. Stern-Völmer quenching experiments showed that the luminescence of homogenous Zn-porphyrin was quenched upon the addition of CoDBP; the emission intensity of 30 μM ZnDBP decreased to 68% of the initial intensity when 15 μM CoDBP was added. More than 5% equivalents of CoDBP relative to the amount of ZnDBP must be present to quench the luminescence of ZnDBP, likely due to inefficient diffusional encounter at these low concentrations (Figure 2-4). MOFs should be able to alleviate this issue due to the high local concentrations of the Co photocatalyst and Zn photosensitizer that are separated by short distances.

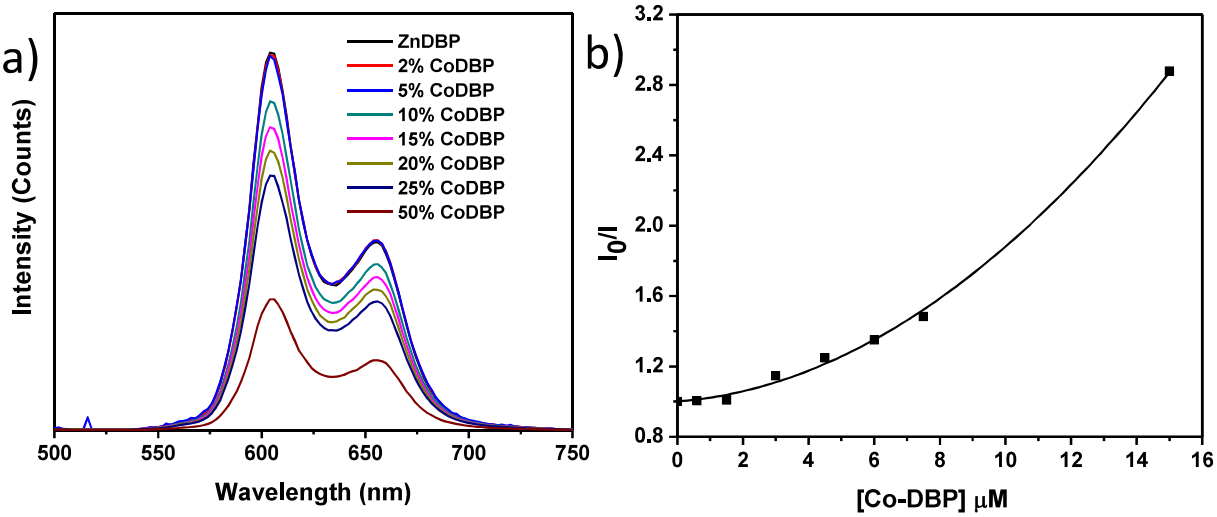

Figure 2-4. a) The luminescence intensity of 30μM ZnDBP with increasing percentages of CoDBP present in DMF. All percentages are relative to the ZnDBP concentration. b) The Stern-Völmer plot of ZnDBP with addition of Co-DBP in different concentrations.

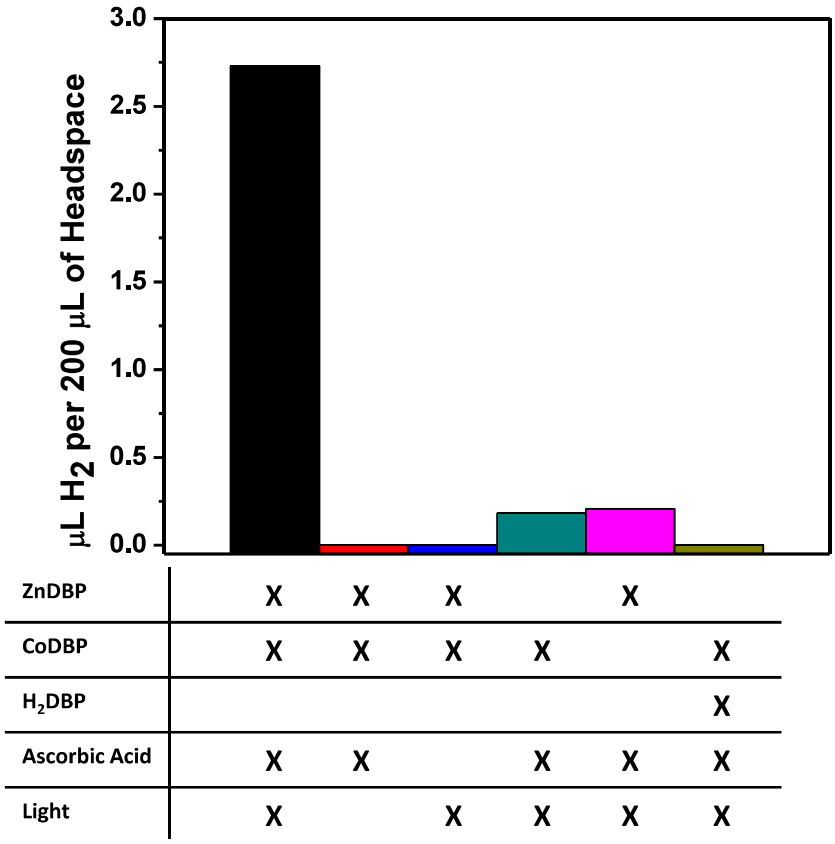

Figure 2-5. Photocatlytic hydrogen production by Zr_6-M-DBP in pH 4 ascorbic acid along with a series of MOF controls in which the metal centers, sacrificial agent, and light source were varied.

The MOFs were examined for their photocatalytic activities towards HER using a 530 mW visible light source at >400 nm. The reaction was carried out at pH = 4 with 0.037M ascorbic acid as a sacrificial electron donor. Hydrogen production was quantified by gas chromatography (GC) of headspace gases after irradiation. Under optimized conditions, the Zn:Co ratio in the MOF was 19:1 with all porphyrin coordination sites occupied as determined by inductively coupled plasma mass spectrometry (ICP-MS). The highest hydrogen evolution turnover number (TON) for each MOF based on Co-Porphyrin (Co-TON) was found to be 75 for Zr_6-M-DPDBP, 52 for Zr_6-M-DBP, and 31 for Zr_{12}-M-DBP after irradiation for five hours. The average TONs for all three MOFs after two hours irradiation can be found in Table 2-2 and Figure 2-6. Compared to their respective

homogenous analogs, the MOF based catalysts showed as high as 15 times enhancement in TON, with Zr_6-M-DPDBP (average TON = 34.8) catalyzing hydrogen slightly more effectively than that of the Zr_6-M-DBP (average TON = 24.0) and Zr_{12}-M-DBP (average TON = 18.7). The higher hydrogen production observed for Zr_6-M-DPDBP compared to Zr_6-M-DBP is likely due to that fact that the additional phenyl groups decrease donor-acceptor distance between struts and enhance the rate of electron transfer. Surprisingly, Zr_{12}-M-DBP which has the shortest linker-linker distance of 6.7 Å was the least active material for proton reduction, likely a result of the high rate of defect sites and ligand vacancies within the MOF as reported previously for Hf_{12}-DBP.[24] These vacancies increase the overall nearest neighbor distances of Zr_{12}-M-DBP and limit electron transfer.

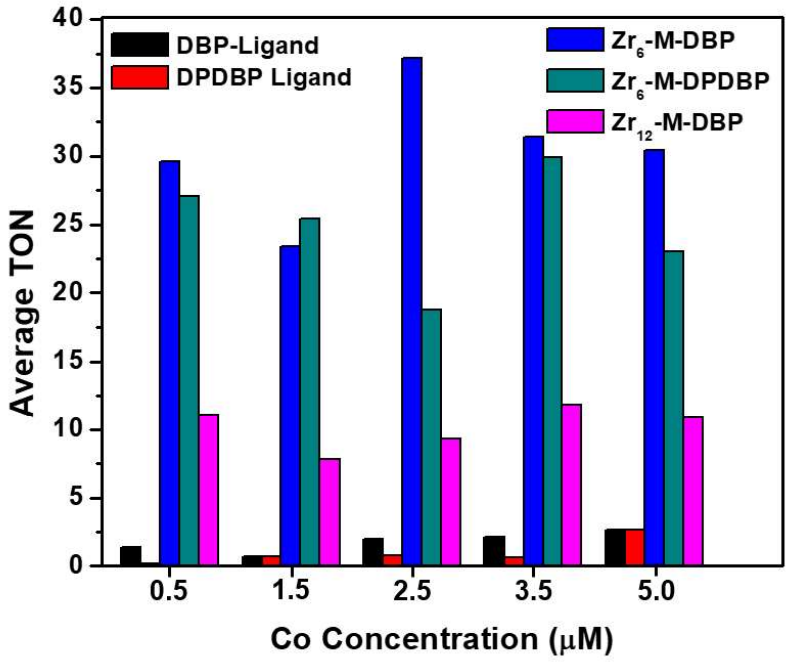

Figure 2-6. Average TONs of Zr_6-M-DBP, Zr_6-M-DPDBP, and Zr_{12}-M-DBP (5 mol% Co loading in the MOF) verses homogeneous M-DBP and M-DPDBP for photocatalytic hydrogen production in pH 4 ascorbic acid.

Table 2-2. Average TONs for Zr_6-M-DBP, Zr_6-M-DPDBP, and Zr_{12}-M-DBP and homogenous M-DBP and M-DPDBP after two hours irradiation in pH 4 ascorbic acid with CoDBP loading ranging from 3.45-7.42% as determined by ICP-MS.

Material	Average TON	Standard Deviation
Zr_6-M-DBP	24.02	14.3
Zr_6-M-DPDBP	34.84	14.78
Zr_{12}-M-DBP	14.67	5.26
DBP-Ligand	2.39	1.74
DPDBP-Ligand	2.28	1.71

The proton reduction reaction is proposed to proceed in accordance with the mechanism in Scheme 2-2. In said mechanism, a Zn-porphyrin strut is excited upon the absorption of light where it is actively reduced by the electron donor ascorbic acid. Two reduced zinc-porphyrin species then sequentially transfer electrons to a cobalt porphyrin center where proton reduction into hydrogen occurs. A series of control experiments confirmed that all four components, zinc porphyrin, cobalt porphyrin, ascorbate, and a light source, are necessary for appreciable hydrogen generation to occur (Figure 2-5).

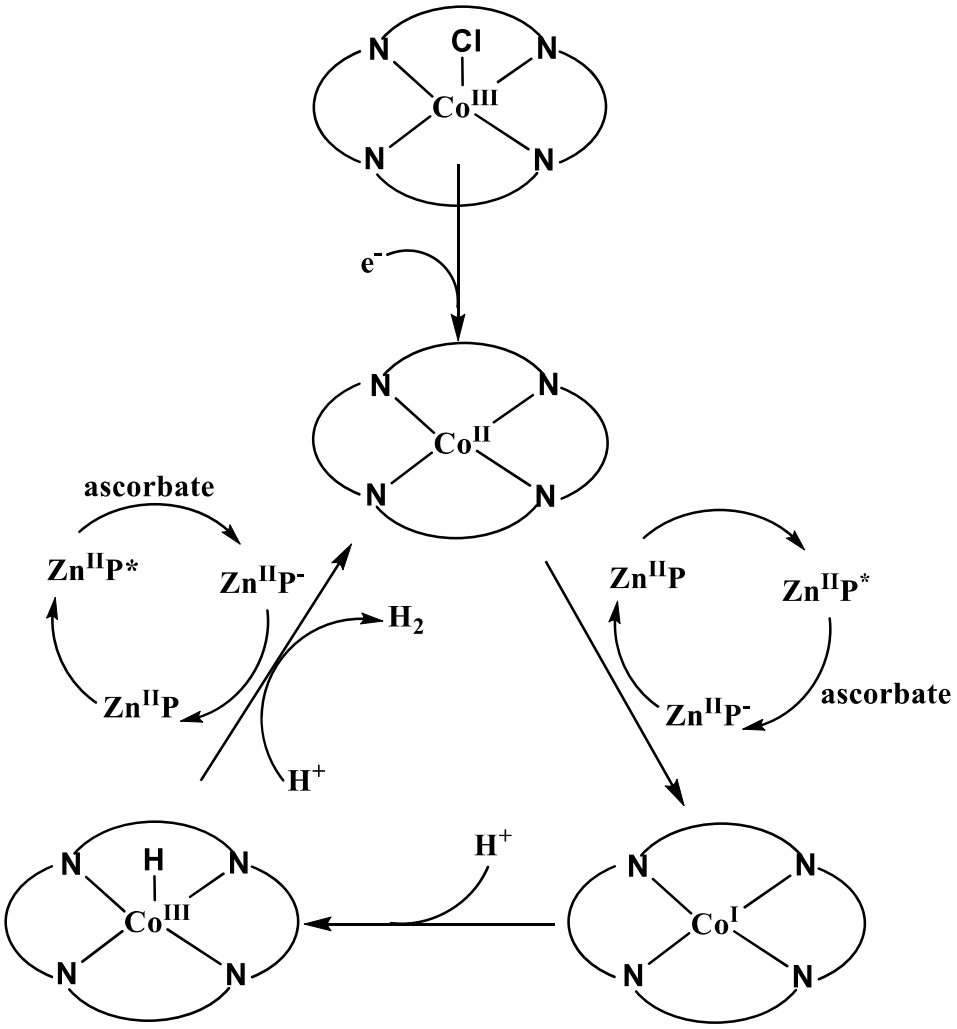

Scheme 2-2. Zr_6-M-DBP, Zr_6-M-DPDBP, and Zr_{12}-M-DBP are active photocatalysts for proton reduction when metalated with Zn and Co to serve as photosensitizer and catalysts, respectively. The mechanism of proton reduction likely proceeds through a Co(III)-H intermediate.

The improved HER perfromance of the MOF materials over that of their homogenous counterpart results from a synergistic and cooperative interaction between the linkers uniformly distributed in the MOF. The close proximity of the linkers to their neighbors results in a significantly increased rate of electron transfer between M-porphyrin centers in MOFs as compared to the homogenous counterparts which rely on diffusion. Photoluminescence lifetime studies of the MOF materials provide supporting evidence for this enhanced interaction between

the photosensitizing and catalytic linkers. The lifetime of Zr_6-Zn-DBP decreases with increasing doping concentrations of cobalt in the MOF (Figure 2-6). This behavior results from efficient energy transfer between the porphyrin struts, likely involving both the Forster and Dexter type mechanisms. Energy transfer within the homogenous material is shown in fluorescent lifetime spectra in Figure 2-7. However, appreciable quenching is only seen as the Co-DBP concentration is greater than 10 mol% of the total M-DBP in solution, further highlighting the diffusion limited interaction between the Co and Zn species while in solution.

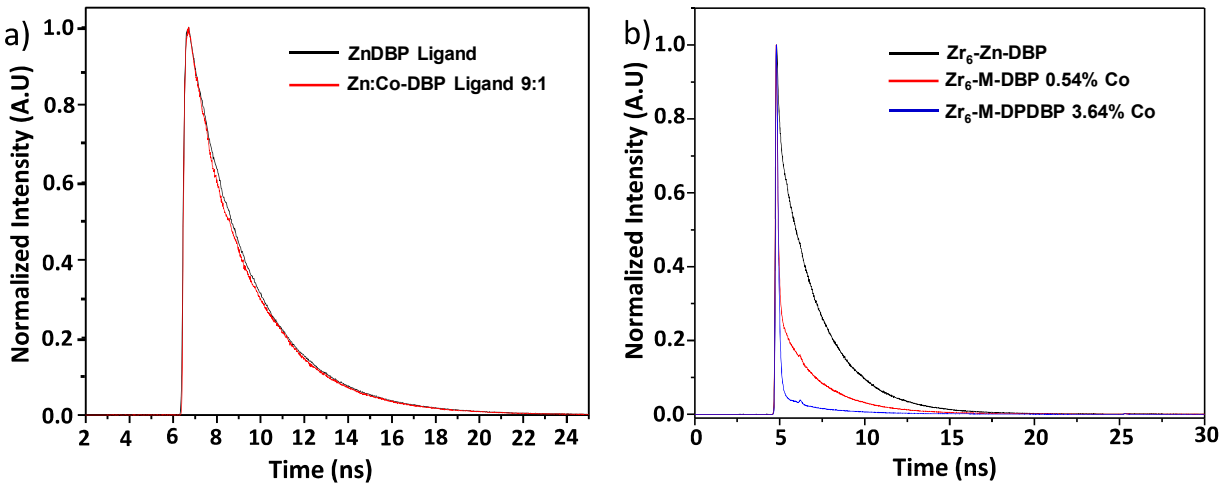

Figure 2-7. a) Luminescence lifetime measurements for Zn-DBP in DMF with the addition of Co-DBP (9:1 ratio). b) Luminescence lifetime measurements of Zr-Zn-DBP with varying doping concentrations of Co in DMF.

Table 2-3. Excited state lifetimes of DBP ligands and MOFs in DMF, fitted by software. Averages from bi-exponential fits were calculated according to the f-weighted technique.

Sample	τ_1 (ns)	τ_2 (ns)	τ_{avg}(ns)
Zn-DBP	2.8	N/A	2.8
Zn:Co-DBP (9:1)	2.8	N/A	2.8
Zr_6-M-DBP (100% Zn)	9.17	2.37	2.53
Zr_6-M-DBP (0.54% Co)	2.27	5.79	2.38
Zr_6-M-DPDBP (3.64% Co)	1.42	3.77	1.81

Electrochemical studies were performed to further analyze the roles of each linker in the HER reaction. The reversible first reduction potential of Zn-DBP occurs at -1.13V vs NHE (Figure 2-8) and is sufficiently negative to reduce Co(II) to Co(I) that has a reduction potential of -0.474V. These results are in agreement with literature reports for analogous systems.[25-27] The small reversible peak seen in both samples at 0.770V vs NHE can be assigned to the reduction of trace amounts of oxygen. Because Zn-DBP can only carry out reduction of the cobalt center to the Co(I) state in the ground state, the mechanism likely goes through a Co(III)-hydride intermediate rather than through a Co(0) species. This mechanism was validated upon the addition of trifluoroacetic acid (TFA) proton source to a solution of Co-DBP in acetonitrile. A non-reversible increase in current is observed immediately following the Co(II)/Co(I) reduction potential of the cobalt species indicative of HER (Figure 2-8). The onset of this peak concurrent with the reduction to a Co(I) state supports the possibility of a Co(III)-H reactive intermediate as found in analogous systems such as cobaloximes.[28] Likely, the bound proton possesses enough electron density to interact with free protons as a Co(III)-H intermediate to facilitate proton reduction upon a secondary reduction of the porphyrin molecule.[29] However, unlike homogenous cobalt HER catalysts, the MOF systems cannot undergo proton reduction through the homolytic pathway as

the rigid spatial arrangements of the porphyrin species prevent any bimolecular interactions within the MOF lattice.

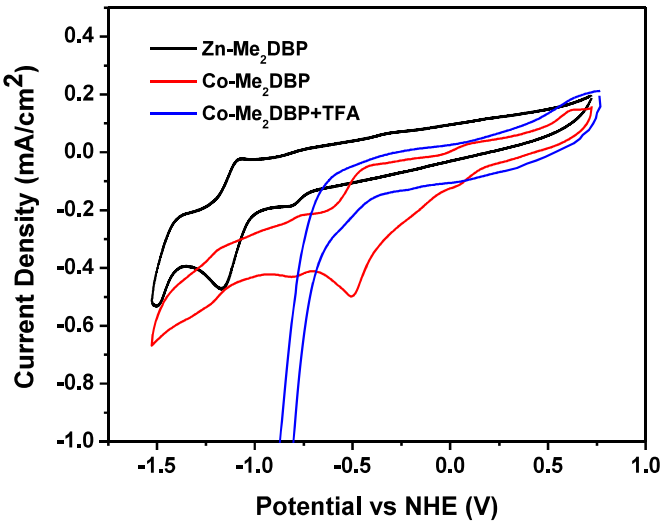

Figure 2-8. CV traces of homogenous Co-Me_2DBP (with and without trifluoroacetic acid) and Zn-Me_2DBP ester in acetonitrile with 0.1 M $TBAPF_6$.

The mechanism for hydrogen evolution was further supported with density functional theory (DFT). DFT calculations were performed using a B3LYP-6331G* basis set for structure optimization of Co-DPDBP and B3LYP-6331G** for charge calculations (Table 2-4). As expected, the charge varied depending on whether Mulliken or NBO methods were used. However, both show the same trend of a significant decrease of charge on the cobalt center upon reduction of the ground state concurrent with ligand non-innocence, followed by a slight increase in cobalt charge after protonation of the cobalt center to a Co(III)-H product. Though the calculated results do not explicitly support the formation of Co(III)-H^- intermediate, instead a Co(I)-H is shown as most of the additional electron density resides within the porphyrin macrocycle, the charge values on the cobalt center matches those reported previously for other "Co(III)-H" intermediates found

in analogous cobaloximes systems.[27] Therefore, we can conclude that the PCET to the intermediate to form hydrogen is not simply metal-centered, but is facilitated by the entire porphyrin assembly within the MOF material due to ligand non-innocence.

Table 2-4. The DFT calculated atomic charges for the central Co atom and its surrounding first coordination shell at four separate states throughout the hydrogen production process for Co-DBPDP. * denotes the use of the B3LYP/6311+G* basis set in contrast to the B971/631+G* basis set.

		NBO*	NBO	Mulliken
Ground state	Co Charge	0.835	0.851	1.06
	Average N Charge	-0.537	-0.786	-0.795
	H Charge	n/a	n/a	n/a
First Reduction	Co Charge	0.253	0.572	0.572
	Average N Charge	-0.498	-0.754	-0.754
	H Charge	n/a	n/a	n/a
Co-H	Co Charge	0.274	0.834	0.834
	Average N Charge	-0.466	-0.767	-0.767
	H Charge	0.177	0.013	0.013

Despite producing hydrogen at a comparably high TON for precious metal free MOF based photocatalysts, the MOF species do degrade after irradiation and become amorphous, thereby decreasing production of hydrogen as a function of time as seen in Figure 2-9. However, this destructive process is mitigated for that of the Zr_{12} species which retains proficient crystallinity after two hours and can maintain a high level of hydrogen production for at least 5 hours. The increased stability of the Zr_{12} species is likely the result of decreased solubility of the reduced Zn-porphyrin linker in solution for the Zr_{12} due to electronic and dielectric effects imparted by the SBU.[30] Improved inter-linker-electron-transfer rates within MOFs can likely mitigate this effect and highlights the need for fixing chromophores and catalysts in close proximity to each other for photocatalytic applications.

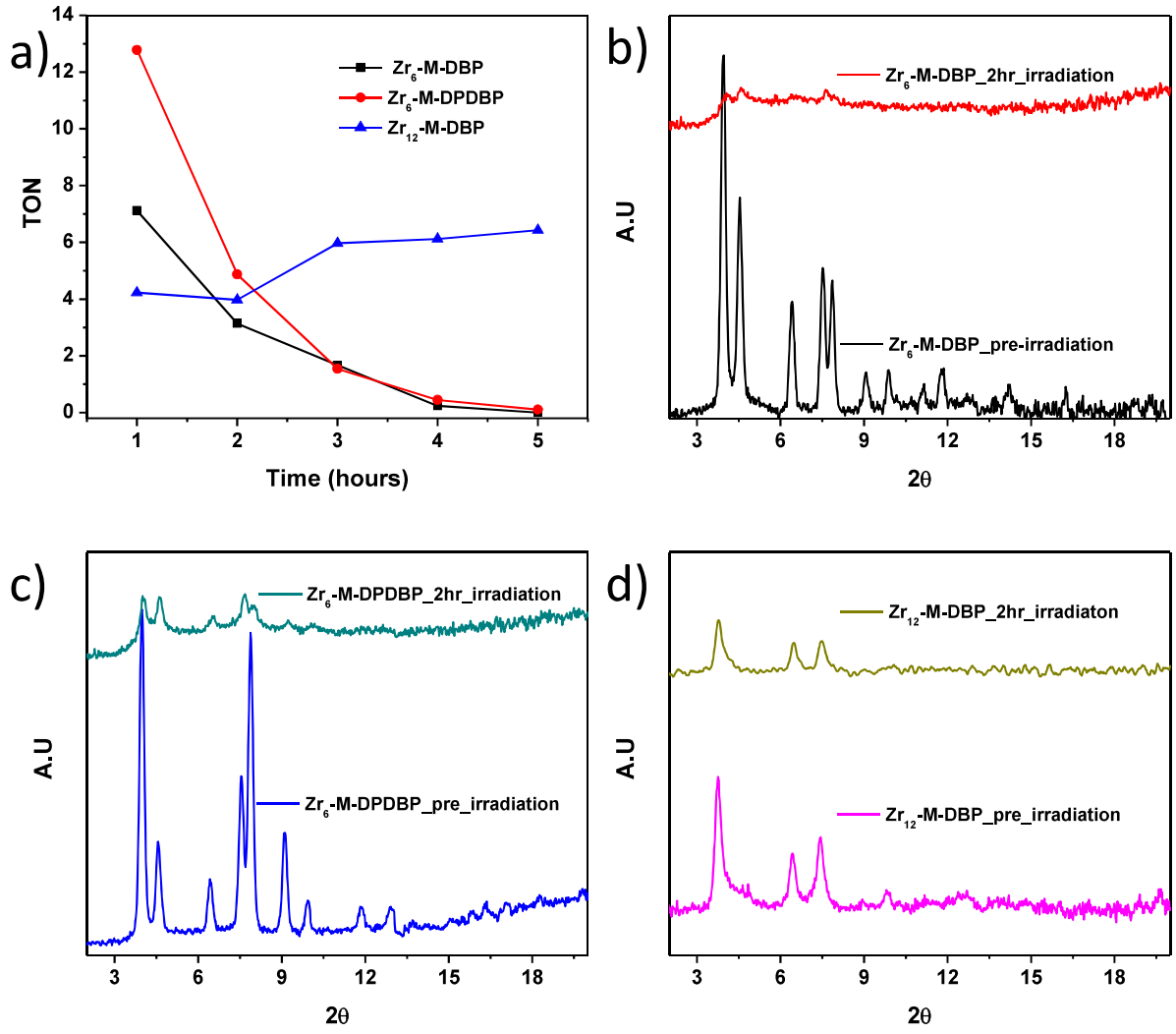

Figure 2-9. a) Time-dependent photopcatalytic HER by Zr_6-M-DBP, Zr_6-M-DPDBP and Zr_{12}-M-DBP in pH 4 ascorbic acid. PXRD of b) Zr_6-M-DBP, c) Zr_6-M-DPDBP and d) Zr_{12}-M-DBP before after two hours of photocatalysis.

2.4 Conclusion

We have successfully incorporated both photosensitizer and catalyst in porphyrin based metal-organic frameworks through a post synthetic metalation procedure with zinc and cobalt ions respectively. Built from either DBP or DPDBP and Zr_6 or Zr_{12} SBUs, all three porphyrin MOF species successfully catalyze hydrogen production from aqueous protons at a rate higher than their homogenous analog, owing to the close proximity and high density of linkers inherent within the MOF lattice. Furthermore, the geometric nature of the MOF materials ensures that proton reduction goes through a heterolytic pathway, providing an unambiguous system to study the hydrogen evolution reaction. The porphyrin MOFs have thus provided a versatile and tunable platform for the integration and optimization of various functional components for the application and study of solar energy conversion.

2.5. Experimental Methodologies

2.5.1 Photochemical Proton Reduction Parameters

A 0.037 M pH 4 ascorbic acid buffer was used as the solution for all reported photochemical hydrogen production data to serve as both the proton source and sacrificial reductant. The solution and head space were degassed for thirty minutes with nitrogen prior to irradiation with a 530 mW Thor Labs visible light source. The sample vials were kept in a water bath to stabilize reaction temperature during the photochemical reaction. To quantify the amount of hydrogen produced, 100 μL of the reaction atmosphere was removed from the headspace and injected into a gas chromotograph with a previously fabricated calibration curve. The amount of gas produced was then back-calculated from the GC data with the ideal gas law.

2.5.2 EXAFs

X-ray absorption data was collected at Beamline 9-BM-C at the Advanced Photon Source at Argonne National Laboratory. Spectra were collected at the cobalt K-edge in transmission mode. A pure cobalt foil standard was used as the reference energy for calibration and was measure simultaneously with the experimental sample. Data was collected over three energetic regimes relative to the cobalt K-edge: the pre-edge region from -150 to -20 eV, the XANES region from -20 to 50 eV, and the EXAFs region from 3.62 to 13.93 Å. The sample was pulverized and prepared with in a polyethyleneglycol matrix and packed into a sample holder to achieve necessary absorption.

2.5.3 Data Processing

The XAFs data was processed using the Athena and Artemis programs of the IFEFFIT package. Prior to merging, spectra were calibrated against the cobalt reference spectra by determining the energy corresponding to the first peak in the first derivative of the absorption spectrum.

Once the data was processed, the fits of the EXAFS region were determined using the Artemis program. For all fits, the number of parameters was limited to fewer than two thirds the total number of independent points as determined by the Nyquist equation. Fits were performed with a k-weight of three in R-space. The CoDBP was MOF was fitted with the reported crystal structure for PCN-222, a cobalt porphyrin MOF, obtained from the Cambridge Crystallographic Database.

2.6 Synthetic Procedures

2.6.1 Synthesis of Ligands

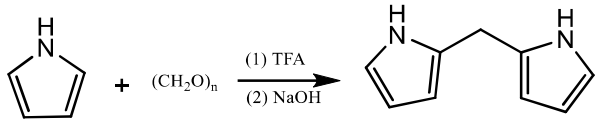

Scheme 2-3. Synthesis of 2,2' Dipyrromethane.

Paraformaldehyde (1500mg) was suspended in freshly distilled pyrrole (500mL) and stirred under nitrogen for 2.5 hours at 55°C. Trifluoroacetic acid (TFA, 530uL) was then added dropwise to the solution and stirred for another 1.5 hours. The solution was then cooled to room temperature followed by the addition of sodium hydroxide (817mg, 20.4mmol) and stirred for one hour. The Unreacted pyrrole was then removed via distillation, affording a brown viscous oil which was extracted with water and chloroform three times. The product was purified on silica column with dichloromethane as the eluent to afford a pale white powder as the product. Yield: 2.96g, 22.8mmol (34.8%). ^{1}H-NMR (500MHz, chloroform-D, ppm): δ= 7.57 (s, 2H), 6.62 (d. 2H), 6.18 (d, 4H), 3.94 (s, 2H).

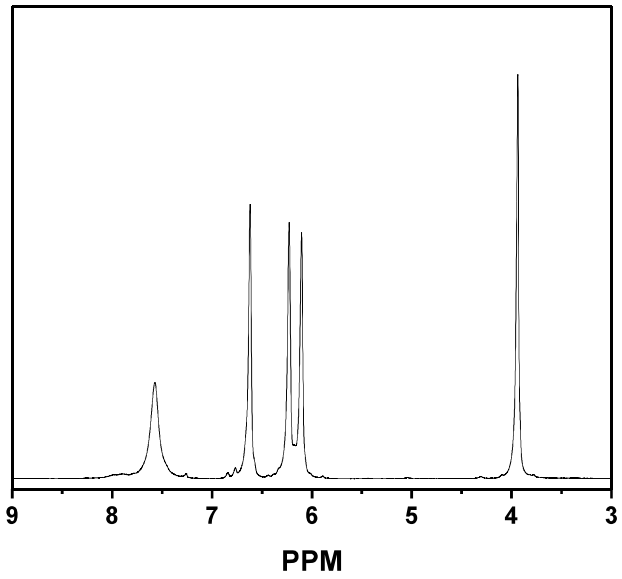

Figure 2-10. The ^{1}H-NMR of 2,2'-dipyrromethane in chloroform.

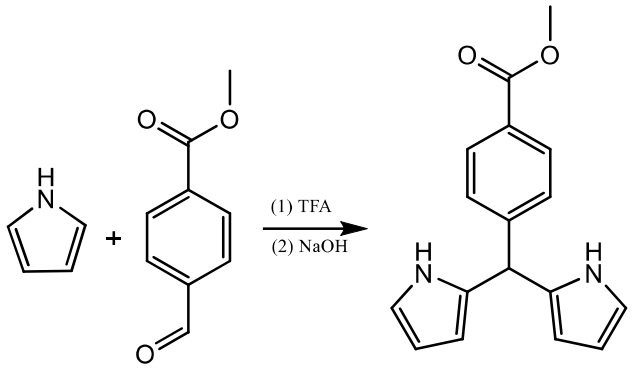

Scheme 2-4. Synthesis of 5-(4-Carbomethoxyphenyl)dipyrromethane.[1]

Distilled pyrrole (34.8mL, 500mmol) was combined with methyl-4-formylbenzoate (6.0g, 36. 8mmol) and degassed for 30 minutes. TFA (220uL, 2.8mmol) was then added dropwise to the solution and stirred in the dark at room temperature for four hours. The solution was then diluted with chloroform and washed with 0.1M NaOH (aq) and water twice. The chloroform was removed with a rotary evaporator while the unreacted pyrrole was removed via vacuum distillation. The brown viscous oil was then purified on a silica column with chloroform as the eluent to afford a

light brown solid. The resulting solid was then rinsed with cold ethyl acetate to obtain a pale gray solid as the product. Yield: 2.1g, 7.1mmol (19.2%). ^{1}H-NR (500MHz, chloroform-D, ppm): δ = 7.97 (d,4H), 7.27 (m, 2H). 6.71 (d, 2H), 6.16 (d, 2H), 5.89 (s, 2H), 5.53 (s, 1H), 3.9 (s, 3H).

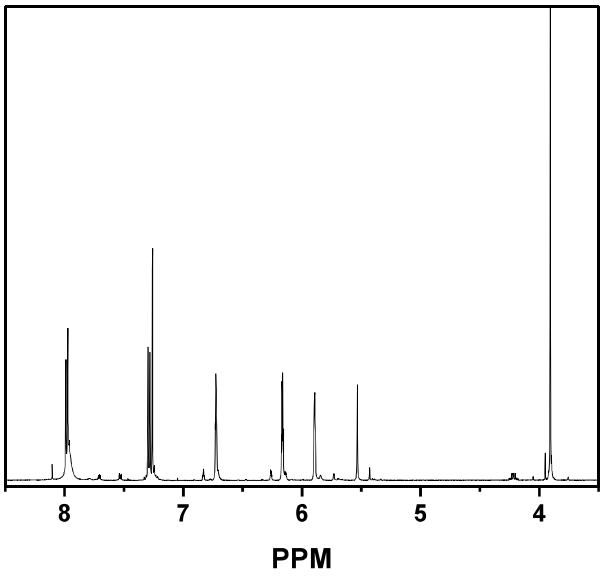

Figure 2-11. The ^{1}H-NMR of 5-(4-Carbomethoxyphenyl)dipyrromethane in chloroform.

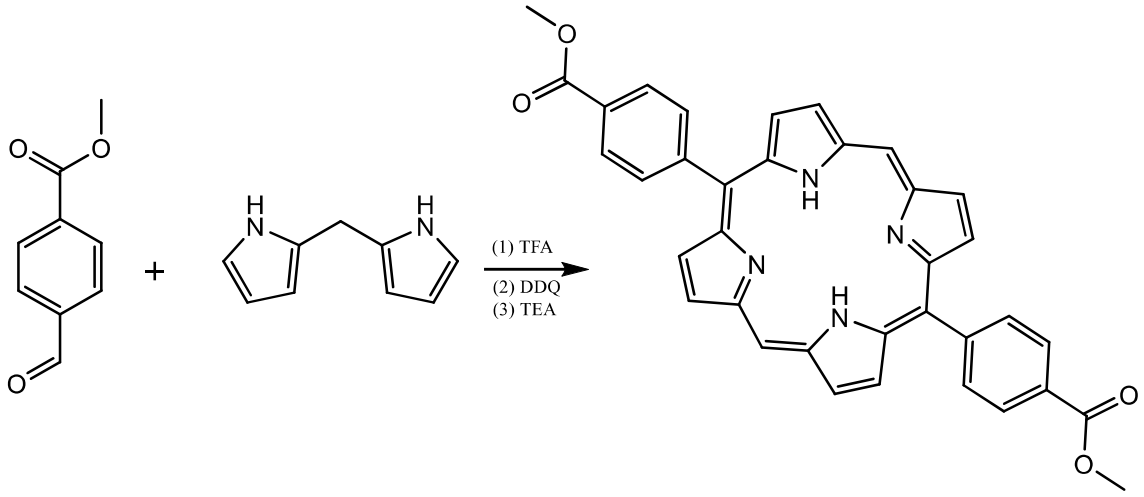

Scheme 2-5. Synthesis of 5,15-di(p-methyl-benzoato)porphyrin (Me_2DBP).

Methyl-4-formylbenzoate (520 mg, 3.16 mmol) and dipyrromethane (463mg, 3.16mmol) were added to a round bottom flask. 500mL of anhydrous dichloromethane was added to the flask and degassed for 30 minutes. Trifluoroacetifc acid (0.5mL, 6.47mmmol) was added dropwise via syringe. The mixture was stirred at room temperature in the dark for four hours. After, 2,3-dichloro-5,6-dicyano-1,4benzoquinone (DDQ, 1085mg, 4.74mmol) was added and allowed to stir for another one hour. The reaction was subsequently quenched with triethylammine (TEA, 8ml, 57.3mmol). The solvent was removed with a rotary evaporator and the resulting solid was purified on a silica column using a chloroform ethyl acetate mixture (9:1) as the eluent to give a deep purple solid as the product. Yield: 290mg, 0.50mmmol (31.6%). ^{1}H-NMR (500MHz, chloroform-D, ppm): δ =10.37 (s, 2H), 9.47 (d, 4H), 9.10 (d, 4H), 8.49 (d, 4H), 8.36(d, 4H), 4.15 (s, 6H), -3.12 (s, 2H).

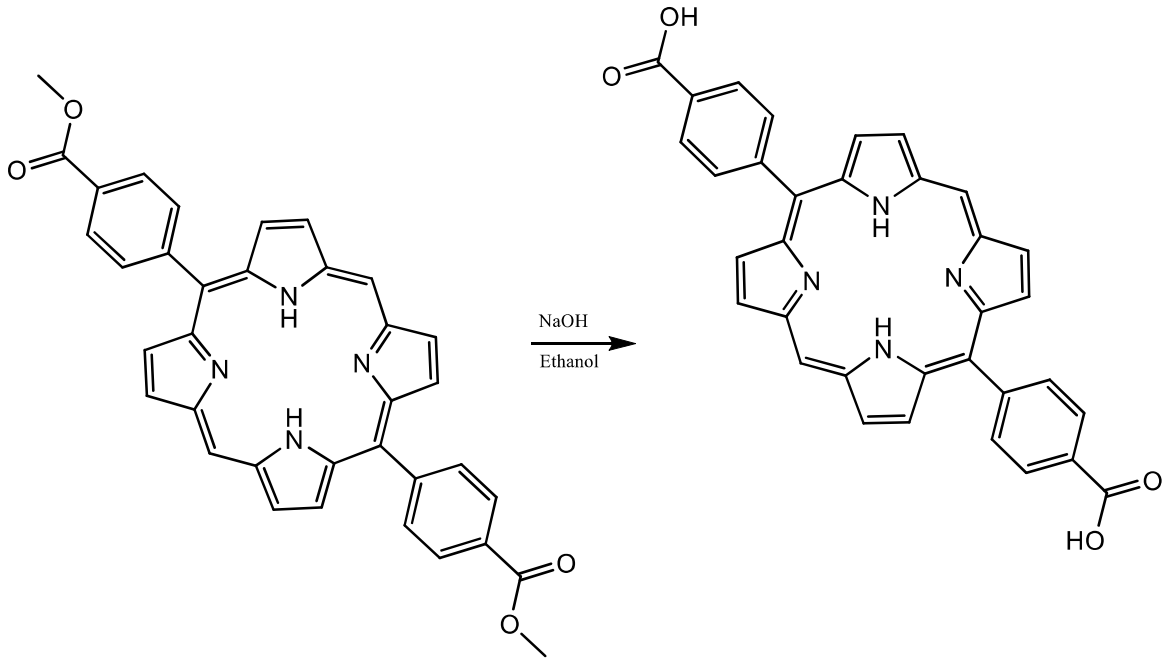

Scheme 2-6. Synthesis of 5, 15-di(*p*-benzoato)porphyrin (H_2DBP).

Me_2DBP (290mg, 0.50mmol) was dissolved in a mixture of 1:1 ethanol and 6M NaOH. The solution was heated to reflux under nitrogen overnight. The solution was then cooled to room temperature upon which it was acidified to pH 2 with 2M HCl. The solid was collected and washed via centrifugation three times with water and dried overnight under vacuum to afford the maroon product. Yield: 257mg, 46.5mmol (93% yield). ^{1}H-NMR (500MHz, dimethyl sulfoxide-D_6, ppm): δ =13.33 (s, 2H), 10.69 (s, 2H), 9.69 (d, 4H), 9.06 (d, 4H), 8.43 (m, 8H), -3.35 (s, 2H).

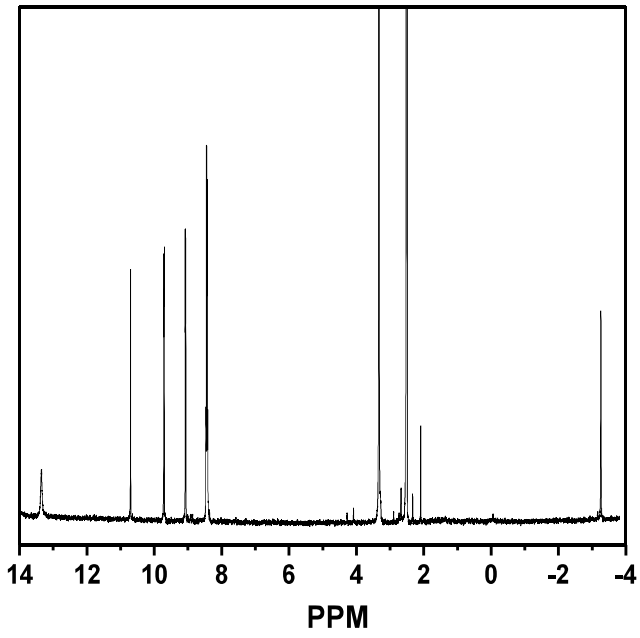

Figure 2-12. The ^{1}H-NMR of H_2DBP in $(CD_3)_2SO$.

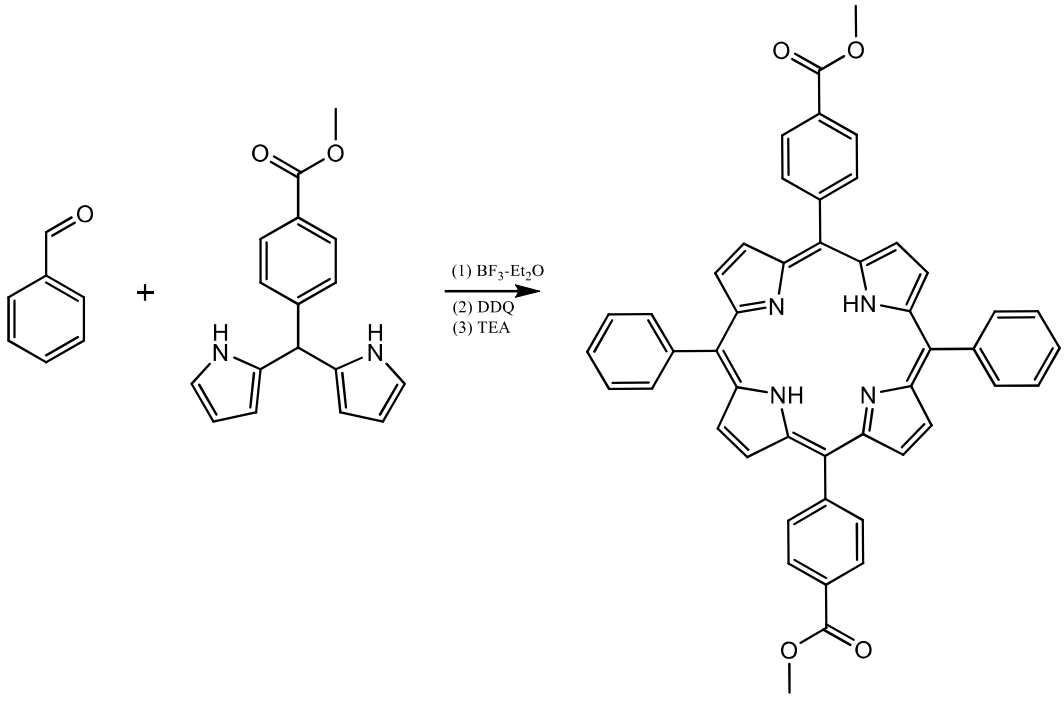

Scheme 2-7. Synthesis of 5,15-di(*p*-methyl-benzoato)-10, 20-diphenyl-porphyrin (Me_2DPDBP).

5-(4-Carbomethhoxyphenyl)dipyrromethane (500mg, 1.8mmol) was combined with benzaldehyde (192uL, 1.8mmol) in 250mL of chloroform. The solution was degassed for one hour followed by the addition of boron trifluoride diethyl etherate (BF_3-Et_2O, 230uL, 1.8mmol). The resulting mixture was stirred at room temperature in the dark for two hours under nitrogen. Subsequently, DDQ (720mg, 3.14mmol) was added to mixture and stirred overnight. The final reaction mixture was quenched with TEA (2mL, 14.32mmol). The solvent was removed with a rotary evaporator and the resulting product was purified using column chromatography on a silica gel with chloroform as the eluent. Yield: (95mg, 0.13mmol (14.4%). ^{1}H-NMR (500MHz, chloroform-D, ppm): δ =8.89 (m, 8H), 8.47(d, 4H), 8.34 (d, 4H), 8.25 (m, 4H), 7.78 (d, 6H), 4.14 (s, 6H), -2.71 (s, 2H).

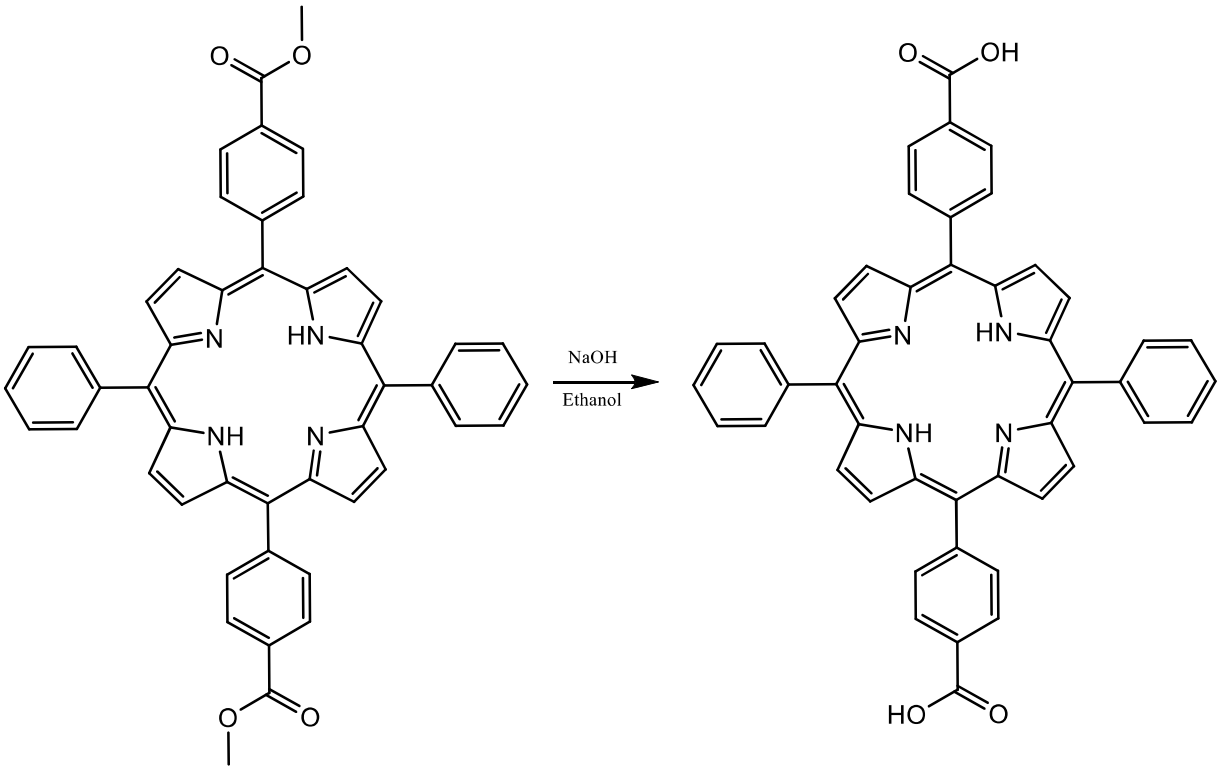

Scheme 2-8. Synthesis of 5,15-di(*p*-benzoato)-10,20-diphenyl-porphyrin (H_2DPDBP).

Me_2DPBP (95mg, 0.50mmol) was dissolved in a mixture of 1:1 ethanol and 6M NaOH. The solution was heated to reflux under nitrogen overnight. The solution was then cooled to room temperature upon which it was acidified to pH 2 with 2M HCl. The solid was collected and washed via centrifugation three times with water and dried overnight under vacuum to afford the dark purple product. Yield: 88mg, 12.3mmol (95% yield). ^{1}H-NMR (500MHz, dimethyl sulfoxide-D_6, ppm): δ =13.33 (s, 2H), 8.83 (d, 8H), 8.33 (dd, 8H), 8.21 (d, 4H), 7.83 (d, 6H), -2.95 (s, 2H).

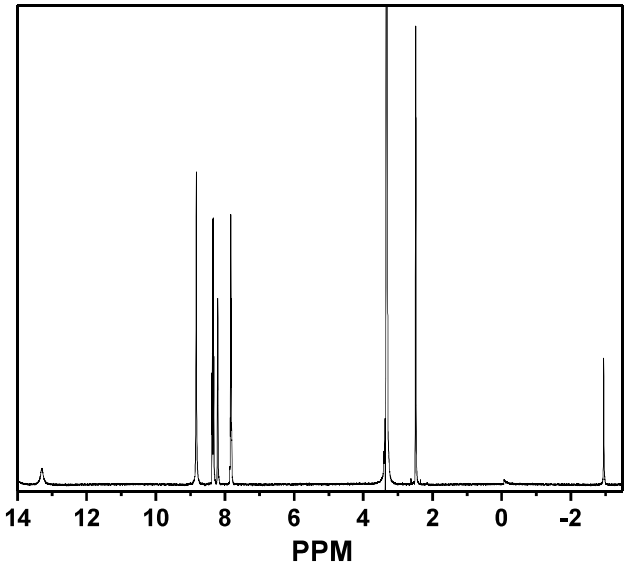

Figure 2-13. The ^{1}H-NMR of H_2DPDBP in $(CD_3)_2SO$.

2.6.2 Synthesis of Metal-Organic Frameworks

Synthesis of the Zr_6-M-DBP: H_2DBP (1.5mg, 2.7 μmol), zirconium(IV) chloride solution (30uL, 20mg/ml in N,N-dimethylformamide (DMF)), and TFA (2uL, 26umol) were combined in a half dram vial and heated at 90°C oven for three days. A dark red powder was collected by centrifugation and washed with DMF three times. After, the resulting material was combined with a mixture of $ZnCl_2$ and $CoCl_2$-$6H_2O$ (10 equivalents of metal based on porphyrin) in DMF and

heated at 90 ˚C for 24 hours followed by subsequent washing with ethanol to yield the final product (~40% yield).

Synthesis of Zr_6-M-DPDBP: H_2DPDBP (1.5mg, 2.1 μmol), $ZrCl_4$ solution (27uL, 20mg/ml in DMF), and TFA (1uL, 13umol) were combined in a half dram vial and heated at 90°C for three days. A dark purple powder was collected by centrifugation and washed with DMF three times. After, the resulting material was combined with a mixture of $ZnCl_2$ and $CoCl_2$-$6H_2O$ (10 equivalents of metal based on porphyrin) in DMF and heated at 90 ˚C for 24 hours followed by subsequent washing with ethanol to yield the final product (~30 % yield).

Synthesis of the Zr_{12}-M-DBP: H_2DBP (1.75mg, 3.2 μmol), zirconium(IV) chloride (0.727 mg, 3.2 μmol), acetic acid (55 μL, 961 μmol), 5 μL H_2O, and 1 mL DMF were combined in a half dram vial and heated at 85°C oven for two days. A dark red powder was collected by centrifugation and washed with DMF three times. After, the resulting material was combined with a mixture of $ZnCl_2$ and $CoCl_2$-$6H_2O$ (10 equivalents of metal based on porphyrin) in DMF and heated at 90 ˚C for 24 hours followed by subsequent washing with ethanol to yield the final product (~50% yield).

2.5 References

1. Loeckenhoff, R.; Dimroth, F.; Oliva, E.; Ohm, A.; Wilde, J.; Faiman, D.; Biryukov, S.; Melnichak, V.; Kabalo, S.; Bokobza, D.; Bett, A. W., Development, characterisation and 1000 Suns outdoor tests of GaAs monolithic interconnected module (MIM) receivers. *Prog. Photovoltaics* **2008,** *16* (2), 101-112.

2. Li, S.-L.; Xu, Q., Metal-organic frameworks as platforms for clean energy. *Energy Environ. Sci.* **2013,** *6* (6), 1656-1683.

3. Kudo, A.; Miseki, Y., Heterogeneous photocatalyst materials for water splitting. *Chem. Soc. Rev.* **2009,** *38* (1), 253-278.

4. Pullen, S.; Fei, H.; Orthaber, A.; Cohen, S. M.; Ott, S., Enhanced photochemical hydrogen production by a molecular diiron catalyst incorporated into a metal-organic framework. *J. Am. Chem. Soc.* **2013,** *135* (45), 16997-17003.

5. Fateeva, A.; Chater, P. A.; Ireland, C. P.; Tahir, A. A.; Khimyak, Y. Z.; Wiper, P. V.; Darwent, J. R.; Rosseinsky, M. J., A Water-Stable Porphyrin-Based Metal-Organic Framework Active for Visible-Light Photocatalysis. *Angew. Chem., Int. Ed.* **2012,** *51* (30), 7440-7444, S7440/1-S7440/17.

6. Horiuchi, Y.; Toyao, T.; Saito, M.; Mochizuki, K.; Iwata, M.; Higashimura, H.; Anpo, M.; Matsuoka, M., Visible-Light-Promoted Photocatalytic Hydrogen Production by Using an Amino-Functionalized Ti(IV) Metal-Organic Framework. *J. Phys. Chem. C* **2012,** *116* (39), 20848-20853.

7. Sumida, K.; Rogow, D. L.; Mason, J. A.; McDonald, T. M.; Bloch, E. D.; Herm, Z. R.; Bae, T.-H.; Long, J. R., Carbon Dioxide Capture in Metal-Organic Frameworks. *Chem. Rev. (Washington, DC, U. S.)* **2012,** *112* (2), 724-781.

8. Li, J.-R.; Sculley, J.; Zhou, H.-C., Metal-Organic Frameworks for Separations. *Chem. Rev. (Washington, DC, U. S.)* **2012,** *112* (2), 869-932.

9. Cui, Y.; Yue, Y.; Qian, G.; Chen, B., Luminescent Functional Metal-Organic Frameworks. *Chem. Rev. (Washington, DC, U. S.)* **2012,** *112* (2), 1126-1162.

10. Lee, J. Y.; Farha, O. K.; Roberts, J.; Scheidt, K. A.; Nguyen, S. B. T.; Hupp, J. T., Metal-organic framework materials as catalysts. *Chem. Soc. Rev.* **2009,** *38* (5), 1450-1459.

11. Huxford Rachel, C.; Della Rocca, J.; Lin, W., Metal-organic frameworks as potential drug carriers. *Curr Opin Chem Biol* **2010,** *14* (2), 262-8.

12. Wang, C.; deKrafft, K. E.; Lin, W., Pt Nanoparticles@Photoactive Metal-Organic Frameworks: Efficient Hydrogen Evolution via Synergistic Photoexcitation and Electron Injection. *J. Am. Chem. Soc.* **2012,** *134* (17), 7211-7214.

13. Lin, J.; Hu, X.; Zhang, P.; Van Rynbach, A.; Beratan, D. N.; Kent, C. A.; Mehl, B. P.; Papanikolas, J. M.; Meyer, T. J.; Lin, W.; Skourtis, S. S.; Constantinou, M., Triplet Excitation Energy Dynamics in Metal-Organic Frameworks. *J. Phys. Chem. C* **2013,** *117* (43), 22250-22259.

14. Kent, C. A.; Mehl, B. P.; Ma, L.; Papanikolas, J. M.; Meyer, T. J.; Lin, W., Energy transfer dynamics in metal-organic frameworks. *J. Am. Chem. Soc.* **2010,** *132* (37), 12767-12769.

15. Lee, C. Y.; Farha, O. K.; Hong, B. J.; Sarjeant, A. A.; Nguyen, S. B. T.; Hupp, J. T., Light-Harvesting Metal-Organic Frameworks (MOFs): Efficient Strut-to-Strut Energy Transfer in Bodipy and Porphyrin-Based MOFs. *J. Am. Chem. Soc.* **2011,** *133* (40), 15858-15861.

16. Lu, K.; He, C.; Lin, W., Nanoscale Metal-Organic Framework for Highly Effective Photodynamic Therapy of Resistant Head and Neck Cancer. *J. Am. Chem. Soc.* **2014,** *136* (48), 16712-16715.

17. Miao, J.; Zhu, L., Hydrogen Bonding Induced Supramolecular Self-Assembly of Linear Doubly Discotic Triad Supermolecules. *Chem. - Asian J.* **2010,** *5* (7), 1634-1641.

18. Dai, R.; Peng, F.; Ji, P.; Lu, K.; Wang, C.; Sun, J.; Lin, W., Electron Crystallography Reveals Atomic Structures of Metal-Organic Nanoplates with M12(μ3-O)8(μ3-OH)8(μ2-OH)6 (M = Zr, Hf) Secondary Building Units. *Inorg. Chem.* **2017,** *56* (14), 8128-8134.

19. Newville, M., IFEFFIT: interactive XAFS analysis and FEFF fitting. *J. Synchrotron Radiat.* **2001,** *8* (2), 322-324.

20. Yang, J.; Huang, P., A Study of Cobalt(II) Porphyrins on Their Oxygen-Binding Behaviors and Oxygen-Facilitated Transport Properties in Polymeric Membranes. *Chem. Mater.* **2000,** *12* (9), 2693-2697.

21. Hafizovic Cavka, J.; Jakobsen, S.; Olsbye, U.; Guillou, N.; Lamberti, C.; Bordiga, S.; Lillerud, K. P., A New Zirconium Inorganic Building Brick Forming Metal Organic Frameworks with Exceptional Stability. *J. Am. Chem. Soc.* **2008,** *130* (42), 13850-13851.

22. Rodriguez, J.; Kirmaier, C.; Holten, D., Optical properties of metalloporphyrin excited states. *J. Am. Chem. Soc.* **1989,** *111* (17), 6500-6.

23. Natali, M.; Luisa, A.; Iengo, E.; Scandola, F., Efficient photocatalytic hydrogen generation from water by a cationic cobalt(ii) porphyrin. *Chem. Commun. (Cambridge, U. K.)* **2014,** *50* (15), 1842-1844.

24. Lu, K. H., Chunbai.; Guo, N.; Chan, C.; Ni, K. L., Guangxu.; Tang, H.; Pelizzari, C.; Fu, Y.-X. S., Michael T.; Weichselbaum, R. R. L., Wenbin., Nature Biomedical Engineering: 2018; Vol. 2, pp 600-610.

25. Kellett, R. M.; Spiro, T. G., Cobalt(I) porphyrin catalysts of hydrogen production from water. *Inorg. Chem.* **1985,** *24* (15), 2373-7.

26. Walker, F. A.; Beroiz, D.; Kadish, K. M., Electronic effects in transition metal porphyrins. 2. The sensitivity of redox and ligand addition reactions in para-substituted tetraphenylporphyrin complexes of cobalt(II). *J. Am. Chem. Soc.* **1976,** *98* (12), 3484-9.

27. Quimby, D. J.; Longo, F. R., Luminescence studies on several tetraarylporphins and their zinc derivatives. *J. Am. Chem. Soc.* **1975,** *97* (18), 5111-17.

28. Dempsey, J. L. Hydrogen evolution catalyzed by cobaloximes. 2011.

29. Bhattacharjee, A.; Weiss, A. K. H.; Artero, V.; Field, M. J.; Hofer, T. S., Electronic Structure and Hydration of Tetramine Cobalt Hydride Complexes. *J. Phys. Chem. B* **2014,** *118* (20), 5551-5561.

30. Lan, G.; Zhu, Y.-Y.; Veroneau, S. S.; Xu, Z.; Micheroni, D.; Lin, W., Electron Injection from Photoexcited Metal-Organic Framework Ligands to Ru2 Secondary Building Units for Visible-Light-Driven Hydrogen Evolution. *J. Am. Chem. Soc.* **2018,** *140* (16), 5326-5329.

CHAPTER 3

Efficient Electrocatalytic Proton Reduction by a Carbon Nanotube-Supported Metal-Organic Framework

3.1 Introduction

The ever-changing energy landscape dictates the need for renewable and clean energy sources. Of the numerous proposed solutions, the hydrogen economy stands out for the ubiquity of hydrogen in water and hydrogen's ability to serve as the energy source for transportation as well as electricity production. Paramount to this objective is the hydrogen evolution reaction (HER). However, the large scale production of hydrogen remains a technically difficult and expensive endeavor, with the bulk of hydrogen production coming from the steam reforming of natural gas in the form of syngas.[1]

Typically, the HER is dominated by inorganic materials which fall near the top of the kinetic volcano plot based on the strength of the metal-hydrogen bond. [2, 3] However these materials are comprised of precious metals including platinum, rhenium, ruthenium, and iridium, making their large-scale implementation prohibitively expensive.

To overcome the scarcity and high costs of precious metal electrocatalysts, numerous molecular systems and semiconductors have been developed based on earth-abundant metals including cobalt,[4-8] nickel,[9-11] iron, [12, 13] and molybdenum.[14-16] Tuning of organic ligands has afforded molecular HER catalysts with low overpotentials and catalytic activity. However, the materials are often water insoluble and limited by diffusion to the electrode in electrochemical setups.

Metal-organic frameworks (MOFs) provide a unique platform to solve the issues that plague molecular electrocatalysts for the hydrogen evolution reaction. They are highly porous allowing for rapid mass transport, they are catalytically active due to the large number of coordinatively unsaturated metal-sites present, and their crystalline nature allows for easy identification of catalytic centers. [17] Although MOFs have been explored as photocatalysts for HER,[18-21] they have not found use as electrocatalysts because sluggish inter-ligand electron transfer kinetics. The only metal sites that can be reduced in the presence of a cathodic potential are those within contact of the electrode surface. The rest of the material generally remains in its neutral state as a result of poor atomic overlap and large distances between ligands slowing down electron transfer. To improve the conductive nature of MOFs, most electrocatalytic MOF systems require the MOF to be pyrolyzed to yield a highly conductive material with metal nanoparticles confined within the native pores. [22-24] Alternatively, efficient electrolysis was reported for MOF species which are very thin being comprised of only a few layers, have open catalytic sties, and/or are covalently tethered to the electrode surface. [25-34]

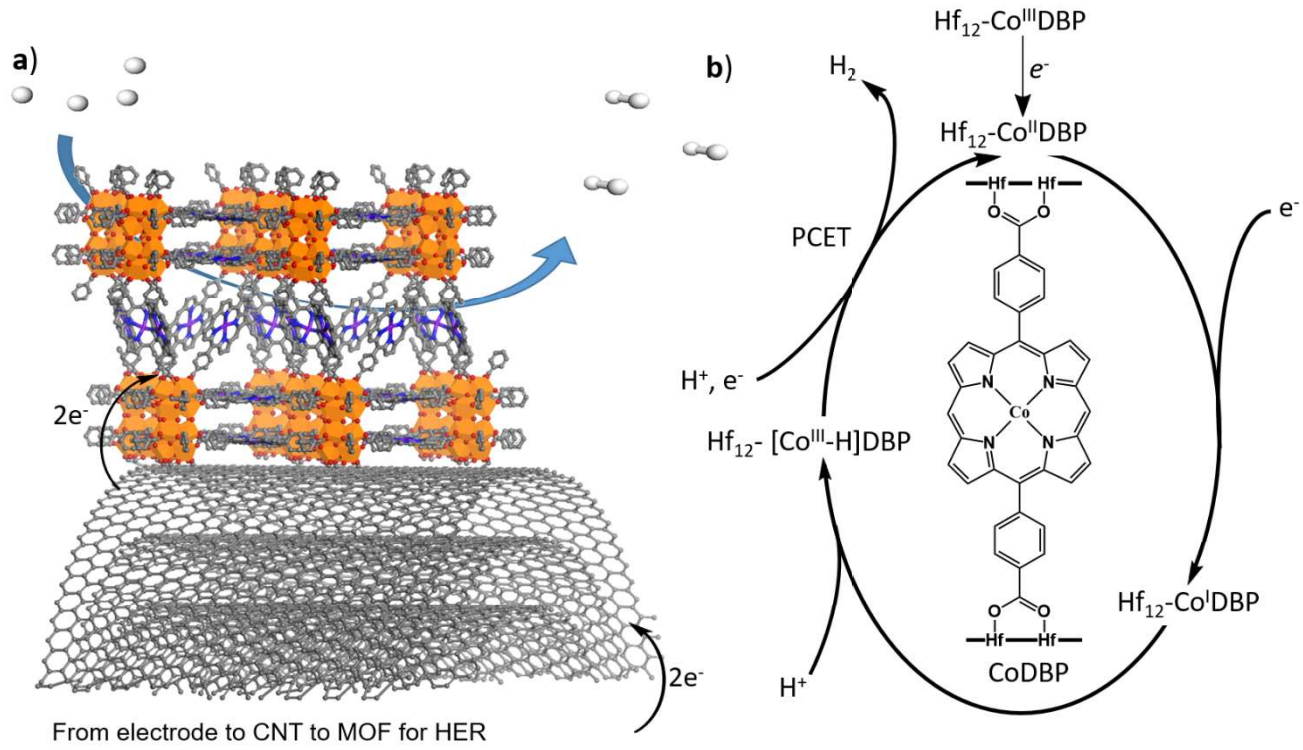

Scheme 3-1. a) Covalent attachment of Hf_{12}-CoDBP to CNTs enhances electrocatalytic HER at CoDBP centers. b) The HER is proposed to proceed through a Co^{III}-H intermediate. Orange = Hf, purple = Co, black = C, red= O, blue = N, and white = H.

We recently reported a series of MOFs comprised of M_{12} (M = Zr and Hf) secondary building units (SBUs) and linear dicarboxylate ligands that fulfill many requirements of efficient electrocatalytsts.[35-37] These MOFs are a few nanometers thick with short inter-ligand distances (<1 nm), leading to efficient electron transfer through the MOF nanoplates. They are stable in aqueous environments owing to the strong bond between Zr^{4+} ions and carboxylate groups. Herein we report the design of a Hf_{12} MOF, Hf_{12}-CoDBP, comprised of Co-metalated 5,15-di(*p*-benzoato)-porphyrin (CoDBP) bridging ligands as an active HER electrocatalyst in acidic media (Figure 3-1). Molecular Co-porphyrin systems have previously been shown to effectively catalyze the HER.[24, 38, 39] Furthermore, we show that covalent tethering of Hf_{12}-CoDBP to multi-walled carbon

nanotubes (CNTs) significantly improves electrical conductivity, leading to drastically enhanced HER turnover number (TON) and turnover frequency (TOF) for the Hf_{12}-CoDBP/CNT hybrid.

3.2 Results and Discussion

3.2.1 Material Synthesis and Characterization

Hf_{12}-CoDBP with the ideal composition of $Hf_{12}O_8(\mu_3\text{-}OH)_8(\mu_2\text{-}OH)_6(CoDBP)_9$ was prepared via a solvothermal reaction between CoDBP and $HfCl_4$ in DMF at 85 °C for 72h. Alternatively, Hf_{12}-CoDBP was prepared by metalation of known Hf_{12}-H_2DBP with $CoCl_2$ in DMF at 80 °C.[40] PXRD studies showed that both procedures afforded the same structure with four major peaks at 2θ = 3.8, 6.55, 7.57, and 9.99 ° corresponding to hk0 indices (Figure 3-1); most of the other PXRD peaks are unobservable due to inherent defects along the *c*-direction of the lattice.[37] Hf_{12}-CoDBP has a diameter ranging from 30 to 100 nm by TEM (Figure 3-2) and a thickness ranging from 10 to 40 nm by atomic force microscopy (AFM, Figure 3-3), correlating to the stacking of 3 to 12 unit cells along the c-axis. The thickness of Hf_{12}-CoDBP is thus smaller than that of the electric double layer, making it a potential candidate for electrocatalysis.

Hf_{12}-CoDBP/CNT was synthesized by heating a DMF solution of H_2(CoDBP) and $HfCl_4$ in the presence of carboxylated multi-walled CNTs at 85 °C for 72 h. The carboxylate groups on the CNTs allow for direct attachment to the MOF via the SBU, affording a densely packed Hf_{12}-CoDBP/CNT heterostructure with the unchanged plate-like morphology of Hf_{12}-CoDBP (Figure 3-2c, d). PXRD studies indicated that Hf_{12}-CoDBP/CNT adopts the same crystalline structure as Hf_{12}-CoDBP (Figure 3-1), while high resolution TEM (HRTEM) images showed lattice points with inter-SBU distances of 2.7 nm. The Fast Fourier Transform (FFT) of the TEM image showed six-fold symmetry which is consistent with the projection of Hf-CoDBP structure along the (001) direction (Figure 3-2d).

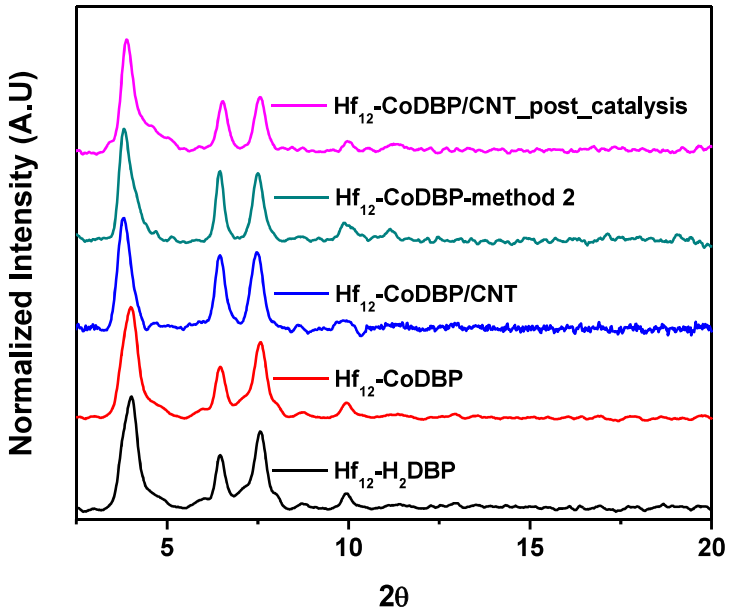

Figure 3-1. PXRD of Hf_{12}-CoDBP/CNT (blue) showed identical peaks to Hf_{12}-CoDBP (red and teal), and Hf_{12}-H_2DBP (black), indicating the Hf_{12}-CoDBP grown on CNT had the same crystalline structure as the parent Hf_{12}-CoDBP.

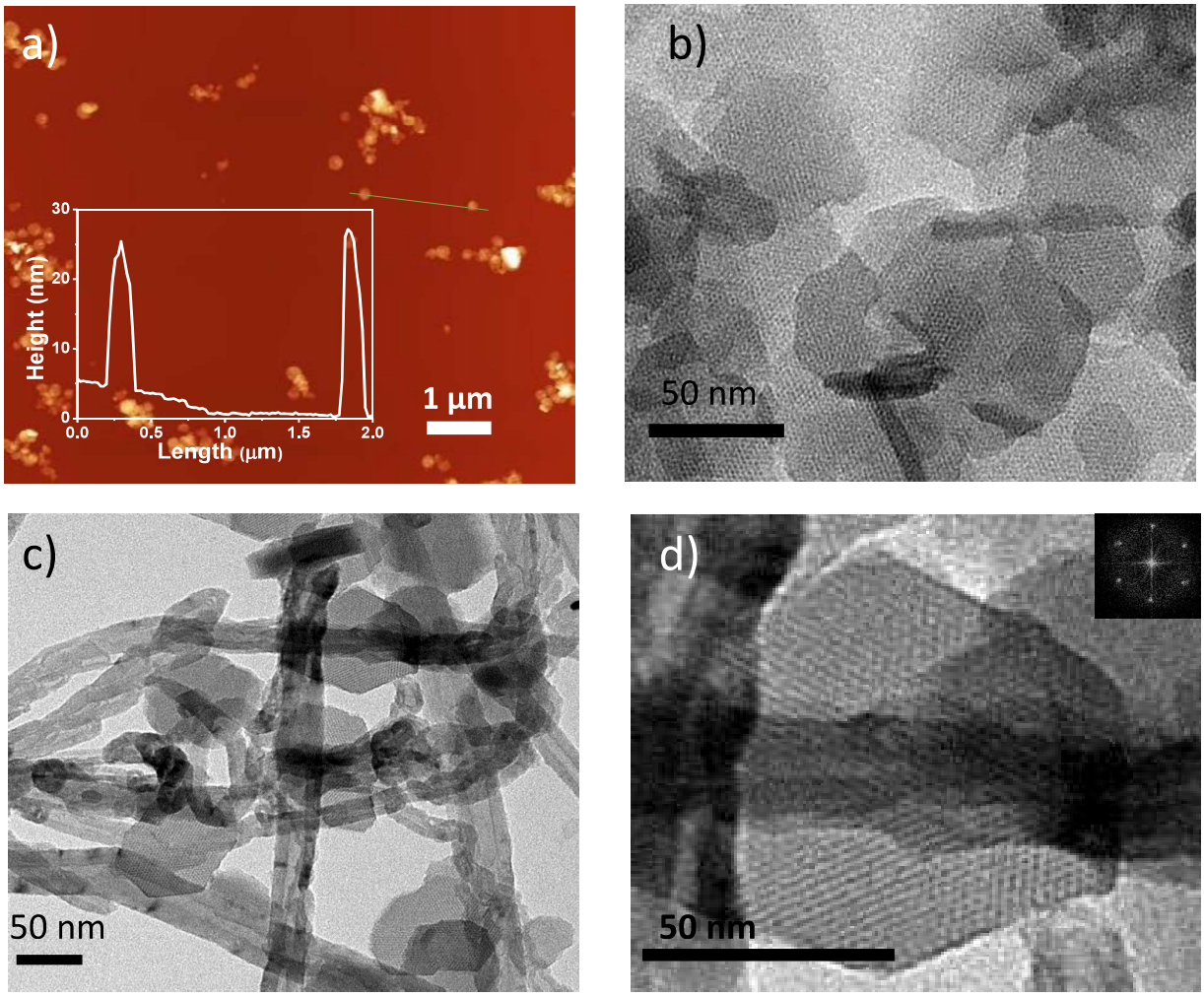

Figure 3-2. a) AFM analysis of Hf_{12}-CoDBP shows 20 and 25 nm thick nanoplates. TEM images of b) Hf_{12}-CoDBP and c, d) Hf_{12}-CoDBP/CNT show the retention of crystalline MOF nanoplate morphology when covalently bound to CNTs. The Fast Fourier Transform in inset of (d) shows expected 6-fold symmetry along the c-axis.

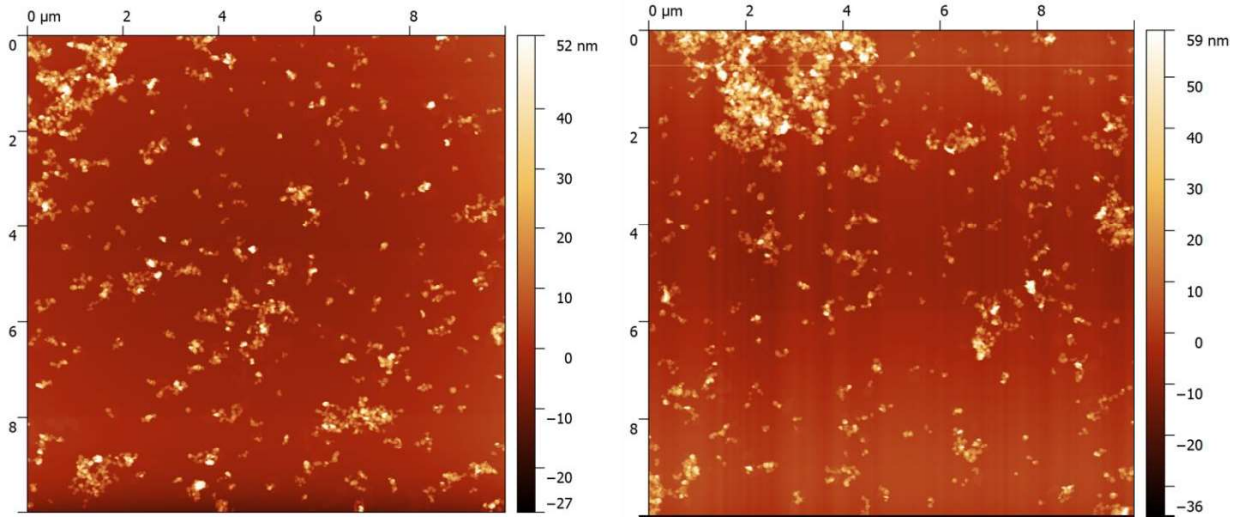

Figure 3-3. AFM images of two different Hf_{12}-DBP samples show consistent shape and thickness ranging from 15 to 40 nm.

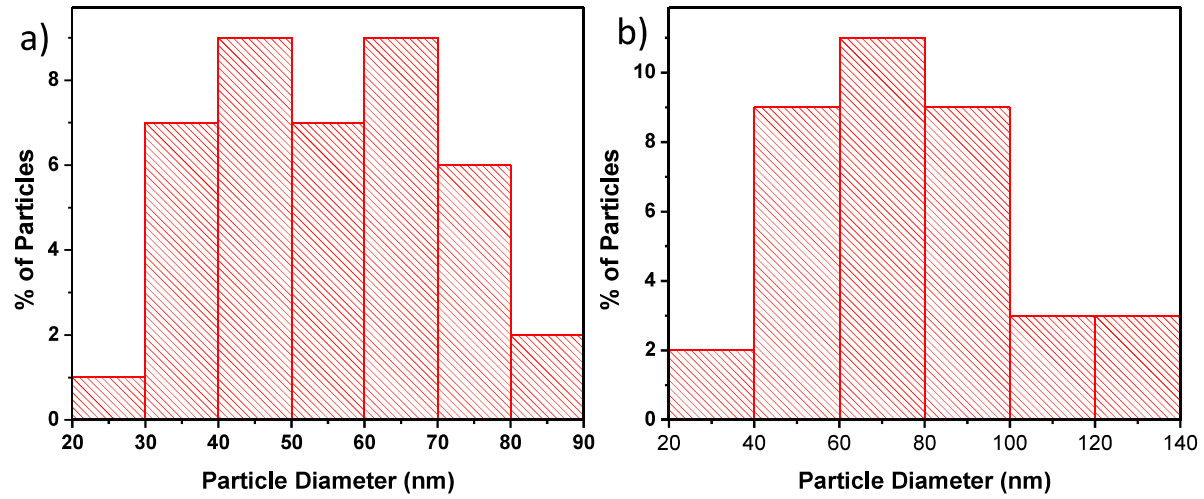

Figure 3-4. Histogram of the Hf_{12}-CoDBP particle sizes from distinct samples, both a) with and b) without CNT functionalization as determined by TEM above and in the primary manuscript.

X-ray photoelectron spectroscopy (XPS) indicated the presence of mixed valent Co^{2+}/Co^{3+} and Hf^{4+} centers in Hf_{12}-CoDBP/CNT (Figure 3-5). Integration of XPS $Co2P_{3/2}$ and $Hf4d_{3/2}$ peaks gave a Hf:Co ratio of 1.78 for Hf_{12}-DBP-Co/CNT (Figure 3-5). Thermogravimetric analysis (TGA) gave a Hf:porphyrin ratio of 1.46 - 1.66 (Figure 3-6) and inductively coupled plasma-mass

spectrometry (ICP-MS) gave a Hf:Co ratio of 1.57:1 for Hf_{12}-DBP-Co/CNT. The Hf:CoDBP ratios from these analyses gave an average Hf:CoDBP ratio of 1.62, which deviates from 1.33 expected for the idealized Hf_{12}-CoDBP structure. The MOF structure of Hf_{12}-CoDBP/CNT is thus highly defected along the c-axis and has an empirical formula of $Hf_{12}O_8(\mu_3\text{-}OH)_8(\mu_2\text{-}OH)_6(CoDBP)_{7.4}$ as no Co^{3+} ions were observed to leach from CoDBP during the MOF growth as determined by the UV-Vis spectra of Hf_{12}-DBP-Co/CNT (Figure 3-7,8).

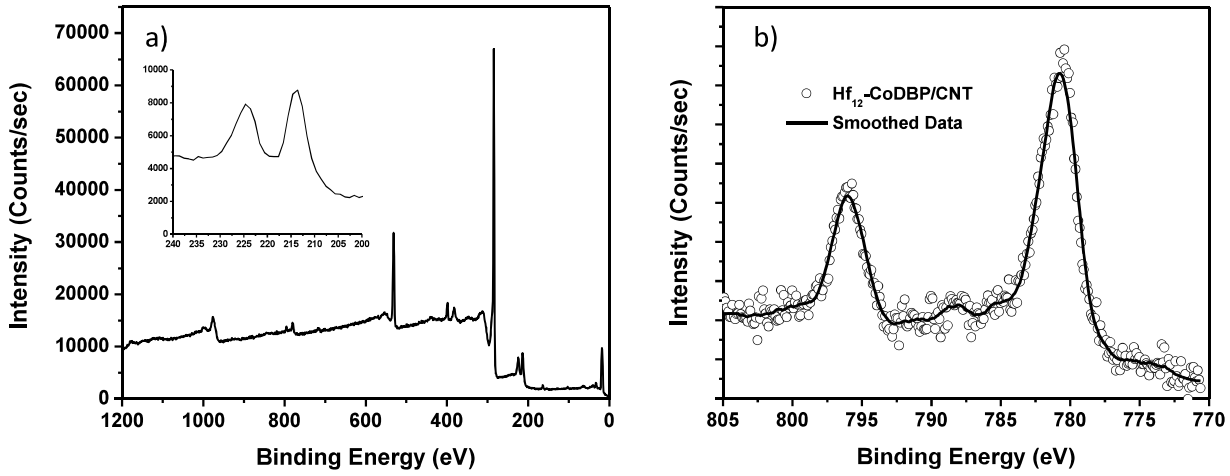

Figure 3-5. a) The XPS spectrum of Hf_{12}-CoDBP/CNT was used to determine the Hf to Co ratio, with the inset graph showing the $Hf4d_{3/2}$ peak. b) The cobalt region of the XPS spectrum shows Co^{III} oxidation state for Hf_{12}-CoDBP/CNT. For XPS integration, relative sensitive factors (RSFs) of 33.12 and 66.88 were used for $Co2p_{3/2}$ and $Hf4d_{3/2}$ peaks, respectively.

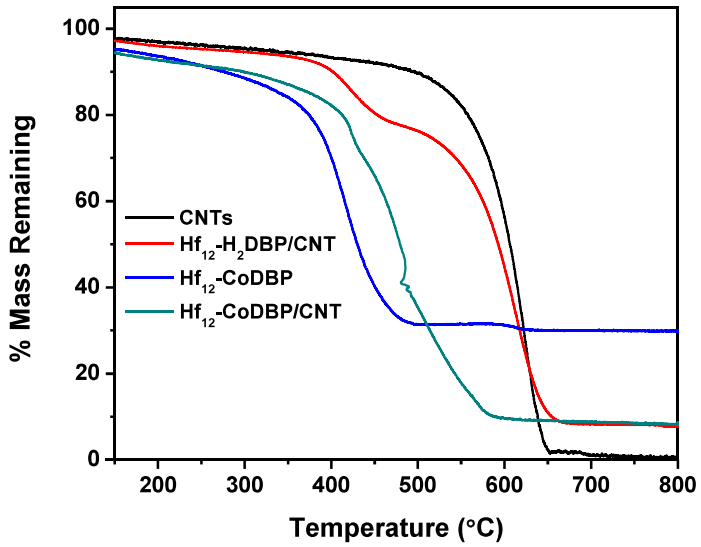

Figure 3-6. Comparison of TGA curves of Hf_{12}-CoDBP/CNT, CNT, and Hf_{12}-CoDBP shows that Hf_{12}-CoDBP/CNT contains ~20 wt% Hf_{12}-CoDBP with a Hf to H_2DBP ligand ratio of 1.66:1 and a Hf to CoDBP ratio of 1.46:1. The first weight at 385 to 470 °C (13.4 %) was assigned to the degradation of the porphyrin moiety into CO_2 and metal oxides. The second weight loss at 485 to 670 °C corresponds to the decomposition of the CNTs. The weight remaining (8.25%) at > 670 °C is attributed to HfO_2. The Hf to ligand ratio was determined from the percent weight loss of porphyrin compared to the percent HfO_2 remaining.

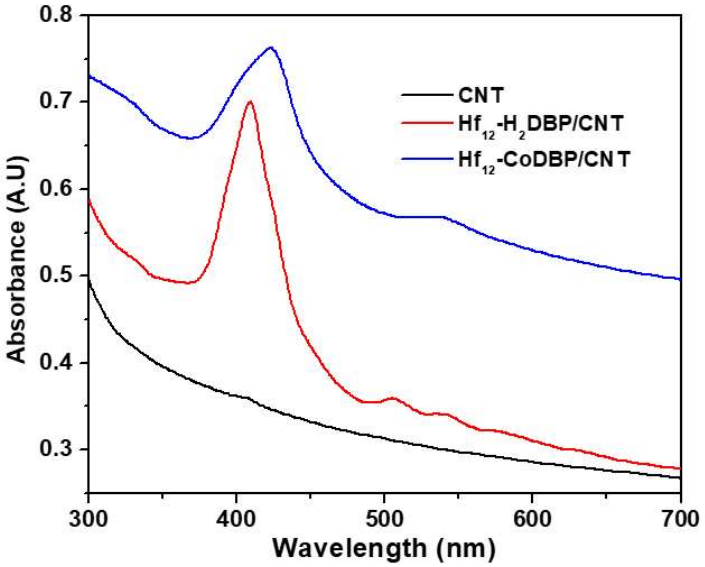

Figure 3-7. UV-Vis spectra of CNTs, Hf_{12}-H_2DBP/CNT and Hf_{12}-CoDBP/CNT in DMF.

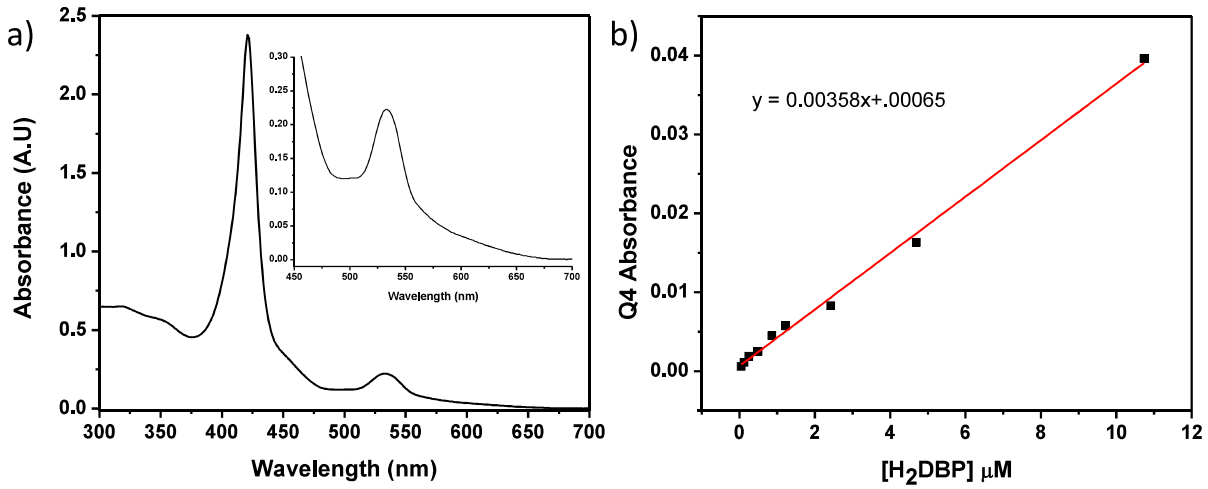

Figure 3-8. UV-Vis spectrum of 40 μM CoDBP taken from the Hf_{12}-CoDBP growth solution (a) shows no loss of the Co center nor emergence of the Q4 band at 630 nm of H_2DBP with H_2DBP detection limits up to 10% of that of the concentration of DBP when in the same medium.

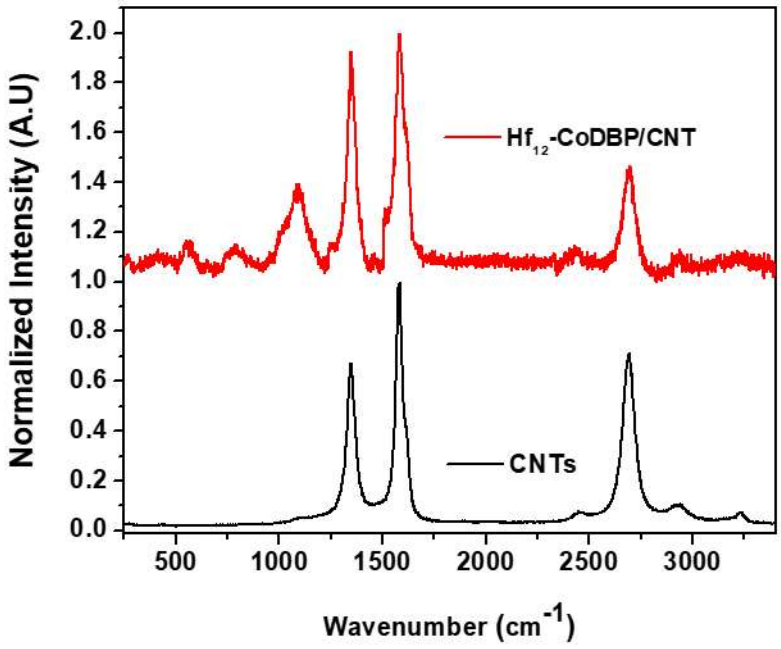

Figure 3-9. The Raman spectra of CNTs and the MOF@CNT sample shows the emergence of a peak at 1100 cm^{-1} in addition to the retention of the native CNT bands.

Nitrogen sorption studies revealed a Brunauer-Emmett-Teller (BET) surface area of 115.44 m^2/g for Hf_{12}-CoDBP/CNT, which is significantly higher than that of untreated CNTs (S_{BET} = 78.12 m^2/g, Figure 3-6) due to the deposition of highly porous Hf_{12}-CoDBP (S_{BET} = 509.3 m^2/g) on CNTs (Figure 3-10). The pore sizes of Hf_{12}-CoDBP/CNT ranged from 2 to 3 nm for the MOF lattice and 4 to 10 nm for the natural porosity of the CNTs (Figure 3-10). The S_{BET} and TGA results thus suggest that Hf_{12}-CoDBP comprises 20-25 % of the overall mass of Hf_{12}-CoDBP/CNT. The high loading of Hf_{12}-CoDBP is also evident in TEM images.

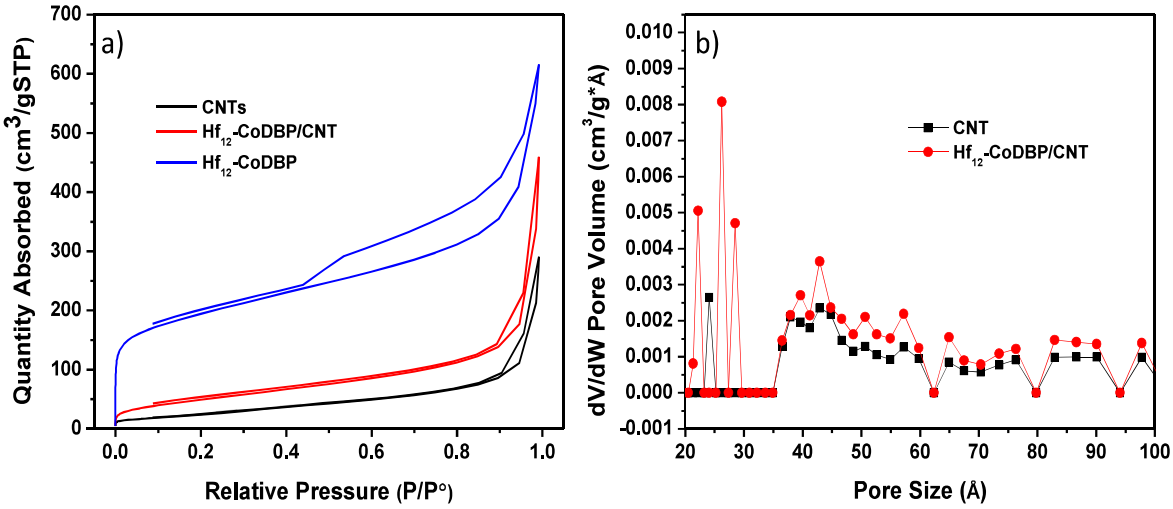

Figure 3-10. Nitrogen sorption isotherms for CNTs, Hf_{12}-CoDBP, and Hf_{12}-CoDBP/CNT afforded BET surface areas of 78.12 m^2/g, 509.3 m^2/g, and 115.14 m^2/g, respectively.

The structural and chemical properties of Hf_{12}-CoDBP lend itself toward electrochemical applications when covalently attached to CNTs. Direct tethering of Hf_{12}-CoDBP to a conductive surface increases the rate of electron transfer to CoDBP catalytic sites. The nanoplate morphology of Hf_{12}-CoDBP places active sites in close proximity to the conductive support, the electrolyte, and the substrate simultaneously. These features not only overcome the diffusion constraint of the active catalyst, but also prevent detrimental bimolecular deactivation pathways as a result of active

site isolation. The deposition of highly porous Hf_{12}-CoDBP on CNTs also increases the number of active sites on the electrode surface.

3.2.2 Electrochemical Results

For all electrochemical methods involving CoMOF@CNT, CoMOF@CNT was dropcasted onto the surface of the electrode and held in place via the intermolecular forces between the electrode and MOF material. Cyclic voltammetry measurements of Hf_{12}-CoDBP, Hf_{12}-CoDBP/CNT, and homogenous H_2CoDBP showed a reversible one electron peak at -0.485 V vs NHE in acetonitrile (ACN), corresponding to the $Co^{II/I}$ reduction peak of CoDBP (Figure 3-11, 12).[41] Upon the addition of 0.026 M trifluoroacetic acid (TFA) as a proton source, the $Co^{I/II}$ anodic peak disappeared with a concurrent increase in current density attributable to catalytic proton reduction. The similar behavior seen in Hf_{12}-CoDBP, Hf_{12}-CoDBP/CNT, and CoDBP indicates an identical catalytic process, likely through the Heyrovsky pathway via a Co^{III}-H intermediate, as the physical constraints of the MOF and the thermodynamics of the system ensure the process proceeds via the unimolecular, homolytic pathway after reduction to a Co^{I} species.

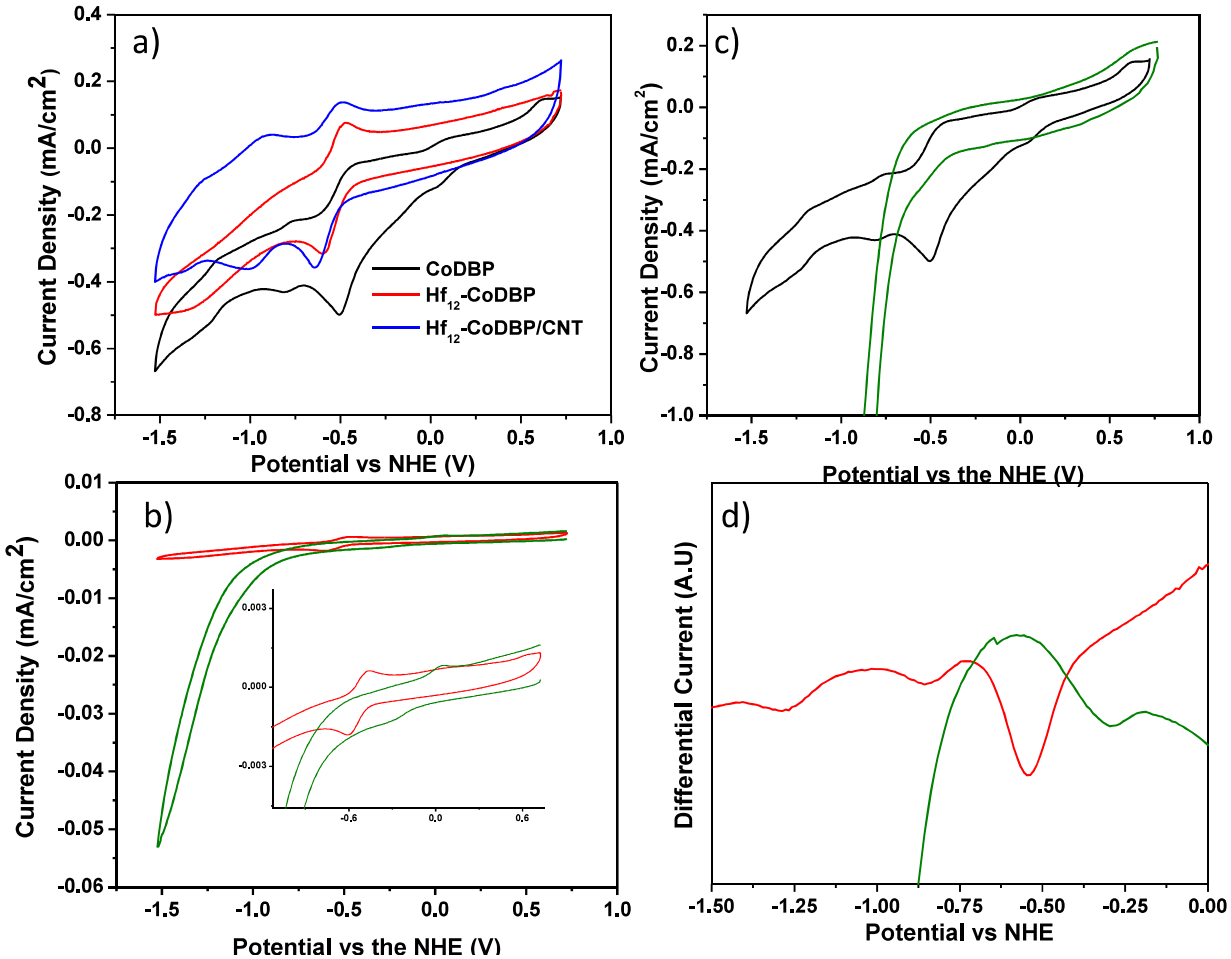

Figure 3-11. a) The CV curves of the homogenous species (black), Hf_{12}-CoDBP (Red), and Hf_{12}-CoDBP/CNT (Blue) in 0.1 M [TBA]PF_6 dissolved in acetonitrile. b,c) The CV curves of H_2(CoDBP) (b) and Hf_{12}-CoDBP (c) with (blue) and without (red) TFA (0.026 M) show similar hydrogen production behavior. d) Differential pulse voltammetry curves of Hf_{12}-CoDBP in acetonitrile with (blue) and without (red) TFA suggest the HER process occurs via protonation of a Co^{III}-H intermediate.

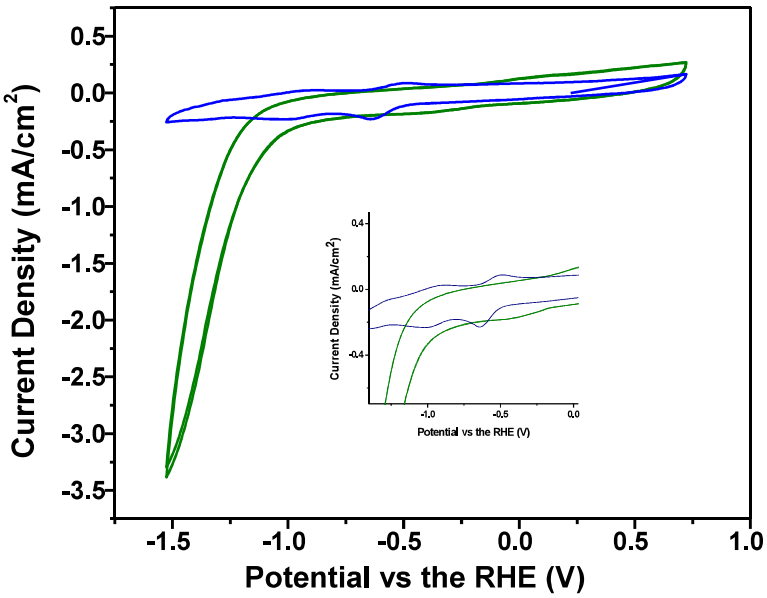

Figure 3-12. Cyclic voltammetry curves of Hf_{12}-CoDBP/CNT in the presence of 0.026 M TFA in acetonitrile show proton reduction consistent with a Co^{III}-H intermediate, vastly outperforming a bare glassy carbon electrode.

Integration of the Co^{II}/Co^{I} anodic peak for the Hf_{12}-CoDBP/CNT species in acetonitrile revealed that 31.9% of total Co species (0.947 nmol by ICP-MS) on the electrode surface were electrochemically active. This value represents a 114 times increase over that of Hf_{12}-CoDBP (Figure 3-13), highlighting the important role of MOF/CNT hybrid in increasing the overall surface area of the electrode to enhance electron injection into the catalytic sites; dropcasting 0.1 mg of Hf_{12}-CoDBP/CNT on a 0.0625 cm^2 glassy carbon electrode yields a catalytically active surface area of 49.6 cm^2. A linear relationship for the log of the current vs the log of the scan rate with a slope of 0.54 was found for Hf_{12}-CoDBP/CNT in ACN, indicating the redox process occurs via a charge hopping mechanism (Figure 3-14). In comparison, Hf_{12}-CpDBP synthesized with non-carboxylated CNTs showed only 0.29% electrochemically active Co sites (Figure 3-15). These results demonstrate the importance of covalent tethering of the MOF to the CNT in achieving good

electrocatalytic activity by increasing the overall surface area of the electron injection into catalytic sites.

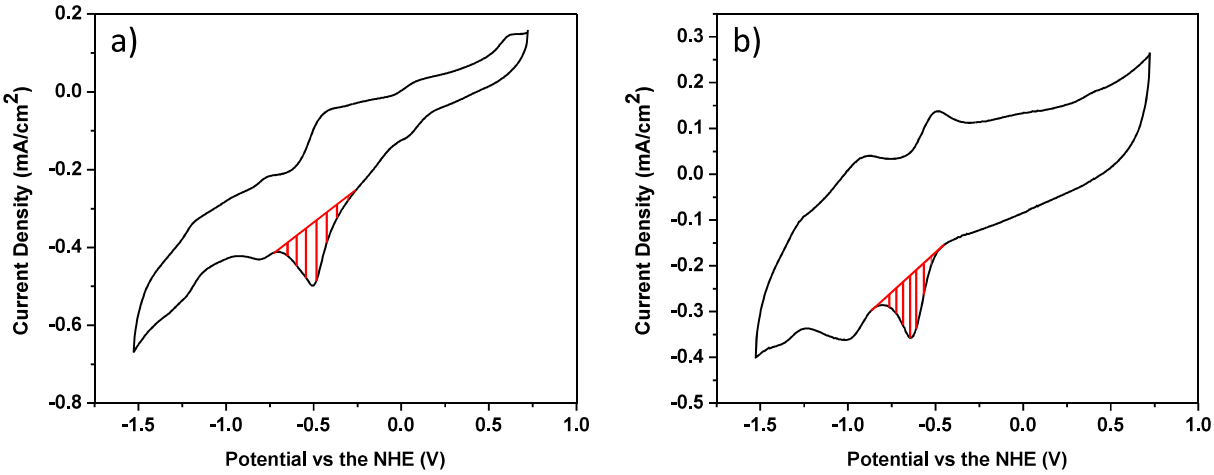

Figure 3-13. a) Comparison of the integrations of the first reductive peaks for Hf_{12}-CoDBP and b) Hf_{12}-CoDBP/CNT shows a 114-fold increase in the percent active sites for the Hf_{12}-CoDBP/CNT material. For a), 0.28% of the 26.1 nmol of Co centers were reduced, while for b), 31.9% of the available 1.58 nmol Co centers were reduced.

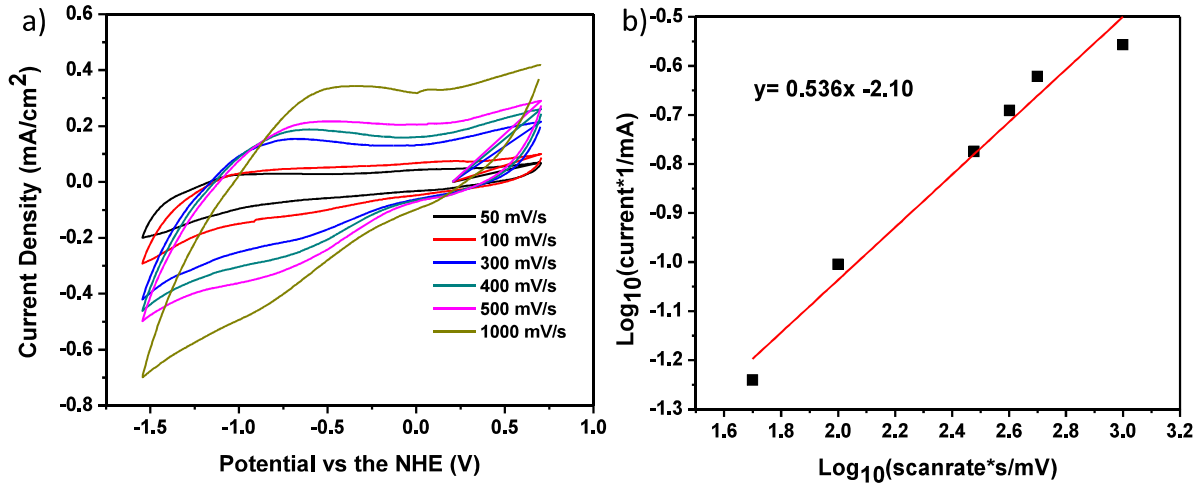

Figure 3-14. a) CV curves of Hf_{12}-CoDBP/CNT in ACN at varying scan rates. b) A linear relationship between $\log_{10}$(current in mA) and $\log_{10}$(scan rate in mV/s) with a slope of 0.54 suggests electron transfer occurs via charge hopping to the cobalt center.

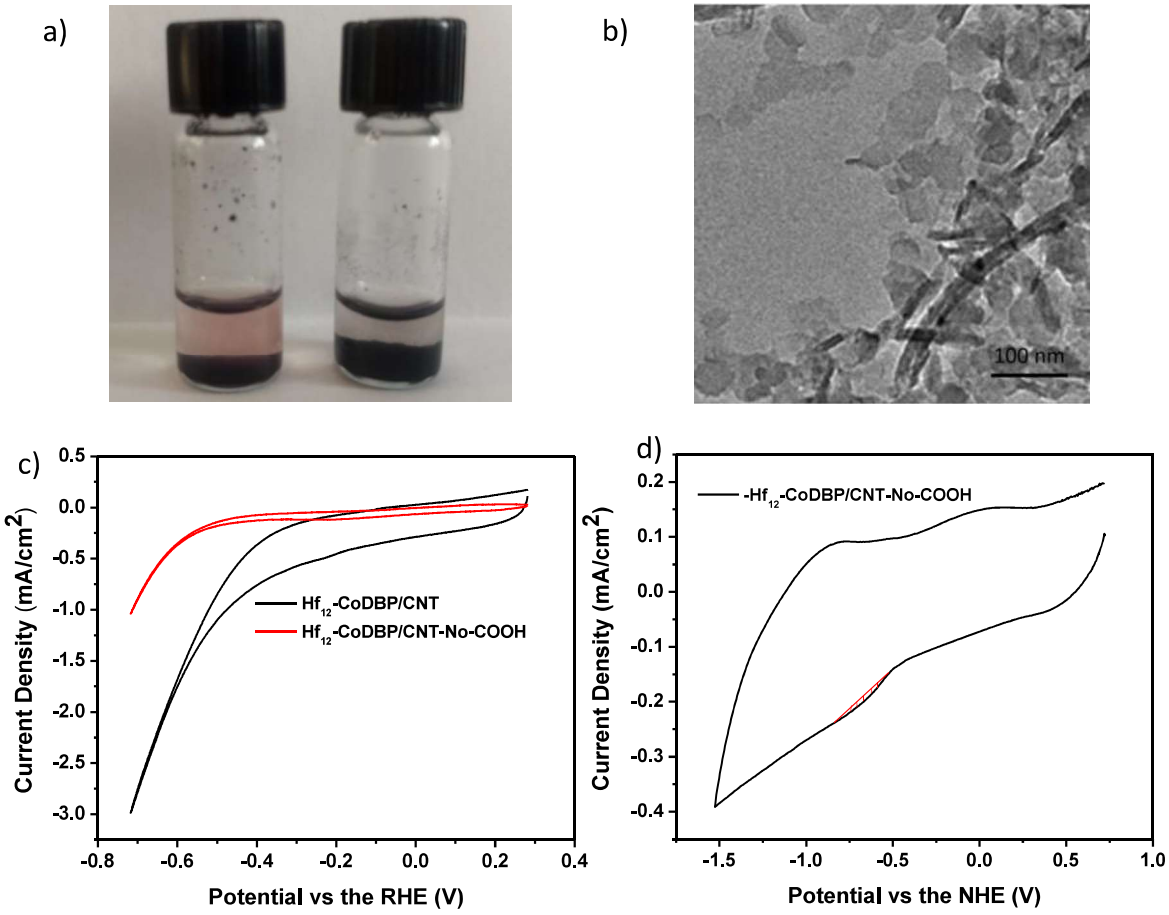

Figure 3-15. a) Hf_{12}-CoDBP/non-carboxylated CNT (left) showed the color of unbound Hf_{12}-CoDBP in the supernatant but not Hf_{12}-CoDBP/CNT (right). b) TEM image of Hf_{12}-CoDBP/non-carboxylated CNT. c) CV curve of Hf_{12}-CoDBP/CNT and Hf_{12}-CoDBP/non-carboxylated CNT at pH = 1 ($HClO_4$). d) CV curve of Hf_{12}-CoDBP/non-carboxylated CNT in 0.1 M $TBAPF_6$ dissolved in ACN shows that 0.29% of 1.81 nmol total Co on the electrode is electrochemically active.

Table 3-1. The results of 30 minutes of controlled potential electrolysis at η = 715 mV for various samples of Hf_{12}-CoDBP/CNT/Nafion with variable CNT loading in pH 1 perchloric acid.

Sample	η (mV)	μMOL H_2 Produced	TON	%Faradaic Efficiency
Hf_{12}-CoDBP/1mg-CNT	715	3.81	8.20×10^2	64.8
Hf_{12}-CoDBP/2mg-CNT	715	4.44	1.51×10^3	65.7
Hf_{12}-CoDBP/3mg-CNT	715	4.66	2.82×10^3	70.3
Hf_{12}-CoDBP/4mg-CNT	715	6.29	1.06×10^4	85.3
Hf_{12}-CoDBP/5mg-CNT	715	5.94	3.80×10^3	80.0

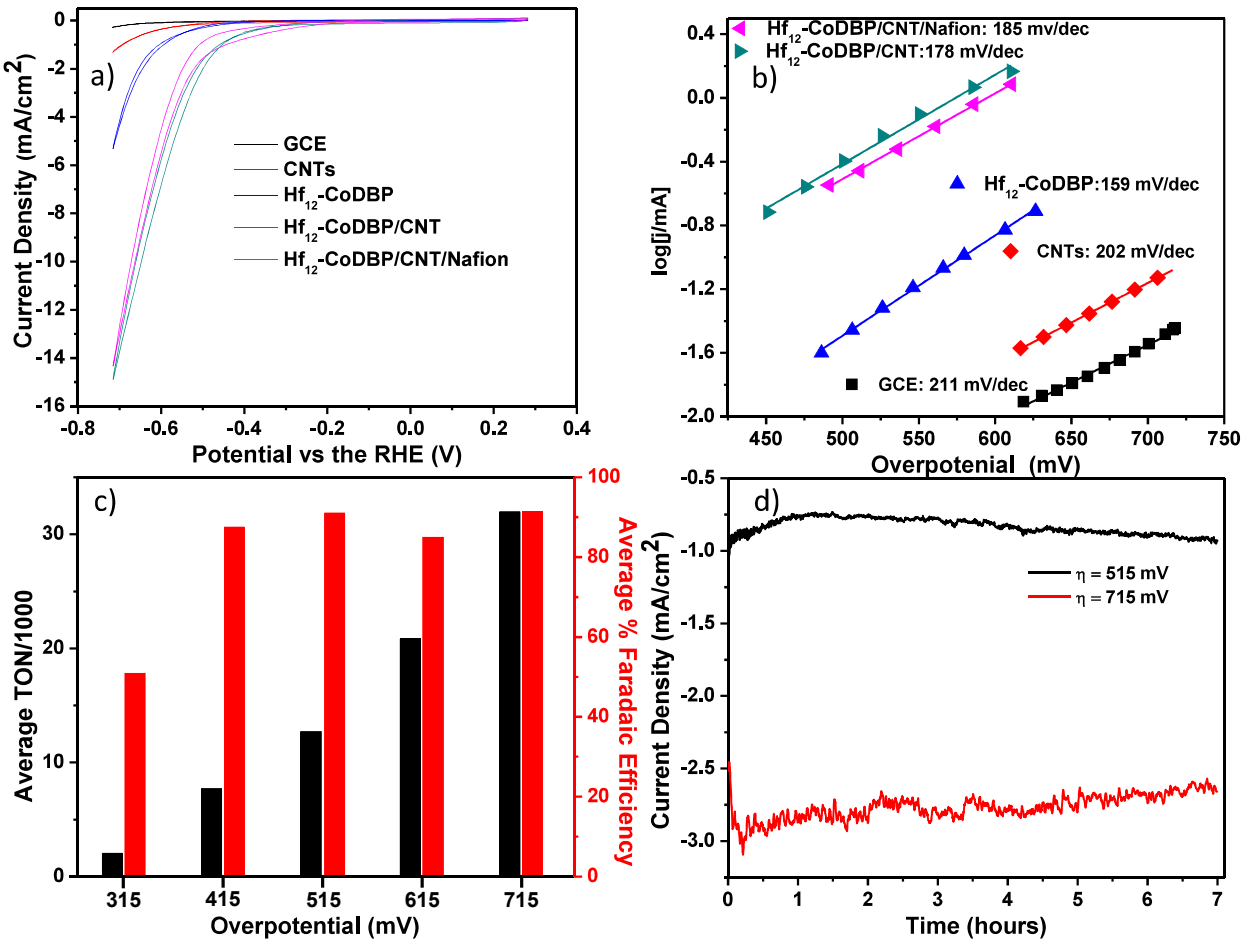

Figure 3-16. a) The CV curves of Hf_{12}-CoDBP/CNT and Hf_{12}-CoDBP/CNT/Nafion compared to their controls in 0.1 M aqueous perchloric acid and b) their corresponding Tafel curves. c) TON (black) and Faradaic Efficiency (red) measurements of Hf_{12}-CoDBP/CNT/Nafion after 30 minutes of controlled potential electrolysis at varying overpotenials at pH = 1. d) Time-dependent current densities of bulk electrolysis by Hf_{12}-CoDBP/CNT/Nafion at η = 515 and 715 mV, showing sustained hydrogen production for >7 hours.

Hf_{12}-CoDBP/CNT greatly outperformed Hf_{12}-CoDBP and Hf_{12}-CoDBP/non-carboxylated CNT in electrocatalytic HER in aqueous media (Table 3-1). Dropcasted Hf_{12}-CoDBP/CNT exhibited a remarkable electrocatalytic HER activity in a pH = 1 perchloric acid solution, with a current density of $10mA/cm^2$ at an overpotential (η) of 650 mV. This corresponds to a Tafel slope of 178 mV/dec, which is consistent with a rate limiting step involving the adsorption of a proton to the catalytic site within the Volmer portion of the HER (Figure 3-16 a,b) and competitive with other precious-metal-free HER catalysts (Table 3-2). The importance of the CNT tethering was further supported by the increased current densities for Hf_{12}-CoDBP/CNT samples with higher CNT loadings relative to Hf_{12}-CoDBP (Figure 3-17). However, long term stability of the Hf_{12}-CoDBP/CNT system remained an issue as stirring and hydrogen bubble formation tended to shear the catalyst off the electrode surface.

Table 3-2. The efficiency of porphyrin and cobalt-containing electrocatalysts for HER.

Sample	Solvent	Ref. Electrode	H^+ Source	Potential (V)	TON	% F.E
FeTPP[42]	DMF	SCE	TEA-H^+	-1.60	22	> 95
CoPc[43]	H_3PO_4, pH 1	AgCl	H^+	-0.9	20000	N/A
CoTMAP[44]	H_2O	SCE	0.1 M TFA	-0.95	N/A	> 90
CoTPPS[38]	2M Kpi (*aq*)	SHE	H_2O, pH 7	-1.29	725	> 95
CoP[45]	PO_4^{3-}, pH 7	SCE	Benzoic acid	-1.30	n/a	n/a
Co($dmgBF_2$)$_2$[46]	ACN	SCE	HCl	-0.37 V	11	90
Cobalt Tetraazamacrocycle[47]	$NaClO_4$ (*aq*)	SCE	H^+, pH 2.2	-0.93	22	81
CoPY5Me$_2$[8]	PO_4^{3-}, pH 7	SHE	H_2O	-1.30	55000	100
CoPY4[48]	H_2O/ACN	SCE	TFA	N/A	40	N/A
Co(mnt)$^-_2$[49]	H_2O/ACN	SCE	Ascorbic acid, pH 4	-1.37	3450	N/A
CoMP11-AC[50]	H_2O	Ag/AgCl	H_2O	-1.5	25000	> 95

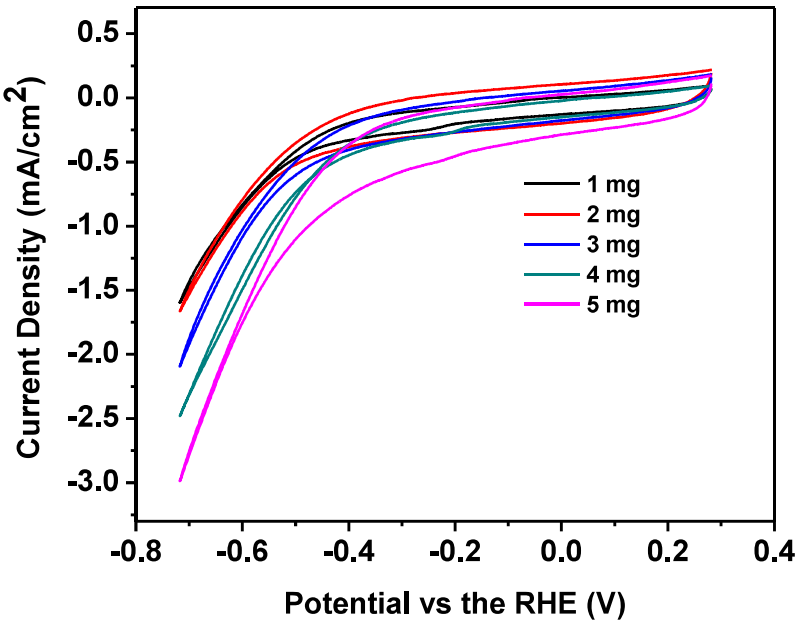

Figure 3-17. CV traces of 0.05 mg of Hf_{12}-CoDBP/CNT/Nafion synthesized with 1 to 5 mg of CNTs and 1.7 mg of CoDBP in pH 1 perchloric acid solutions. Increasing currents due to increasing amounts of CNT indicate the important role of carboxylated CNT in electrocatalytic activity.

Nafion was therefore added to the Hf_{12}-CoDBP/CNT suspension to improve thin film stability while serving as a proton conducting layer. The Hf_{12}-CoDBP/CNT/Nafion sample maintained stable currents for varying time lengths of electrolysis at a η of 715 mV, producing hydrogen with a TON of 3.2×10^4 after thirty minutes of electrolysis and a TOF= 17.7 s^{-1} based on active Co sites (Figure 3-16c). Furthermore, hydrogen gas was detected at a η as low as 315 mV at pH = 1 and Hf_{12}-CoDBP/CNT/Nafion showed moderate activity in aqueous solutions up to pH = 5 (Figure 3-18). In comparison, the bare glassy carbon electrode, bare CNTs, and Hf_{12}-H_2DBP/CNT need an overpotenial of ≥515 mV to detect any trace of hydrogen, most likely from nanoparticle formation

[51, 52] at a rate that is at least one order of magnitude lower than that of Hf_{12}-CoDBP/CNT/Nafion (Table 3-3, Figure 3-19).

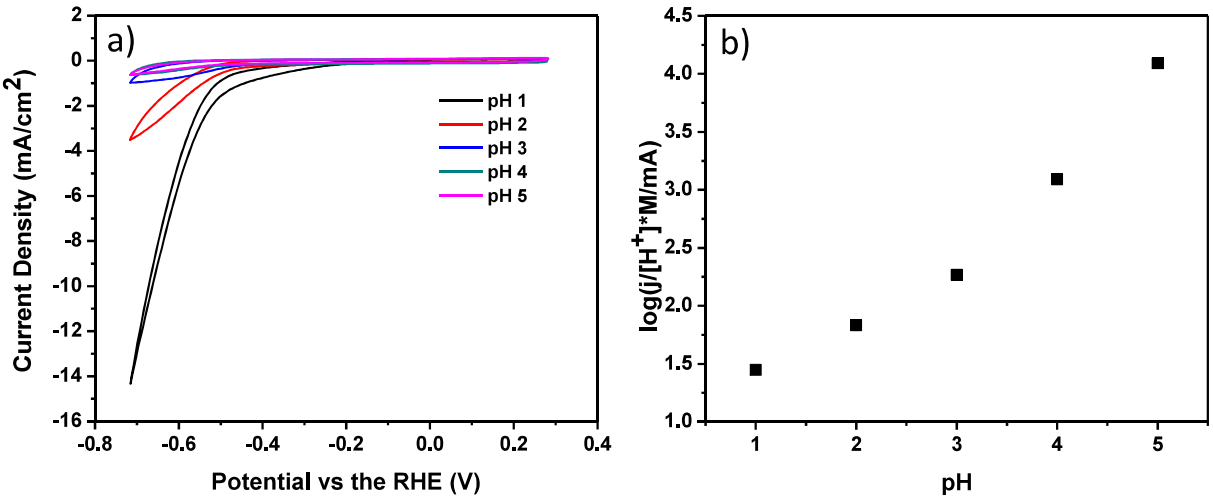

Figure 3-18. a) CV traces of Hf_{12}-CoDBP/CNT at varying pHs and b) the recorded current at η = 715 mV divided by proton concentration shows enhanced activity at higher pH values, indicating non-first order kinetics.

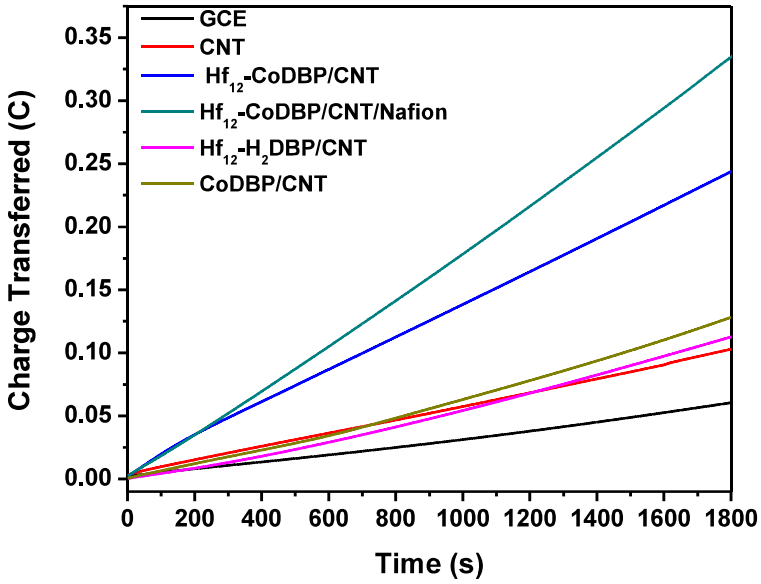

Figure 3-19. Controlled potential electrolysis of Hf_{12}-CoDBP/CNT and Hf_{12}-CoDBP/CNT/Nafion outperform their controls at a η of 515 mV vs the RHE at pH = 1 (perchloric acid).

Table 3-3. The results of controlled potential electrolysis at varying potentials show the functionalized Hf_{12}-CoDBP materials outperform the controls in both activity and Faradaic efficiency.

Sample	η (mV)	μMOL H_2 Produced	%Faradaic Efficiency
GCE	515	0.084	38.7
CNT	515	0.0593	14.1
CoDBP/Nafion	515	0.421	81.7
Hf_{12}-CoDBP/CNT	515	0.878	71.1
Hf_{12}-CoDBP/CNT/Nafion	515	1.41	82.9
Hf_{12}-H_2DBP/CNT	515	0.154	3.0
GCE	715	1.13	45.8
CNT	715	1.88	12.9
CoDBP/Nafion	715	1.59	43.1
Hf_{12}-CoDBP/CNT	715	10.33	93.2
Hf_{12}-CoDBP/CNT/Nafion	715	16.39	83.5
Hf_{12}-H_2DBP/CNT	715	3.39	36.8

Hf_{12}-CoDBP/CNT/Nafion showed good efficacy of electrocatalytic HER at varying potentials (Figure 3-10c). At $\eta > 415$ mV, the Faradaic efficiency averaged at 92.4%. The Faradaic efficiency was only 51.2% at $\eta = 315$ mV, likely due to dominance of CNT reduction and other side reactions over HER at low overpotentials. Above $\eta > 415$, the TON showed a roughly linear increase with overpotential; a slight tailing off was observed at higher potentials indicative of saturation of active sites with protons. Hf_{12}-CoDBP/CNT/Nafion also showed very good stability with consistent hydrogen production across varying potentials for at least seven hours (Figure 3-16d).

In addition to enhancing stability, Nafion can also slow down the transport of larger ions (such as Co^{2+}) to the electrode surface to mitigate the formation of nanoparticles, which can also catalyze proton reduction, thus ensuring that HER by Hf_{12}-CoDBP/CNT is entirely molecular in nature. In agreement with this conjecture, the Hf_{12}-CoDBP/CNT/Nafion showed good stability upon 10 000 CV cycles and no significant change in the CV curve before and after electrocatalytic HER (Figure 3-20). In addition, ICP-MS analyses showed negligible leaching of Co (<0.2%) and Hf (<0.1 %) from Hf_{12}-CoDBP/CNT/Nafion after electrolysis at η=715 mV for one hour based on metal loadings on the electrode surface. PXRD and UV-Vis spectra of Hf_{12}-CoDBP/CNT/Nafion remained unchanged after electrolysis at η =715 mV for 18 hours (Figure 3-20c). Additionally, TEM imaging showed no Co or Pt nanoparticle formation during electrolysis (Figure 3-20d). The system was still active with a GCE counter electrode in place of the Pt electrode for all other studies (Figure 3-21).

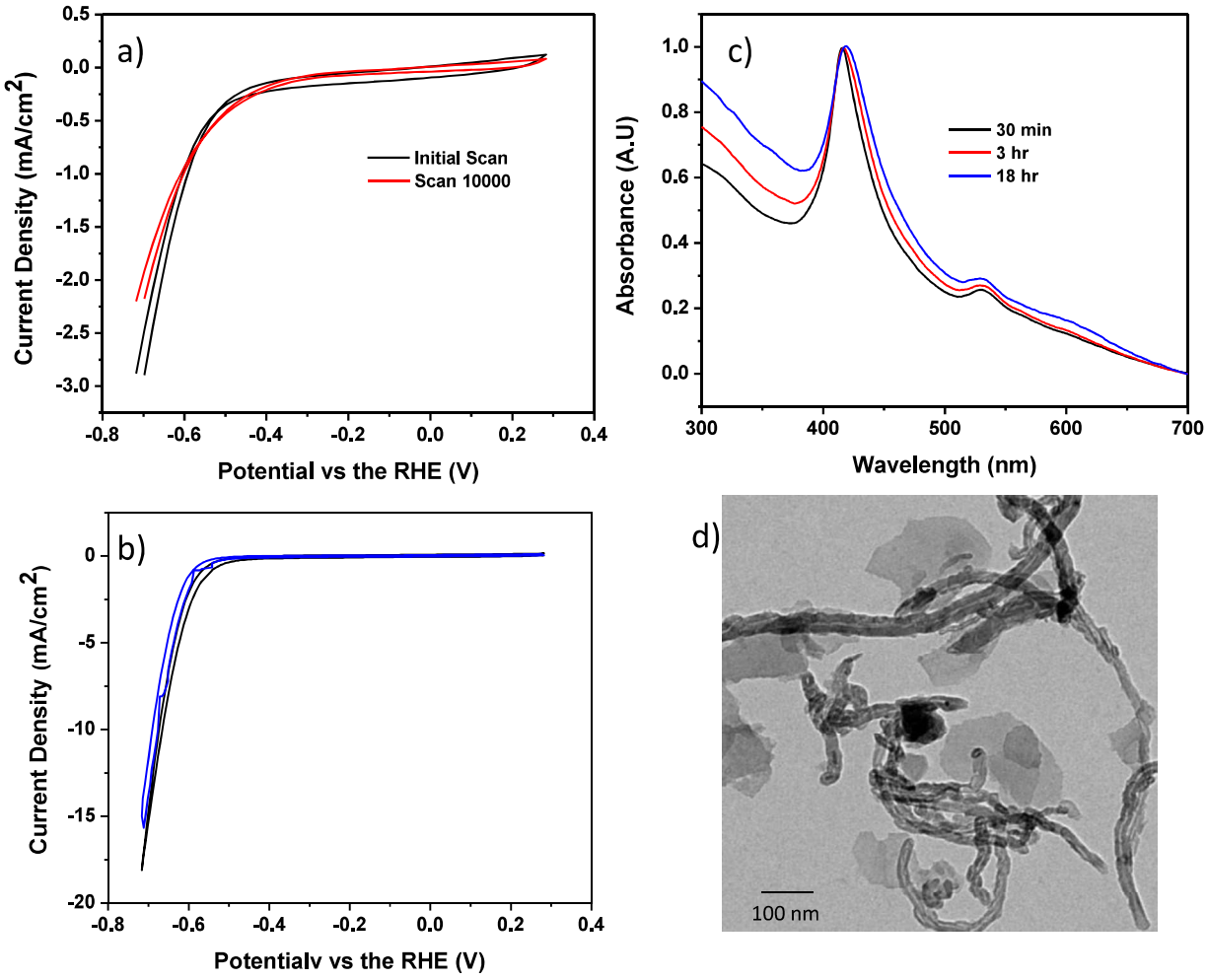

Figure 3-20. a) Hf_{12}-CoDBP/CNT/Nafion shows consistent CV curves after 10,000 CV scans and b) after 30 minutes of controlled potential electrolysis at 715 mV vs the RHE in pH = 1 $HClO_4$. c) Hf_{12}-CoDBP/CNT/Nafion shows no change in its UV-Visible spectra after bulk electrolysis at η = 615 mV for various time lengths, d) Hf_{12}-CoDBP/CNT/Nafion shows no Co nanoparticle formation in the TEM after electrolysis at an overpotential of 715 mV for one hour.

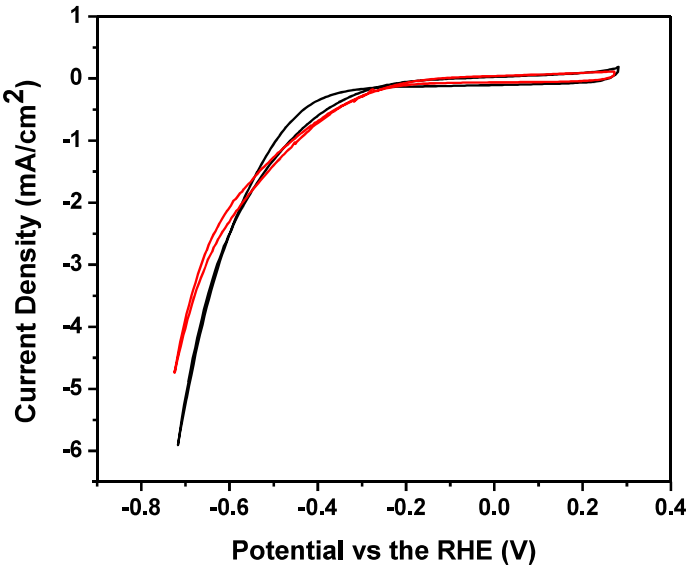

Figure 3-21. CV traces of Hf_{12}-CoDBP/CNT/Nafion taken with a GCE counter electrode before (red) and after bulk electrolysis (black) in pH 1 perchloric acid.

3.3 Conclusion

We have synthesized Co-porphyrin MOFs supported on CNT for efficient electrocatalytic proton reduction. Covalent attachment of Co-porphyrin MOFs to CNTs significantly increases the number of catalytically active sites by increasing both the surface areas of conductive supports and the percentage of active sites in contact to a conductive surface. The MOF/CNT hybrid is highly active for the reduction of protons to hydrogen in acidic media with an onset potential of 315 mV and TOFs of over 17.7 s^{-1}. This straightforward synthetic strategy should be amenable to the design of other MOF/CNT heterostructures for electrochemical applications as conductive CNTs compensate for the insulating nature of MOFs.

3.4 Experimental Methodologies

3.4.1 Electrochemical Methods: All electrochemical experiments were performed using a Pine Instruments WaveDriver potentiostat (Model AFP2). Non-catalytic experimental techniques were performed in acetonitrile degassed with nitrogen for at least thirty minutes with a 0.1 M

$TBAPF_6$ serving as the electrolyte. Aqueous based experiments were performed in pH 1 perchloric acid solution degassed with nitrogen for at least thirty minutes. If the pH was increased, the electrolyte concentration was maintained at 0.1 $[ClO_4]^-$ using potassium perchlorate. Cyclic voltammetry (CV) measurements were performed in a standard three-electrode cell with a glassy carbon electrode (0.4 cm diameter) serving as the working electrode, silver chloride electrode serving as the reference electrode (Calculated at 0.223 V vs NHE from the $Fe(CN)_6$ redox couple), and a platinum counter electrode. Scan rates were collected at 100 mV s^{-1} unless stated otherwise and all experiments were collected underneath a nitrogen atmosphere. Controlled potential electrolysis was performed in the same setup as the CV except that the electrode was spun at 400 RPM using the RDE assembly coupled with a stir bar at 400 RPM to prevent bubbles from obscuring the working electrode surface.

3.4.2 GC Quantification: All gas chromatography (GC) measurements were obtained using an Agilent 7890B GC system. 300 μL of headspace (measured to be 177 mL) of the reaction vessel was injected post controlled potential electrolysis.

3.4.3 XPS Characterization: X-ray photoelectron spectroscopy (XPS) data was collected using an AXIS Nova spectrometer (Kratos Analytical) with monochromatic Al Kα Xray source. For this instrument, the Al anode was powered at 10 mA and 15kV. Instrument base pressure was ca. 1×10^{-9} Torr, and the analysis area size was 0.3×0.7 mm^2. For calibration purposes, the binding energies were referenced to the C 1s peak at 284.8 eV. Survey spectra were collected with a step size of 1 eV and a pass energy of 160 eV, while the cobalt region was collected with a step size of 0.1 eV.

3.4.4 ICP-MS Characterization: ICP-MS data was obtained with an Agilent 7700x ICP-MS and analyzed using ICP-MS MassHunter version B01.03. Samples were diluted in a 2% HNO_3

matrix and analyzed with a ^{159}Tb internal standard against a 12-point standard curve over the range from 0.1 ppb to 500 ppb. The correlation was >0.9997 for all analyses of interest. Data collection was performed in spectrum Mode with five replicates per sample and 100 sweeps per replicate.

3.5 Synthesis of Materials

3.5.1 Synthesis of Ligands

The synthesis of the porphyrin H_2DBP ligand can be found in chapter 2.

3.5.2 Synthesis of MOFs

Synthesis Hf_{12}-CoDBP: H_2DBP (1.5 mg, 2.7 μmol), hafnium(IV) chloride (1.00 mg, 3.15 μmol), and acetic acid (70 μL, 1224 umol) were combined in 1.0 mL of dimethylformamide and heated at 85 °C oven for three days. A dark red powder was collected by centrifugation and washed with DMF three times. The MOF was then metalated with 4.05 μmol of $CoCl_2 \cdot 6H_2O$ in 1 mL of DMF at 80 °C for 24 hours. The product was washed with DMF then ethanol twice and collected via centrifugation and stored in 0.5 mL of ethanol. Yield: 1.5 mg (71.5%).

Alternatively, Hf_{12}-CoDBP was prepared by heating a mixture of H_2CoDBP (1.66 mg, 2.7 μmol), hafnium(IV) chloride (1.00 mg, 3.15 μmol), water (10 μL μmol), and acetic acid (70 μL, 1224 umol) in DMF at 85 °C for three days. Yield: 1.0 mg (47.7%).

Synthesis of Hf_{12}-CoDBP/CNT: H_2CoDBP (1.66 mg, 2.7 μmol), hafnium(IV) chloride (1.00 mg, 3.15 μmol), 5 mg of carboxylated multi-walled carbon nanotubes, 10 μL H_2O, and acetic acid (70 μL, 1224 umol) were combined in 1.0 mL of dimethylformamide and heated at 85 °C for three days. A black powder was collected by centrifugation and washed with DMF three times, ethanol twice, then stored in 0.5 mL of ethanol.

3.6 References

1. Armor, J. N., Catalysis and the hydrogen economy. *Catal. Lett.* **2005,** *101* (3-4), 131-135.

2. Trasatti, S., Work function, electronegativity, and electrochemical behavior of metals. III. Electrolytic
hydrogen evolution in acid solutions. *J. Electroanal. Chem. Interfacial Electrochem.* **1972,** *39* (1), 163-84.

3. Norskov, J. K.; Bligaard, T.; Logadottir, A.; Kitchin, J. R.; Chen, J. G.; Pandelov, S.; Stimming, U., Trends in the exchange current for hydrogen evolution. *J. Electrochem. Soc.* **2005,** *152* (3), J23-J26.

4. Hu, X. L.; Brunschwig, B. S.; Peters, J. C., Electrocatalytic Hydrogen Evolution at Low Overpotentials by Cobalt Macrocyclic Glyoxime and Tetraimine Complexes. *J. Am. Chem. Soc.* **2007,** *129* (29), 8988-8998.

5. Jacques, P.-A.; Artero, V.; Pecaut, J.; Fontecave, M., Cobalt and nickel diimine-dioxime complexes as molecular electrocatalysts for hydrogen evolution with low overvoltages. *Proc. Natl. Acad. Sci. U. S. A.* **2009,** *106* (49), 20627-20632.

6. Connolly, P.; Espenson, J. H., Cobalt-catalyzed evolution of molecular hydrogen. *Inorg. Chem.* **1986,** *25* (16), 2684-8.

7. Dempsey, J. L. Hydrogen evolution catalyzed by cobaloximes. 2011.

8. Sun, Y.; Bigi, J. P.; Piro, N. A.; Tang, M. L.; Long, J. R.; Chang, C. J., Molecular Cobalt Pentapyridine Catalysts for Generating Hydrogen from Water. *J. Am. Chem. Soc.* **2011,** *133* (24), 9212-9215.

9. Tsay, C.; Yang Jenny, Y., Electrocatalytic Hydrogen Evolution under Acidic Aqueous Conditions and Mechanistic Studies of a Highly Stable Molecular Catalyst. *J Am Chem Soc* **2016,** *138* (43), 14174-14177.

10. Bianchini, C.; Fornasiero, P., A Synthetic Nickel Electrocatalyst with a Turnover Frequency above 100 000 s-1 for H2 Production. *ChemCatChem* **2012,** *4* (1), 45-46.

11. Wilson Aaron, D.; Shoemaker, R. K.; Miedaner, A.; Muckerman, J. T.; DuBois Daniel, L.; DuBois, M. R., Nature of hydrogen interactions with Ni(II) complexes containing cyclic phosphine ligands with pendant nitrogen bases. *Proc Natl Acad Sci U S A* **2007,** *104* (17), 6951-6.

12. Kaur-Ghumaan, S.; Schwartz, L.; Lomoth, R.; Stein, M.; Ott, S., Catalytic Hydrogen Evolution from Mononuclear Iron(II) Carbonyl Complexes as Minimal Functional Models of the [FeFe] Hydrogenase Active Site. *Angew. Chem., Int. Ed.* **2010,** *49* (43), 8033-8036, S8033/1-S8033/12.

13. Gloaguen, F.; Rauchfuss, T. B., Small molecule mimics of hydrogenases: hydrides and redox. *Chem. Soc. Rev.* **2009,** *38* (1), 100-108.

14. Benck, J. D.; Hellstern, T. R.; Kibsgaard, J.; Chakthranont, P.; Jaramillo, T. F., Catalyzing the Hydrogen Evolution Reaction (HER) with Molybdenum Sulfide Nanomaterials. *ACS Catal.* **2014,** *4* (11), 3957-3971.

15. Vrubel, H.; Hu, X., Molybdenum Boride and Carbide Catalyze Hydrogen Evolution in both Acidic and Basic Solutions. *Angew. Chem., Int. Ed.* **2012,** *51* (51), 12703-12706.

16. Xing, Z.; Liu, Q.; Asiri, A. M.; Sun, X., Closely interconnected network of molybdenum phosphide nanoparticles: a highly efficient electrocatalyst for generating hydrogen from water. *Adv. Mater. (Weinheim, Ger.)* **2014,** *26* (32), 5702-5707.

17. Jin, H.; Guo, C.; Liu, X.; Liu, J.; Vasileff, A.; Jiao, Y.; Zheng, Y.; Qiao, S.-Z., Emerging Two-Dimensional Nanomaterials for Electrocatalysis. *Chem. Rev. (Washington, DC, U. S.)* **2018**, Ahead of Print.

18. Horiuchi, Y.; Toyao, T.; Saito, M.; Mochizuki, K.; Iwata, M.; Higashimura, H.; Anpo, M.; Matsuoka, M., Visible-Light-Promoted Photocatalytic Hydrogen Production by Using an Amino-Functionalized Ti(IV) Metal-Organic Framework. *J. Phys. Chem. C* **2012,** *116* (39), 20848-20853.

19. Fateeva, A.; Chater, P. A.; Ireland, C. P.; Tahir, A. A.; Khimyak, Y. Z.; Wiper, P. V.; Darwent, J. R.; Rosseinsky, M. J., A Water-Stable Porphyrin-Based Metal-Organic Framework Active for Visible-Light Photocatalysis. *Angew. Chem., Int. Ed.* **2012,** *51* (30), 7440-7444, S7440/1-S7440/17.

20. Wu, P.; Jiang, M.; Li, Y.; Liu, Y.; Wang, J., Highly efficient photocatalytic hydrogen production from pure water via a photoactive metal-organic framework and its PDMS@MOF. *J. Mater. Chem. A* **2017,** *5* (17), 7833-7838.

21. Lan, G.; Zhu, Y.-Y.; Veroneau, S. S.; Xu, Z.; Micheroni, D.; Lin, W., Electron Injection from Photoexcited Metal-Organic Framework Ligands to Ru2 Secondary Building Units for Visible-Light-Driven Hydrogen Evolution. *J. Am. Chem. Soc.* **2018,** *140* (16), 5326-5329.

22. deKrafft, K. E.; Wang, C.; Lin, W., Metal-Organic Framework Templated Synthesis of Fe2O3/TiO2 Nanocomposite for Hydrogen Production. *Adv. Mater. (Weinheim, Ger.)* **2012,** *24* (15), 2014-2018.

23. Zhang, J.; An, B.; Hong, Y.; Meng, Y.; Hu, X.; Wang, C.; Lin, J.; Lin, W.; Wang, Y., Pyrolysis of metal-organic frameworks to hierarchical porous Cu/Zn-nanoparticle@carbon materials for efficient CO2 hydrogenation. *Mater. Chem. Front.* **2017,** *1* (11), 2405-2409.

24. Xia, B. Y.; Yan, Y.; Li, N.; Wu, H. B.; Lou, X. W.; Wang, X., A metal-organic framework-derived bifunctional oxygen electrocatalyst. *Nat. Energy* **2016,** *1* (1), 15006.

25. Zhao, S.; Wang, Y.; Dong, J.; He, C.-T.; Yin, H.; An, P.; Zhao, K.; Zhang, X.; Gao, C.; Zhang, L.; Lv, J.; Wang, J.; Zhang, J.; Khattak, A. M.; Ali Khan, N.; Wei, Z.; Zhang, J.; Liu, S.; Zhao, H.; Tang, Z., Ultrathin metal-organic framework nanosheets for electrocatalytic oxygen evolution. *Nat. Energy* **2016,** *1* (12), 16184.

26. Kornienko, N.; Zhao, Y.; Kley, C. S.; Zhu, C.; Kim, D.; Lin, S.; Chang, C. J.; Yaghi, O. M.; Yang, P., Metal-Organic Frameworks for Electrocatalytic Reduction of Carbon Dioxide. *J. Am. Chem. Soc.* **2015,** *137* (44), 14129-14135.

27. Lu, X.-F.; Liao, P.-Q.; Wang, J.-W.; Wu, J.-X.; Chen, X.-W.; He, C.-T.; Zhang, J.-P.; Li, G.-R.; Chen, X.-M., An Alkaline-Stable, Metal Hydroxide Mimicking Metal-Organic Framework for Efficient Electrocatalytic Oxygen Evolution. *J. Am. Chem. Soc.* **2016,** *138* (27), 8336-8339.

28. Wurster, B.; Grumelli, D.; Hoetger, D.; Gutzler, R.; Kern, K., Driving the Oxygen Evolution Reaction by Nonlinear Cooperativity in Bimetallic Coordination Catalysts. *J. Am. Chem. Soc.* **2016,** *138* (11), 3623-3626.

29. Miner, E. M.; Gul, S.; Ricke, N. D.; Pastor, E.; Yano, J.; Yachandra, V. K.; Van Voorhis, T.; Dinca, M., Mechanistic Evidence for Ligand-Centered Electrocatalytic Oxygen Reduction with the Conductive MOF Ni3(hexaiminotriphenylene)2. *ACS Catal.* **2017,** *7* (11), 7726-7731.

30. Hod, I.; Deria, P.; Bury, W.; Mondloch, J. E.; Kung, C.-W.; So, M.; Sampson, M. D.; Peters, A. W.; Kubiak, C. P.; Farha, O. K.; Hupp, J. T., A porous proton-relaying metal-organic framework material that accelerates electrochemical hydrogen evolution. *Nat. Commun.* **2015,** *6*, 8304.

31. Hod, I.; Sampson, M. D.; Deria, P.; Kubiak, C. P.; Farha, O. K.; Hupp, J. T., Fe-Porphyrin-Based Metal-Organic Framework Films as High-Surface Concentration, Heterogeneous Catalysts for Electrochemical Reduction of CO2. *ACS Catal.* **2015,** *5* (11), 6302-6309.

32. Usov, P. M.; Huffman, B.; Epley, C. C.; Kessinger, M. C.; Zhu, J.; Maza, W. A.; Morris, A. J., Study of Electrocatalytic Properties of Metal-Organic Framework PCN-223 for the Oxygen Reduction Reaction. *ACS Appl. Mater. Interfaces* **2017,** *9* (39), 33539-33543.

33. Miner, E. M.; Wang, L.; Dinca, M., Modular O2 electroreduction activity in triphenylene-based metal-organic frameworks. *Chem. Sci.* **2018,** *9* (29), 6286-6291.

34. Lin, S.; Pineda-Galvan, Y.; Maza, W. A.; Epley, C. C.; Zhu, J.; Kessinger, M. C.; Pushkar, Y.; Morris, A. J., Electrochemical Water Oxidation by a Catalyst-Modified Metal-Organic Framework Thin Film. *ChemSusChem* **2017,** *10* (3), 469.

35. Ji, P.; Manna, K.; Lin, Z.; Feng, X.; Urban, A.; Song, Y.; Lin, W., Single-Site Cobalt Catalysts at New Zr12(μ3-O)8(μ3-OH)8(μ2-OH)6 Metal-Organic Framework Nodes for Highly Active Hydrogenation of Nitroarenes, Nitriles, and Isocyanides. *J. Am. Chem. Soc.* **2017,** *139* (20), 7004-7011.

36. Ni, K.; Lan, G.; Chan, C.; Quigley, B.; Lu, K.; Aung, T.; Guo, N.; La Riviere, P.; Weichselbaum, R. R.; Lin, W., Nanoscale metal-organic frameworks enhance radiotherapy to potentiate checkpoint blockade immunotherapy. *Nat. Commun.* **2018,** *9* (1), 1-12.

37. Lu, K.; He, C.; Guo, N.; Chan, C.; Ni, K.; Lan, G.; Tang, H.; Pelizzari, C.; Fu, Y.-X.; Spiotto, M. T.; Weichselbaum, R. R.; Lin, W., Low-dose X-ray radiotherapy–radiodynamic therapy via nanoscale metal–organic frameworks enhances checkpoint blockade immunotherapy. *Nature Biomedical Engineering* **2018**.

38. Beyene, B. B.; Mane, S. B.; Hung, C.-H., Highly efficient electrocatalytic hydrogen evolution from neutral aqueous solution by a water-soluble anionic cobalt(II) porphyrin. *Chem. Commun. (Cambridge, U. K.)* **2015,** *51* (81), 15067-15070.

39. Kellett, R. M.; Spiro, T. G., Cobalt porphyrin electrode films as hydrogen catalysts. *Inorg. Chem.* **1985,** *24* (15), 2378-82.

40. Hu, B.; Sun, C.; Deng, Q.; Liu, Z., Synthesis and catalytic properties of a series of cobalt porphyrins as cytochrome P450 model: the effect of substituents on the catalytic activity. *J. Inclusion Phenom. Macrocyclic Chem.* **2013,** *76* (3-4), 345-352.

41. Walker, F. A.; Beroiz, D.; Kadish, K. M., Electronic effects in transition metal porphyrins. 2. The sensitivity of redox and ligand addition reactions in para-substituted tetraphenylporphyrin complexes of cobalt(II). *J. Am. Chem. Soc.* **1976,** *98* (12), 3484-9.

42. Bhugun, I.; Lexa, D.; Saveant, J.-M., Homogeneous Catalysis of Electrochemical Hydrogen Evolution by Iron(0) Porphyrins. *J. Am. Chem. Soc.* **1996,** *118* (16), 3982-3.

43. Zhao, F.; Zhang, J.; Abe, T.; Wohrle, D.; Kaneko, M., Electrocatalytic proton reduction by phthalocyanine cobalt derivatives incorporated in poly(4-vinylpyridine-co-styrene) film. *J. Mol. Catal. A Chem.* **1999,** *145* (1-2), 245-256.

44. Kellett, R. M.; Spiro, T. G., Cobalt(I) porphyrin catalysts of hydrogen production from water. *Inorg. Chem.* **1985,** *24* (15), 2373-7.

45. Natali, M.; Luisa, A.; Iengo, E.; Scandola, F., Efficient photocatalytic hydrogen generation from water by a cationic cobalt(ii) porphyrin. *Chem. Commun. (Cambridge, U. K.)* **2014,** *50* (15), 1842-1844.

46. Hu, X.; Cossairt, B. M.; Brunschwig, B. S.; Lewis, N. S.; Peters, J. C., Electrocatalytic hydrogen evolution by cobalt difluoroboryl-diglyoximate complexes. *Chem. Commun. (Cambridge, U. K.)* **2005,** (37), 4723-4725.

47. McCrory, C. C. L.; Uyeda, C.; Peters, J. C., Electrocatalytic Hydrogen Evolution in Acidic Water with Molecular Cobalt Tetraazamacrocycles. *J. Am. Chem. Soc.* **2012,** *134* (6), 3164-3170.

48. Bigi, J. P.; Hanna, T. E.; Harman, W. H.; Chang, A.; Chang, C. J., Electrocatalytic reduction of protons to hydrogen by a water-compatible cobalt polypyridyl platform. *Chem. Commun. (Cambridge, U. K.)* **2010,** *46* (6), 958-960.

49. McNamara, W. R.; Han, Z.; Yin, C.-J.; Brennessel, W. W.; Holland, P. L.; Eisenberg, R., Cobalt-dithiolene complexes for the photocatalytic and electrocatalytic reduction of protons in aqueous solutions. *Proc. Natl. Acad. Sci. U. S. A.* **2012,** *109* (39), 15594-15599, S15594/1-S15594/8.

50. Kleingardner, J. G.; Kandemir, B.; Bren, K. L., Hydrogen Evolution from Neutral Water under Aerobic Conditions Catalyzed by Cobalt Microperoxidase-11. *J. Am. Chem. Soc.* **2014,** *136* (1), 4-7.

51. Zhou, W.; Zhou, J.; Zhou, Y.; Lu, J.; Zhou, K.; Yang, L.; Tang, Z.; Li, L.; Chen, S., N-Doped Carbon-Wrapped Cobalt Nanoparticles on N-Doped Graphene Nanosheets for High-Efficiency Hydrogen Production. *Chem. Mater.* **2015,** *27* (6), 2026-2032.

52. Zou, X.; Huang, X.; Goswami, A.; Silva, R.; Sathe, B. R.; Mikmekova, E.; Asefa, T., Cobalt-Embedded Nitrogen-Rich Carbon Nanotubes Efficiently Catalyze Hydrogen Evolution Reaction at All pH Values. *Angew. Chem., Int. Ed.* **2014,** *53* (17), 4372-4376.

CHAPTER 4

Luminescence Enhancement of *cis*-$[Ru(bpy)_2(py)_2]^{2+}$ via Confinement within a Metal-Organic Framework

4.1 Introduction

The need for good photosensitizers is paramount. Metal-polypyridyl compounds, in particular those of Ru and Ir, are among the most studied molecular photosensitizers because they absorb strongly in the visible spectrum and undergo both oxidative and reductive chemistry from their long-lived triplet metal-to-ligand charge transfer (^{3}MLCT) excited states.[1] As a result of their unique photophysical and photochemical properties, metal-polypyridyl compounds have been studied in numerous photochemical applications ranging from catalysis,[2, 3] photo-electrochemistry,[4] dye-sensitized solar cells, [5, 6] artificial photosynthesis,[7] and other applications.[8, 9] The tremendous utility of the metal-polypyridyl compounds, derived from their physical properties, has sparked numerous studies into the fundamental properties of their respective photoexcited states. However, specific photosensitizers can be difficult to study, often as a result of photosubstitution chemistry and the photolabile nature of the metal-ligand bond upon excitation. Finding platforms to study these vexing photophores as well as increasing the lifetimes of photophysical events for observation is very important to further our understanding of these chemically important molecules.

One of the main properties limiting Ru-polypyridyl compounds is the thermally accessible transition to the dd-state from the metal-to-ligand charge transfer ($MLCT^1$) state. The dd-state or metal centered excited state is non-emissive and provides thermal decomposition pathways in the excited state, thereby limiting the overall quantum yield and photostability of the ruthenium species. In particular, the $[Ru(bpy)_2(py)_2]^{2+}$ complex (where bpy = 2,2'-bipyridine and py =

pyridine) undergoes a rapid transition of up to 8.7 x 10^6 s^{-1} to the dd-state when irradiated, [10] leading to the cleavage of a metal-pyridine bond and photosubstitution by coordinating solvents and other ligands. As a result, the $[Ru(bpy)_2(py)_2]^{2+}$ compound is inherently difficult to study as most solution based photophysical techniques result in photosubstitution processes resulting in the partial data collection of a species of non-interest.

Metal-organic frameworks (MOFs) have been recently shown to provide a highly tunable platform to study photophysical phenomena[11-17] and reactive photocatalytic intermediates.[18] Additionally, MOFs can drive the uptake of charged species by using a lattice of the opposite charge, resulting in a densely packed system of a species of interest.[19-21] Herein we report the use of an anionic Zn-oxalate MOF to entrap the photo-labile $[Ru(bpy)_2(py)_2]^{2+}$ species. By shutting down the ligand exchange process while simultaneously providing an environment that restricts motion, encapsulation of $[Ru(bpy)_2(py)_2]^{2+}$ in MOF cavities significantly increases the lifetime of emissive states to drastically enhance its luminesence quantum yield.

4.2 Results and Discussion

4.2.1 Material Synthesis and Characterization

We chose to study the $[Ru(bpy)_2(py)_2]^{2+}$ complex confined in a zinc oxalate framework due to the close-fitting matrix the zinc oxalate forms around octahedral metal complexes as well as the negatively charged framework, which drives the uptake of the cationic metal complex within the MOF. As a result of our efforts, we were able to effectively stabilize the $[Ru(bpy)_2(py)_2]^{2+}$ ligand under irradiation as well as increase both the quantum yield and excited state lifetime as compared to the homogenous control.

The $[Ru(bpy)_2(py)_2]^2$ encapsulated MOF material (Ru@MOF) was synthesized in a solvothermal preparation. A mixture of $[Ru(bpy)_2(py)_2][PF_6]$, oxalic acid, $Zn(NO)_3$-$6H_2O$, and

hydrochloric acid in nitrogen saturated dimethylformamide (DMF) was heated at 70˚C under nitrogen for 24 hours to yield a highly crystalline product of the formula $[Ru(bpy)_2(py)_2][Zn_2(C_2O_4)_3]_2$ (Ru@MOF). Ru@MOF crystallizes in the cubic $P4_132$ space group and contained a significant proportion of large single crystals. Zn^{2+} ions are coordinated with six O atoms from three oxalates with each oxalate bridging two Zinc-oxo clusters to form an infinite 3-D anionic framework (Figure 4.1a). The $[Ru(bpy)_2(py)_2]^{2+}$ cations are encapsulated in the cavities of the anionic Zn-oxalate framework to afford a neutral host-guest system. Experimental powder X-ray diffraction (PXRD) patterns of Ru@MOF matched the simulated spectrum of the single crystal very well (Figure 4-1c), indicating phase purity of Ru@MOF samples. Space-filling models indicate a tight fit between the steric bulk of the $[Ru(bpy)_2(py)_2]^{2+}$ and the cavities in the zinc-oxalate framework, leading to a high calculated density of 1.79g/cm^3 and leaving no room for trapped solvent molecules. The nearest atom distance between $[Ru(bpy)_2(py)_2]^{2+}$ and the zinc-oxalate framework was calculated be between 1.37 and 1.28 Å (Figure 4-9). The tight fit between host framework and guest $[Ru(bpy)_2(py)_2]^{2+}$ cations is supported by the thermogravimetric analysis (TGA) result which showed negligible weight loss between room temperature and the decomposition of Ru@MOF at ~390 ˚C (Figure 4-2a). TGA showed a weight loss of 68.9% between 360-390 ˚C, matching well with the calculated weight loss of 67.4% for the complete conversion of Ru@MOF into RuO_2 and ZnO. Nitrogen sorption studies indicate that Ru@MOF is nonporous with a negligible Brunauer-Emmitt-Teller (BET) surface area of 5.76 $m^2 \cdot g^{-1}$ (Figure 4-2b), further supporting the tight fit between the host framework and guest $[Ru(bpy)_2(py)_2]^{2+}$ cations in Ru@MOF.

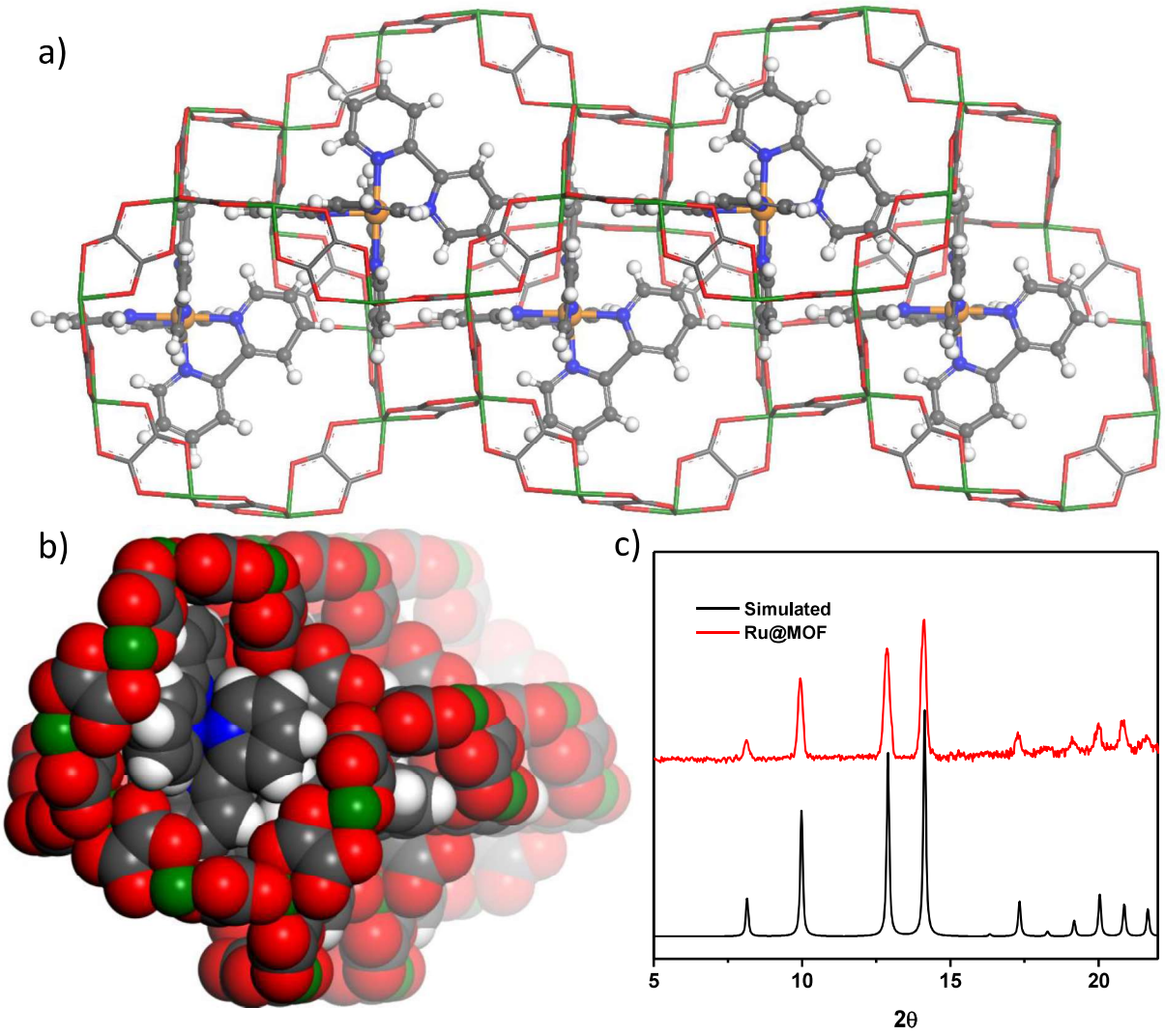

Figure 4-1. a) The structure of Ru@MOF showing encapsulation of $[Ru(bpy)_2(py)_2]^{2+}$ in anionic 3D $[Zn_2(ox)_3]^{2-}$ framework. b) Space filling model showing tight fit between $[Ru(bpy)_2(py)_2]^{2+}$ and the anionic cage of 3D $[Zn_2(ox)_3]^{2-}$ framework. Red = oxygen, blue = nitrogen, gray = carbon, orange = ruthenium, green = zinc, and white = hydrogen. c) The PXRD pattern of Ru@MOF matches that simulated from the single crystal structure.

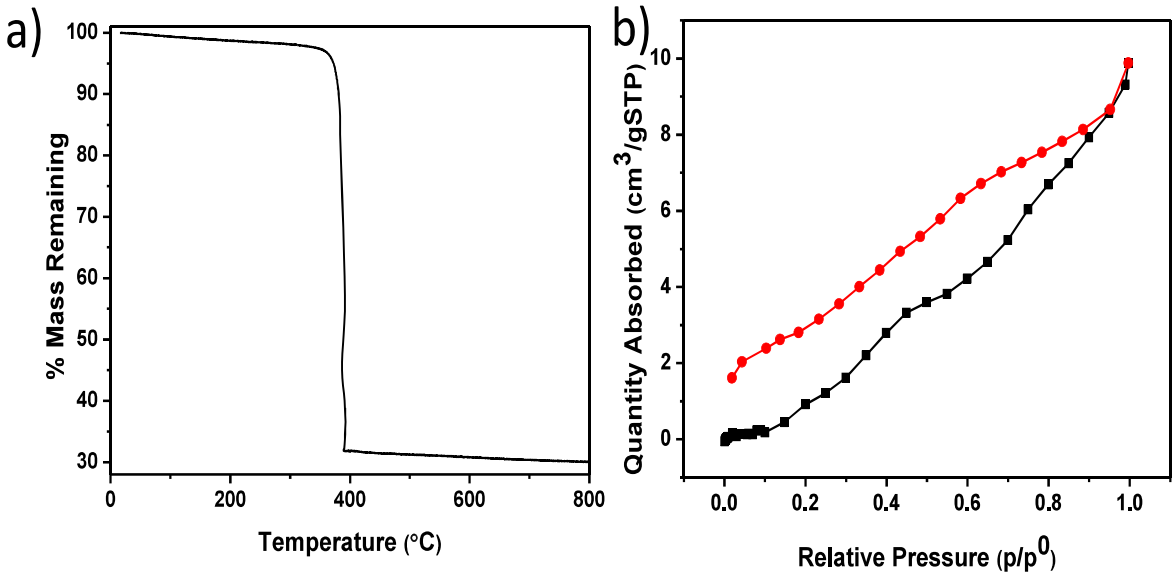

Figure 4-2. a) The thermogravimetric analysis of Ru@MOF and b) BET analysis of Ru@MOF.

4.2.2 Spectroscopic Analysis

Ru@MOF was further characterized with steady state absorption and emission spectroscopies. The absorption properties of entrapped $[Ru(bpy)_2(py)_2]^{2+}$ in Ru@MOF closely resemble those of the homogenous species, however, with a slight red-shift for the absorption maximum (Figure 4-3). A broad absorbance peak with a maximum at 491 nm is attributed to the partially allowed ^{1}MLCT state to the bipyridine, while another strong absorption observed at 369 nm corresponds to the ^{1}MLCT to the pyridine ligands.

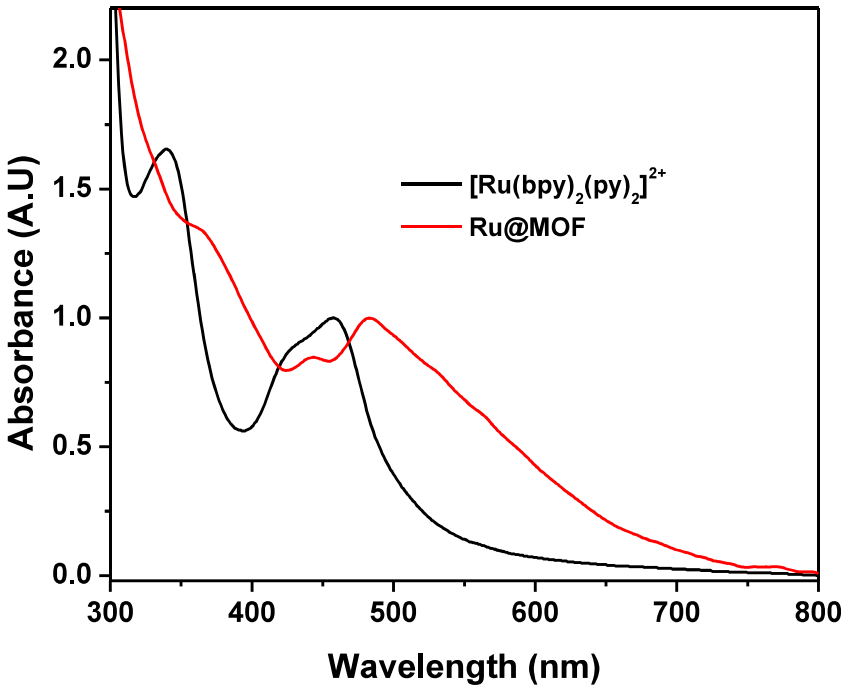

Figure 4-3. The UV-visible absorption spectra of $[Ru(bpy)_2(py)_2](PF_6)_2$ (black) and Ru@MOF (red) in ethanol:methanol (4:1 V/V).

The emission spectra of Ru@MOF show three distinct emission maxima at 585 nm, 639 nm, and 682 nm, which are not visible in the homogenous species (Figures 4-4). These three peaks have been attributed to the vibrational progressions of the $[Ru(bpy)_2(py)_2]^{2+}$ molecule within the confines of the MOF. [11] The solvent free matrix within the MOF prevents coupling of vibrational modes to the solvent resulting in a sharpening of J ±1 transitions. Deviations in the emission maxima intensities of the three vibrational progressions were observed with various sample trials from the same batch of starting material, with spectra associated with Ru@MOF1 (Figure 4-4a) being most prevalent. This variability likely occurred as a result of variable oxygen content within the MOF at different time points after synthesis leading to the quenching of the ^{3}MLCT state.

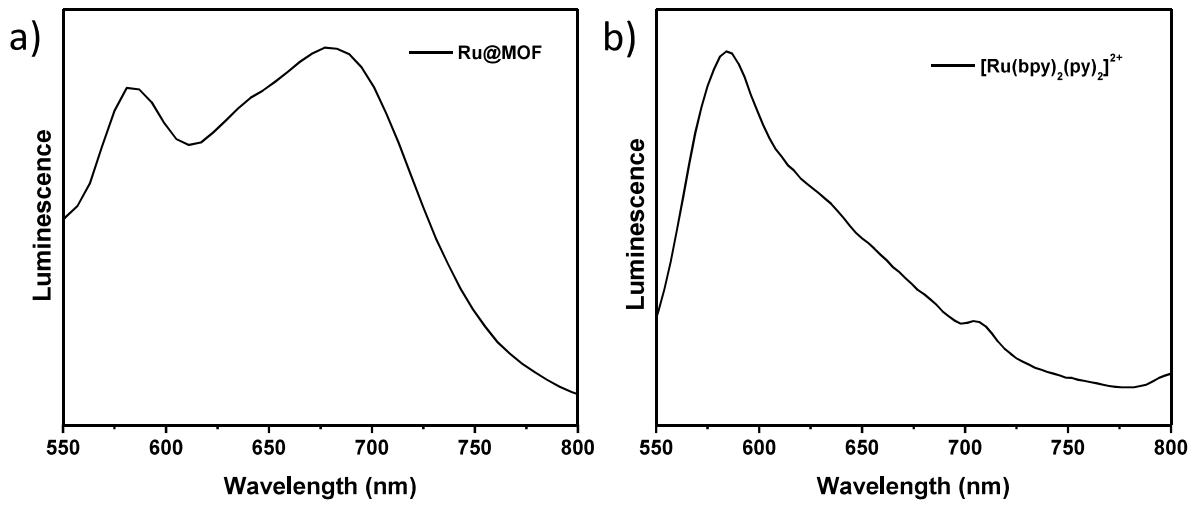

Figure 4-4. a) The steady state emission spectra of a) Ru@MOF and b) $[Ru(bpy)_2(py)_2]^{2+}$ at room temperature in an alcoholic solution (ethanol : methanol 4:1 V:V).

To further elucidate the excited state properties, the emission spectra was taken at decreasing temperatures down to 140 K. (Figure 4-5) It is known that at around 200 K the transition to the dd-state from the $MLCT^3$ state becomes thermally inaccessible, thereby greatly improving the quantum yield of the material. [22] As expected in the low temperature spectra, the emission intensity of the $[Ru(bpy)_2(py)_2]^{2+}$ compound within the MOF increases as temperature decreases. However, the relative change in intensity of the three emission maxima was noteworthy. As temperature drops, the overall and relative intensity of the second vibrational progression (650 nm) greatly increases relative to the peaks at 585 and 690 nm. It is hypothesized that the dd-state is entered from this state and is responsible for the majority of non-emissive deactivation pathways in said molecule.

The observed vibrational modes correlate well with past theoretical analysis derived from Frank-Condon fit factors (Figure 4-6). [10] The Frank-Condon fit was performed according to Equation (1) where $I(\tilde{\nu})$ is the emission intensity in cm^{-1}, S_M and S_L are Huang-Rhys factors

corresponding to the excited state distortion, v_M is the vibrational spacing, E_0 is the energy gap between the zeroth vibrational levels of the ground and excited states, $\hbar\omega_M$ and $\hbar\omega_L$ are the quantum spacings for two averaged acceptor vibrational modes of medium and low frequency respectively, and $v_{\frac{1}{2}}$ is the full width half-maximum for individual vibrionic lines. The resulting calculated emission spectra show three major peak intensities at wavelengths of 581 nm, 633 nm, and 695 nm.

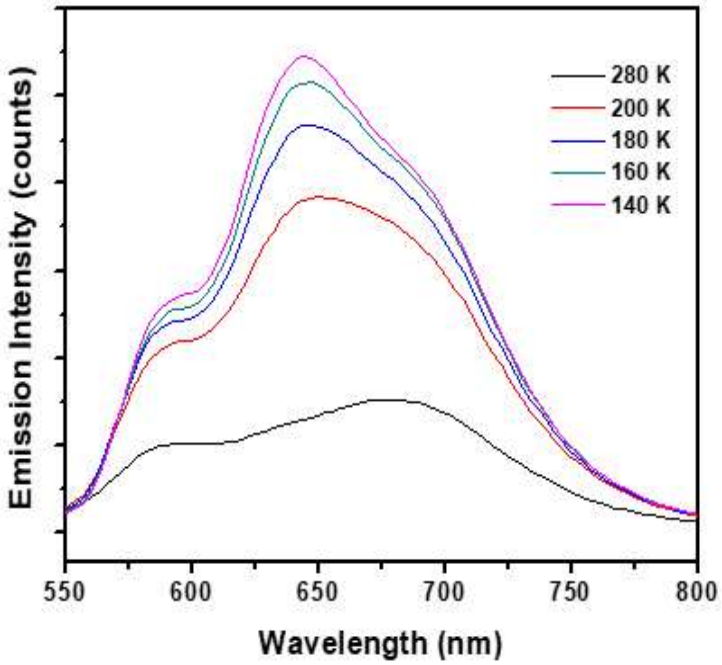

Figure 4-5. The temperature dependent PL spectra of Ru@MOF upon excitation at 455 nm in a 4:1 ethanol:methanol solvent.

$$I(\tilde{\nu} = \sum_{v_M=0}^{N} \sum_{V_L=0}^{N} \left(\frac{E_0 - v_M \hbar\omega_M - v_L \hbar\omega_L}{E_0}\right)^4 \left(\frac{S_M^{v_M}}{v_M!}\right) \left(\frac{S_L^{v_L}}{v_L!}\right) * \exp[-4\ln(2)) \left(\frac{\tilde{\nu} - E_0 + v_M \hbar\omega_M + v_L \hbar\omega_L}{\widetilde{v_{\frac{1}{2}}}}\right)^2 \quad \textbf{4-1}$$

Table 4-1. The parameter values used in Equation 4-1 to generate the theoretical emission pattern of $[Ru(bpy)_2(py)_2]^{2+}$ at 77 K.

Parameter	Value	Units
S_M	1.29	n/a
S_L	2.00	n/a
E_0	17370	cm^{-1}
$\hbar\omega_M$	1380	cm^{-1}
$\hbar\omega_L$	300	cm^{-1}
$v_{\frac{1}{2}}$	530	cm^{-1}

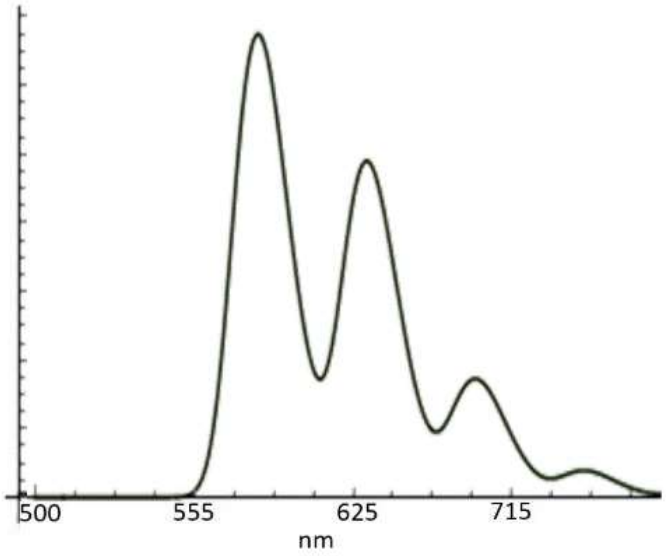

Figure 4-6. The Frank-Condon fit of the $[Ru(bpy)_2(py)_2]^{2+}$ complex shows four distinct vibrational modes at 77 K which match the observed photoluminescent spectra of Ru@MOF well.

The emissive state of $[Ru(bpy)_2(py)_2]^{2+}$ within the confines of the MOF was further analyzed by photoluminescent (PL) lifetime spectroscopy. The excitation wavelength used was 450 nm, while filters were used to probe the emissive lifetime of the three PL maxima: 593 ± 50 nm, 641 ± 75 nm, and 690 ± 100 nm (Figure 4-7). It was observed that longer lifetime phenomena were associated with lower energy emissions. This is a result of the occupation of lower energy vibrational modes as energy transfer propagates throughout the lattice in agreement with the relative intensities of the emission peaks found in the steady state PL spectra. Furthermore, it was found that the lifetime of the excited state for the $[Ru(bpy)_2(py)_2]^{2+}$ species encapsulated by the MOF was over 100 times longer than the PL lifetime for the homogenous sample. The longest observed lifetime was 1.3 μs which corresponds to about 10% f-weight of the overall lifetime for the emission wavelengths 695 ± 100 nm. The tremendous increase in lifetime observed for the MOF-encapsulated species can be attributed to the confinement effect of the molecular species in the MOF. In solvent free matrices with limited rotational, translational, and vibrational freedom, the rate of transition to the dd-state is decreased due to a large increase in the pre-exponential factor of its rate-law, [22] minimizing the available non-emissive pathways for the excited state. The destabilization of the dd-state due to steric effects results in a lower population of electrons in dark states within Ru@MOF, resulting in an eight-fold increased quantum yield as determined from the integration of the photoluminescent spectrum of the MOF relative to homogenous species with equal absorption maxima (Figure 4-8).

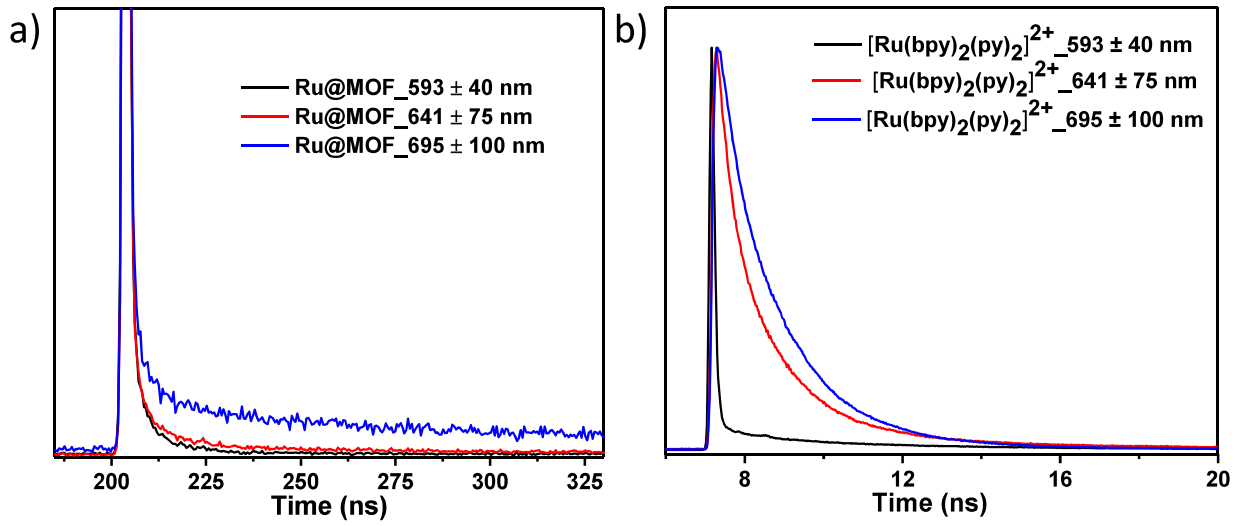

Figure 4-7. a) Time-resolved fluorescence of a DMF dispersion of Ru@MOF and b) a DMF solution of $[Ru(bpy)_2(py)_2]^{2+}$ $(PF_6)_2$ when excited at 455 nm

Table 4-2. The results of the photoluminescence lifetime measurements for both Ru@MOF and $[Ru(bpy)_2(py)_2]^2$ in DMF at varying emission wavelengths.

Ru@MOF

Excitation λ (nm)	Emission λ (nm)	τ_1 (ns)	τ_2 (ns)	F-Weighted Lifetime (ns)
450	593 ± 40	10.6	2.06	6.02
450	641 ± 75	111	5.17	71
450	695 ± 100	149	5.65	123

$[Ru(bpy)_2(py)_2]^{2+}$ homogenous

Excitation λ (nm)	Emission λ (nm)	τ_1 (ns)	τ_2 (ns)	F-Weighted Lifetime (ns)
450	593 ± 40	4.99	0.036	2.53
450	641 ± 75	3.29	0.87	1.8
450	695 ± 100	3.01	1.31	1.63

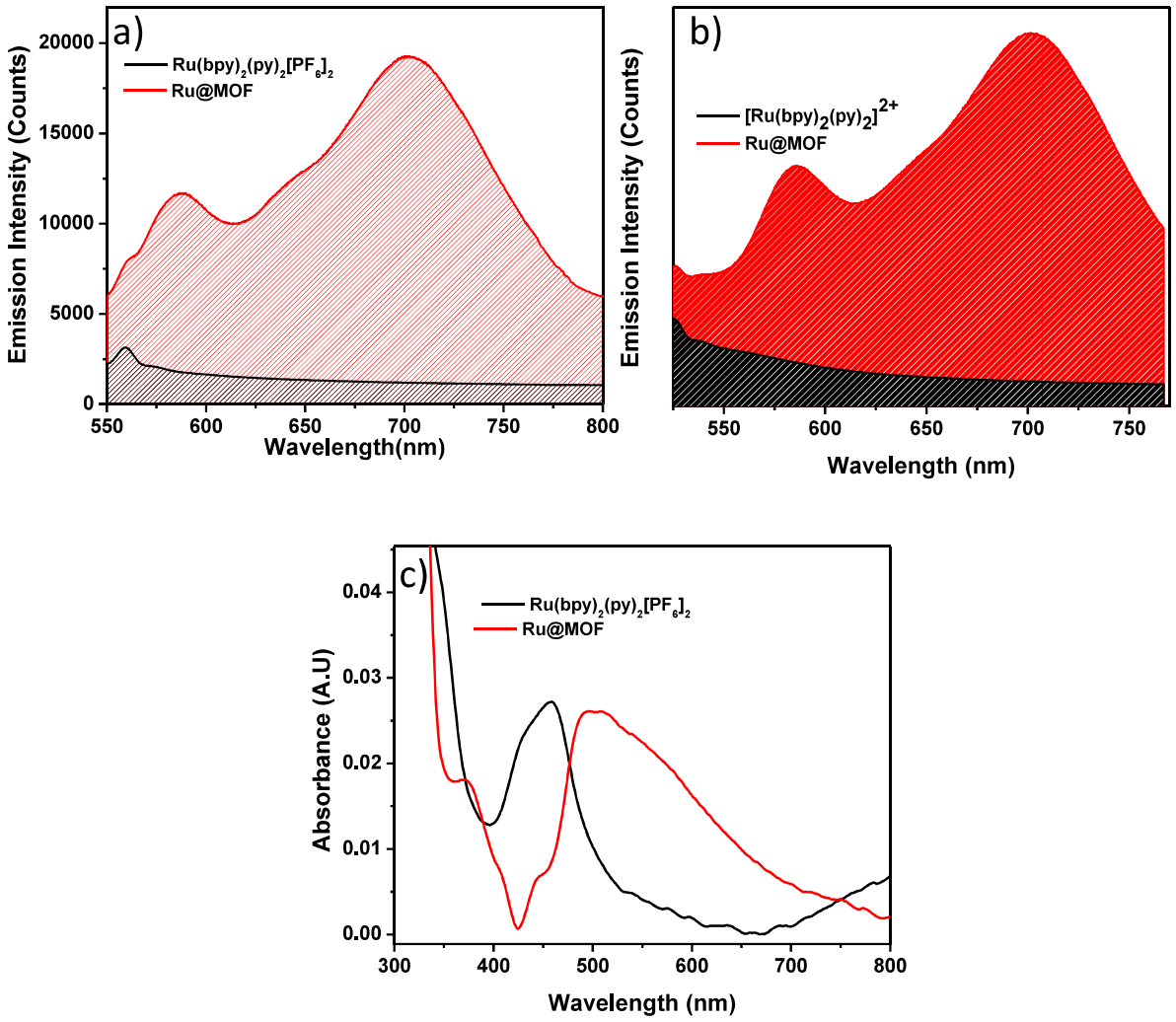

Figure 4-8. a) The emission spectra of the $Ru(bpy)_2(py)_2]^{2+}$ complex and Ru@MOF upon excitation at 476 nm and b) 455 nm light in DMF. c) The UV-VIS spectra of Ru@MOF and $[Ru(bpy)_2(py)_2]^{2+}$ used in the emission studies in a,b.

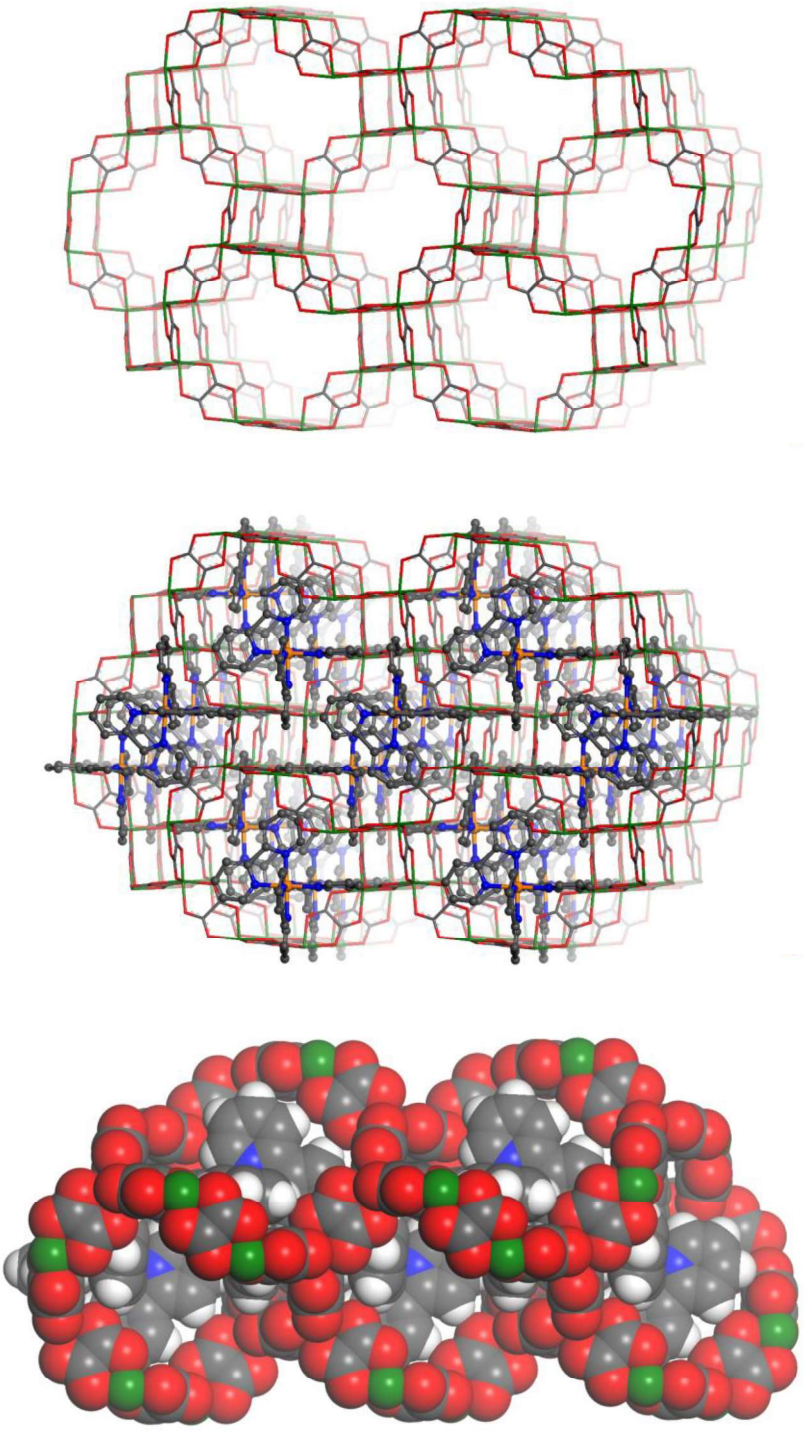

Figure 4-9: Top) Stick model showing the anionic Zn-oxlate framework in Ru@MOF. Middle) Structural model showing the encapsulation of *cis*-$[Ru(bpy)_2(py)_2]^{2+}$ cations inside the anionic $Zn_2(ox)_3^{2-}$ framework. Bottom) Space-filling model showing tight fit between *cis*-$[Ru(bpy)_2(py)_2]^{2+}$ cations and the cages of the anionic $Zn_2(ox)_3^{2-}$ framework in Ru@MOF. Red = oxygen, grey = carbon, green = zinc, blue = nitrogen, orange = ruthenium, and white = hydrogen.

Table 4-3. The crystal data and structure refinement of Ru@MOF at 100K and without visible light radiation.

	Ru@MOF
Empirical formula	$C_{36}H_{24}N_6RuO_{12}Zn_2$
M	964.46
λ/Å	0.41328
T/K	100
Crystal System	Cubic
Space Group	$P4_132$
a/Å	15.2903(5)
V/Å^3	3574.8(4)
Z	4
D_c/g *c*m^{-3}	1.792
μ/mm^{-1}	0.920
F(000)	1928.0
θ Range/°	1.095 to 15.295
$R_1(I > 2\sigma(I))$[a]	0.0630
wR_2	0.1471
Goodness of fit	1.265
Empirical formula	$C_{36}H_{24}N_6RuO_{12}Zn_2$

Table 4-4. The single crystal parameters and structure refinement of Ru@MOF at 200K and without visible light radiation.

	Ru@MOF
Empirical formula	$C_{36}H_{24}N_6RuO_{12}Zn_2$
M	964.46
λ/Å	0.41328
T/K	200
Crystal System	Cubic
Space Group	$P4_132$
a/Å	15.3625(4)
α/°	90
V/Å	3625.7(3)
Z	4
D_c/g *c*m^{-3}	1.767
μ/mm^{-1}	0.907
F(000)	1928
θ Range/°	1.090 to 17.158
$R_1(I > 2\sigma(I))$[a]	0.0801
wR_2	0.1700
Goodness	1.312

Table 4-5. The single crystal parameters and structure refinement of Ru@MOF at 100K and with 2.7mw visible light radiation.

	Ru@MOF
Empirical formula	$C_{36}H_{24}N_6RuO_{12}Zn_2$
M	964.46
λ/Å	0.41328
T/K	100
Crystal System	Cubic
Space Group	$P4_132$
a/Å	15.3464(4)
α/°	90
V/Å	3614.3(3)
Z	4
D_c/g *c*m^{-3}	1.773
μ/mm^{-1}	0.910
F(000)	1928.0
θ Range/°	1.091 to 21.760
$R_1(I > 2\sigma(I))$[a]	0.1059
wR_2	0.2187
Goodness	1.228

Table 4-6. The single crystal parameters and structure refinement of Ru@MOF at 200K and with 2.7 mW visible light radiation

	Ru@MOF
Empirical formula	$C_{36}H_{24}N_6RuO_{12}Zn_2$
M	964.46
λ/Å	0.41328
T/K	200
Crystal System	Cubic
Space Group	$P4_132$
a/Å	15.3704(6)
α/°	90
V/Å	3631.3(4)
Z	4
D_c/g cm^{-3}	1.764
μ/mm^{-1}	0.906
F(000)	1928.0
θ Range/°	1.089 to 20.523
$R_1(I > 2\sigma(I))$[a]	0.1038
wR_2	0.2282
Goodness	1.130

Table 4-7. The single crystal parameters and structure refinement of Ru@MOF at 100K and with 4.5mW visible light radiation.

	Ru@MOF
Empirical formula	$C_{36}H_{24}N_6RuO_{12}Zn_2$
M	964.46
λ/Å	0.41328
T/K	100
Crystal System	Cubic
Space Group	$P4_132$
a/Å	15.3428(4)
α/°	90
V/Å	3611.7(3)
Z	4
D_c/g *c*m^{-3}	1.774
μ/mm^{-1}	0.911
F(000)	1928.0
θ Range/°	1.091 to 20.781
$R_1(I > 2\sigma(I))$[a]	0.1035
wR_2	0.2130
Goodness	1.234

Table 4-8. The single crystal parameters and structure refinement of Ru@MOF at 200K and with 4.5mW visible light radiation.

	Ru@MOF
Empirical formula	$C_{36}H_{24}N_6RuO_{12}Zn_2$
M	964.46
λ/Å	0.41328
T/K	200
Crystal System	Cubic
Space Group	$P4_132$
a/Å	15.3735(7)
α/°	90
V/Å	3633.4(5)
Z	4
D_c/g *c*m^{-3}	1.763
μ/mm^{-1}	0.906
F(000)	1928
θ Range/°	1.089 to 21.310
$R_1(I > 2\sigma(I))$[a]	0.0992
wR_2	0.2496
Goodness	1.045

Table 4-9. The calculated Ru-N bond length from SXRD of Ru@MOF under varying intensities of 450 nm light.

Laser Power (mW/cm^2)	Ru-N Bond length at 100 K (Å)	Ru-N Bond length at 200K (Å)
0	2.0995	2.1287
84	2.0473	2.08605
140	2.0806	2.04497

The long-lived lifetime of the excited state allows for the ability to test the effectiveness of the Ru@MOF matrix on photophore stability through Photo-Xray Crystallography (Photo-XTAL), since the excited state was measured to be longer than the time between photon packets at the Argonne National Laboratory synchrotron. Photo-XTAL experiments were conducted using a 450

nm laser at varying powers and the thinnest single crystal of Ru@MOF available. Prior to all experiments, the crystal was kept for one hour in the dark to decrease the population density of photoexcited electrons to a minimum. Under irradiation, the Ru-N (pyridine) bond has been calculated to be 2.18 Å and 2.80 Å while the bond length of the Ru-N (bipyridine) bond was calculated to be 2.03 Å and 2.37 Å in the MLCT^3 and dd-state, respectively for the homogenous $[Ru(bpy)_2(py)_2]^{2+}$ complex. [23] The Photo-XTAL results of the irradiated sample compared to that of the dark scans show no significant change in global or local structure for Ru@MOF (Figure 4-9). The only appreciable structural changes correspond to an increase in disorder among the bipyridine motifs with increasing temperature and laser intensity due to increased ambient energy and more transitions to the ligand centered ^{3}MLCT state. The list of all Ru-N bond lengths can be found in Table 2 and show a consistent Ru-N bond length at all temperatures and light intensities. The bond lengths reported do not match those of the calculated complex because the Ru-bpy and Ru-py bonds were averaged across the cubic space-group. The slight decrease in Ru-N bond lengths observed upon irradiation shows that the dd-state was not entered and the Ru-py bond was not elongated.[24] From these results it can be seen that the ruthenium complex is completely confined by the MOF matrix. Not only is the labile pyridine bond kept in place, but elongation of the bond is encumbered by the steric forces of the surrounding zinc oxalate species, destabilizing the dd state and leading to its inaccessibility. Furthermore, the same crystal was able to undergo over five hours of irradiation with direct laser light while retaining crystallinity and ruthenium pyridine bonds attesting to the stability that the MOF matrix provides.

The inhibition of photosubstitution of the $[Ru(bpy)_2(py)_2]^{2+}$ photophore within the confines of the MOF matrix was confirmed from the absorbance spectra of the ligand in the presence of a white light emitter. For the experiment, a white light source was used to irradiate Ru@MOF in the

presence of tetrabutyl ammonium chloride, serving as source of chlorine atoms for substitution chemistry. The homogenous analogue is shown to undergo substantial photosubstitution in less than one minute with complete photosubstution observed after five minutes as determined by UV-VIS spectroscopy. For the MOF encapsulated species, the absorbance band at 480 nm was stable for at least thirty minutes of direct irradiation as minimal red shifting of the ^{3}MLCT band was observed (Figure 4-10). This stability also extends to the emission spectra, as the MOF retains 96.1% of its emission intensity after five minutes of irradiation while the homogenous only retains 39.9 % of its native emission intensity. Furthermore, after irradiation up to 6 hours, 0.04% leaching of Ru is observed as determined by ICP-MS.

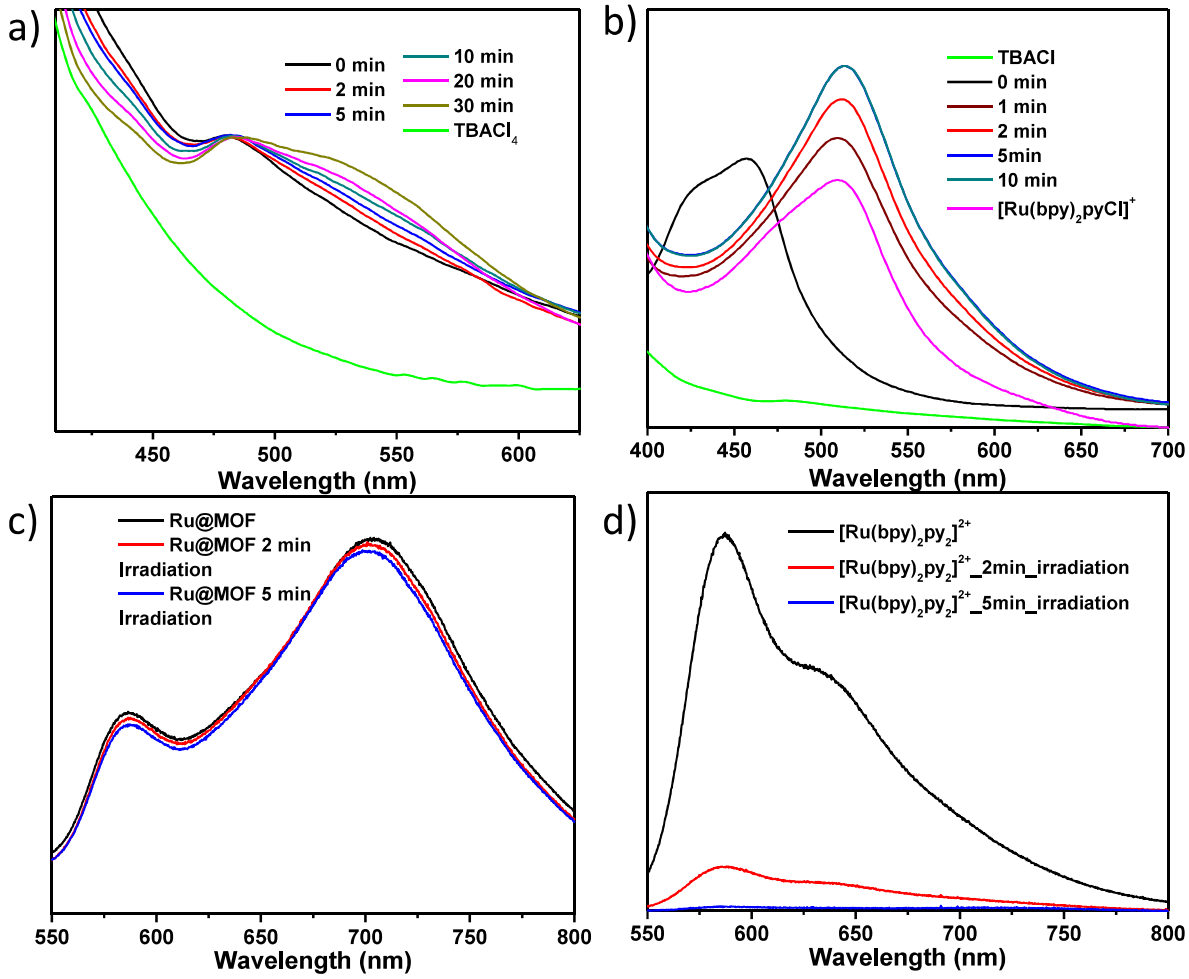

Figure 4-10. a) Photostability studies of Ru@MOF irradiated in the presence of TBACl compared to the b) homogenous analogue in DMF. c) Fluorescent stability studies of Ru@MOF upon irradiation with white light compared to the d) homogenous species in ethanol: methanol 4:1 without a chloride source. Excitation wavelength is 455 nm.

The stability of the $[Ru(bpy)_2(py)_2]^{2+}$ complex in the zinc oxalate MOF matrix allows for further studies of the photoexcited state with transient absorption studies. Transient absorptions have been performed on the $[Ru(bpy)_2(py)_2]^{2+}$ complex prior,[23] however, due to the photolability of the material, it is difficult to ensure that spectra collected correlates with the complex of interest. To mitigate this factor, the study could not look for long lived excited state properties and focused on picosecond phenomena. By confining the $[Ru(bpy)_2(py)_2]^{2+}$ complex in the zinc oxalate MOF,

transient absorption spectroscopy on the nanosecond regime could be performed on the $[Ru(bpy)_2(py)_2]^{2+}$ complex, as the MOF framework prevents photosubsitution chemistry and results in excited state lifetimes in the nanosecond regime. For these transient absorption studies, a 450 nm pulse was used as the pump while a while light source served as a probe. The scattering of the MOF species necessitated at least 55 scans averaged together to improve signal to noise. The transient results expectedly show bleaching at 450 nm for the first 10 nanoseconds of the MOF species compared to that of just 3 ns for the homogenous sample. Furthermore, the homogenous species shows bleaching for up to 0.5 ns at 475 nm. This is a result of photosubsitution of the pyridine ligand, as a similar transition can be observed when the $Ru(bpy)_2(py)_2]^{2+}$ complex is subjected to white light for one minute in ethanol/methanol solution. There is no sign of photosubstitution in the MOF sample. For the MOF, there is no other transient absorption signal detected at any wavelength other than 450 nm until 100 ns after excitation where a broad excited state absorption centered at 575 nm was observed. Based on PL lifetimes, the excited state absorption correlates to a transition from the long lived 695 nm emission band. Energetically, the 650 nm absorption matches the energy gap needed for the excited state to migrate from the lowest energy bipyridine ligand mode to that of the pyridine ligand (absorbance at 369 nm).

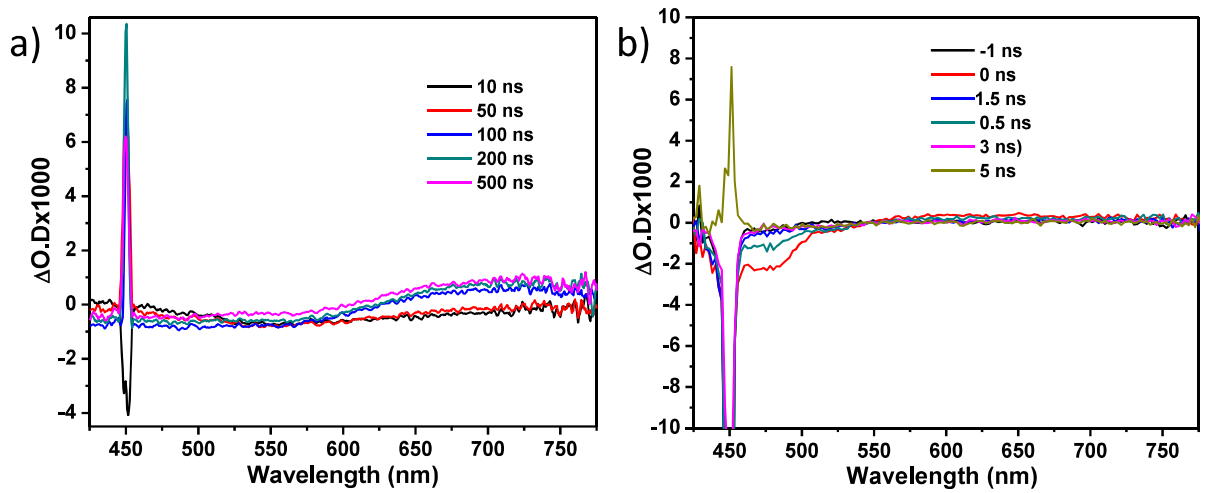

Figure 4-11. a) The transient absorption studies in the nanosecond regime of Ru@MOF and b) the homogenous species with a pumping wavelength of 450 nm in DMF.

4.3 Conclusion

Through the successful incorporation of the photolabile $[Ru(bpy)_2(py)_2]^{2+}$ complex into solvent-free tight-fitting MOF pores, the photophyiscal properties of $[Ru(bpy)_2(py)_2]^{2+}$drastically improved. The increase in PL lifetime, quantum yield, and stability of the $[Ru(bpy)_2(py)_2]^{2+}$ complex allows for novel characterization including but not limited to nanosecond transient absorption. The encapsulation of photophores into MOF cavities for stability purposes can be applied to other photosensitizers or labile compounds, allowing for improved and novel characterization, furthering our understanding of these molecules' properties.

4.4 Experimental Methodologies

4.4.1 X-Ray Structure Determination: The diffraction data was collected with a Bruker APEX II CCD-based detector at the Advanced Photon Source located at Argonne National Laboratory. The raw data was integrated with the APEX II software package. The structure was solved by direct methods using least squares methods and the SHELXTL software suite. The

resulting HKL file was then imported into OLEX2 and edited and refined until fully solved. For the PhotoXTAL experiments, a ThorLabs CPS450 laser diode module was used with a center wavelength of 450 nm and an output power of 4.5 mW.

4.4.2 X-Ray Powder Diffraction: Powder diffraction data was collected with a Bruker D8 Venture diffractometer with a diffraction wavelength (CuK) of 1.5418 Å. The PXRD patterns were processed with the APEX2 package using PILOT plug-in.

4.4.3 Single Crystal X-Ray Diffraction: The diffraction data was collected with a Bruker APEX II CCD-based detector at the Advanced Photon Source located at Argonne National Laboratory. The raw data was integrated with the APEX II software package. The structure was solved by direct methods using least squares methods and the SHELXTL software suite. The resulting HKL file was then imported into OLEX2 and edited and refined until fully solved. For the PhotoXTAL experiments, a ThorLabs CPS450 laser diode module was used with a center wavelength of 450 nm and an output power of 4.5 mW.

X-ray crystallography data gave a long C1-C1' distance of 3.128 Å[25] as a result of the free rotation of the pyridine ligands as opposed to a distance of 1.48 Å between the same bridging carbons of a bipyridine.

4.4.4 Photoluminescence Spectra: The PL spectra were measured by a Flurolog-3 Yobin Yvon-Horiba fluorimeter. Add more details on the instrument settings etc.

4.4.5 Photoluminescent Lifetime Measurements: Lifetime measurements were measured by a ChronosBH lifetime fluorimeter (ISS, INC) using time-correlated single photon counting methods. Excitation was provided with a picosecond pulsed laser source (Hamamatsu PLP-10). Emission wavelengths were selected using interference filters.

4.5 Synthetic Procedures

4.5.1 Synthesis of Ligands

Synthesis of $Ru(DMSO)_4Cl_2$: 380 mg of $RuCl_3$-$3H_2O$ was dissolved in 25 mL of ethanol and refluxed under nitrogen for one hour. While the solution was hot, 518 mL of dimethyl sulfoxide (DMSO) was added and the resulting solution was refluxed an additional hour, turning yellow. The solvent was then removed via rotary evaporation and washed and filtered with cold acetone followed by diethyl ether. 582 mg of orange yellow product were collected. (82.6 % yield)

Synthesis of *cis*-$Ru(bpy)_2Cl_2$: 130 mg of $Ru(DMSO)_4Cl_2$ was combined with 89.5 mg 2,2'-bipyrdine (bpy) and 595 mg lithium chloride in 25 mL DMF. The solution as refluxed under nitrogen gas overnight to yield a deep purple solution. As much DMF as possible was removed via rotary evaporation resulting in a purple oil. The oil was subsequently diluted with acetone cooled by dry ice and kept on ice. The resulting crystals were collected via vacuum filtration and washed with cold acetone then ether to give a dark purple product. ^{1}H-NMR (500MHz, DMSO-D, ppm): δ= 9.936 (s, 2H), δ= 8.634 (d, 2H), δ= 8.488 (d, 2H), δ= 8.069 (t, 2H), δ= 7.760 (t, 2H), δ= 7.662 (t, 2H), δ= 7.475 (s, 2H), δ= 7.105 (t, 2H).

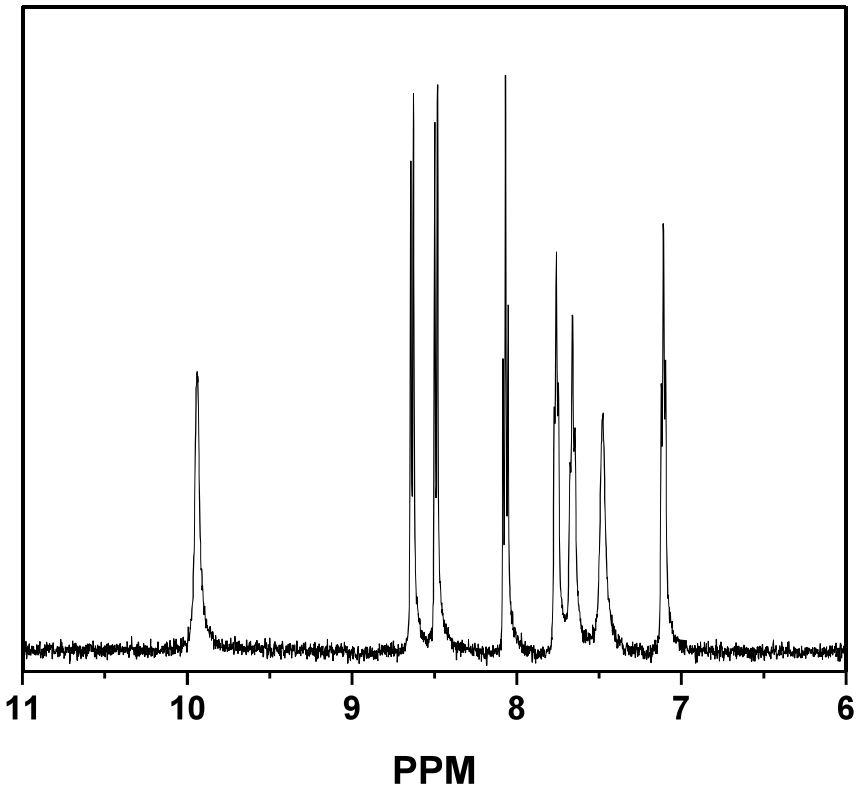

Figure 4-12. The ^{1}H-NMR of *cis*-Ru(bpy)$_2$Cl$_2$ in (CD$_3$)$_2$SO.

Synthesis of *cis*-Ru(bpy)$_2$(py)$_2$[PF$_6$]$_2$: 105 mg of *cis*-Ru(bpy)$_2$Cl$_2$ was combined with 450 µL of pyridine (µmol, 2.55 equivalents) and dissolved in 20 mL methanol and distilled water (2:1 Methanol: H_2O). The resulting solution was refluxed for four hours under nitrogen flow in the dark at 90˚C. The solvent was subsequently removed by rotary evaporation. The orange solid was dissolved in a minimal amount of methanol and crashed out with the addition of ammonium hexafluorophosphate (NH_4PF_6) 0.1 M in water. The solid was extracted five times with dichloromethane (DCM), collecting the organic phase. The DCM was removed via rotary evaporation and the resulting orange solid was dissolved in a minimal amount of methanol

followed by the addition of diethyl ether to afford a bright orange solid. The solid was collected via vacuum filtration and washed with ether (102 mg, 55%).

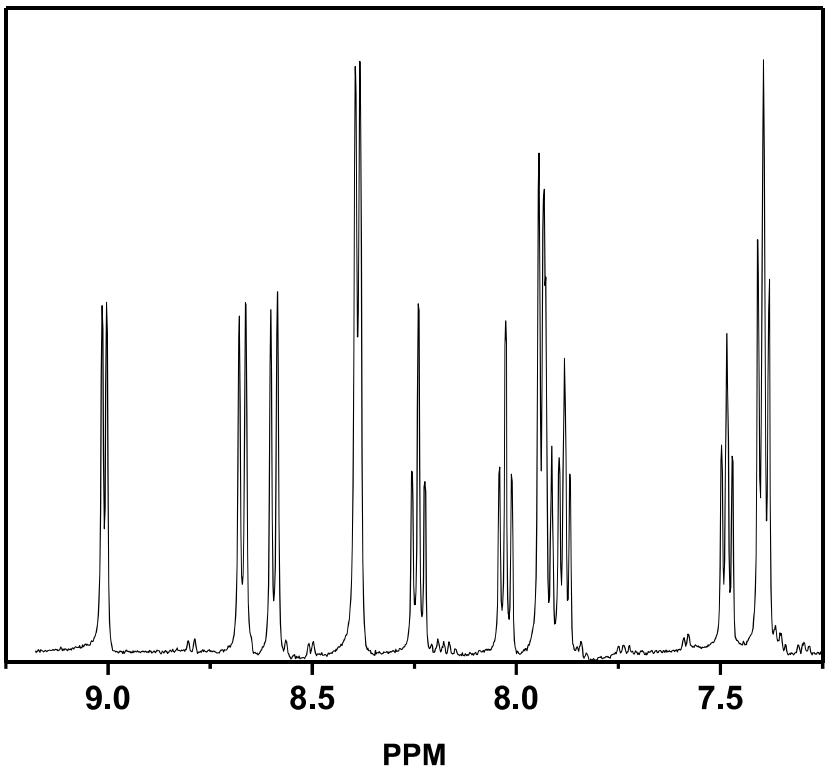

Figure 4-13. The ^{1}H-NMR of *cis*-$Ru(bpy)_2(py)_2[PF_6]_2$ in $(CD_3)_2SO$.

4.5.2 Synthesis of MOFs

Synthesis of $[Ru(bpy)_2(py)_2][Zn_2(C_2O_4)_3]$ (*Ru@MOF)*: 4 mg of *cis*-$Ru(bpy)_2(py)_2[PF_6]_2$ and 3 mg of $Zn(NO_3)_2$-$6H_2O$ were dissolved in 800 µL of dimethylformamide followed by subsequent addition of 16 µL of 0.75 M oxalic acid in DMF, 300 µL H_2O, and 100 µL of 2 M hydrochloric acid. The entire solution was degassed with nitrogen for thirty minutes and kept under a nitrogen atmosphere for MOF growth. The solution was then placed in a 70 ˚C oven for twenty-four hours yielding large red crystals in modest yields (~5%). The crystals were then washed with DMF and ethanol before their use for other studies.

4.6 References

1. Vlcek, A., Jr., Femtosecond dynamics of excited-state evolution in [Ru(bpy)3]2+. *Chemtracts* **1998,** *11* (8), 621-625.

2. Nicewicz David, A.; MacMillan David, W. C., Merging photoredox catalysis with organocatalysis: the direct asymmetric alkylation of aldehydes. *Science* **2008,** *322* (5898), 77-80.

3. Yoon, T. P.; Ischay, M. A.; Du, J., Visible light photocatalysis as a greener approach to photochemical synthesis. *Nat. Chem.* **2010,** *2* (7), 527-532.

4. Youngblood, W. J.; Lee, S.-H. A.; Kobayashi, Y.; Hernandez-Pagan, E. A.; Hoertz, P. G.; Moore, T. A.; Moore, A. L.; Gust, D.; Mallouk, T. E., Photoassisted Overall Water Splitting in a Visible Light-Absorbing Dye-Sensitized Photoelectrochemical Cell. *J. Am. Chem. Soc.* **2009,** *131* (3), 926-927.

5. Chen, C.-Y.; Wang, M.; Li, J.-Y.; Pootrakulchote, N.; Alibabaei, L.; Ngoc-Le, C.-H.; Decoppet, J.-D.; Tsai, J.-H.; Gratzel, C.; Wu, C.-G.; Zakeeruddin, S. M.; Gratzel, M., Highly Efficient Light-Harvesting Ruthenium Sensitizer for Thin-Film Dye-Sensitized Solar Cells. *ACS Nano* **2009,** *3* (10), 3103-3109.

6. Gratzel, M., Dye-sensitized solar cells. *J. Photochem. Photobiol., C* **2003,** *4* (2), 145-153.

7. Sun, L.; Hammarstrom, L.; Akermark, B.; Styring, S., Towards artificial photosynthesis: ruthenium-manganese chemistry for energy production. *Chem. Soc. Rev.* **2001,** *30* (1), 36-49.

8. Howerton, B. S.; Heidary, D. K.; Glazer, E. C., Strained ruthenium complexes are potent light-activated anticancer agents. *J. Am. Chem. Soc.* **2012,** *134* (20), 8324-8327.

9. Buda, M.; Kalyuzhny, G.; Bard, A. J., Thin-Film Solid-State Electroluminescent Devices Based On Tris(2,2'-bipyridine)ruthenium(II) Complexes. *J. Am. Chem. Soc.* **2002,** *124* (21), 6090-6098.

10. Rillema, D. P.; Blanton, C. B.; Shaver, R. J.; Jackman, D. C.; Boldaji, M.; Bundy, S.; Worl, L. A.; Meyer, T. J., MLCT-dd energy gap in pyridyl-pyrimidine and bis(pyridine) complexes of ruthenium(II). *Inorg. Chem.* **1992,** *31* (9), 1600-6.

11. Kent, C. A.; Liu, D.; Ito, A.; Zhang, T.; Brennaman, M. K.; Meyer, T. J.; Lin, W., Rapid energy transfer in non-porous metal-organic frameworks with caged Ru(bpy)32+ chromophores: oxygen trapping and luminescence quenching. *J. Mater. Chem. A* **2013,** *1* (47), 14982-14989.

12. Lin, J.; Hu, X.; Zhang, P.; Van Rynbach, A.; Beratan, D. N.; Kent, C. A.; Mehl, B. P.; Papanikolas, J. M.; Meyer, T. J.; Lin, W.; Skourtis, S. S.; Constantinou, M., Triplet Excitation Energy Dynamics in Metal-Organic Frameworks. *J. Phys. Chem. C* **2013,** *117* (43), 22250-22259.

13. Zhang, Q.; Zhang, C.; Cao, L.; Wang, Z.; An, B.; Lin, Z.; Huang, R.; Zhang, Z.; Wang, C.; Lin, W., Förster Energy Transport in Metal-Organic Frameworks Is Beyond Step-by-Step Hopping. *J. Am. Chem. Soc.* **2016,** *138* (16), 5308-5315.

14. Lee, C. Y.; Farha, O. K.; Hong, B. J.; Sarjeant, A. A.; Nguyen, S. B. T.; Hupp, J. T., Light-Harvesting Metal-Organic Frameworks (MOFs): Efficient Strut-to-Strut Energy Transfer in Bodipy and Porphyrin-Based MOFs. *J. Am. Chem. Soc.* **2011,** *133* (40), 15858-15861.

15. Cao, L.; Lin, Z.; Shi, W.; Wang, Z.; Zhang, C.; Hu, X.; Wang, C.; Lin, W., Exciton Migration and Amplified Quenching on Two-Dimensional Metal-Organic Layers. *J. Am. Chem. Soc.* **2017,** *139* (20), 7020-7029.

16. Jin, S.; Son, H.-J.; Farha, O. K.; Wiederrecht, G. P.; Hupp, J. T., Energy Transfer from Quantum Dots to Metal-Organic Frameworks for Enhanced Light Harvesting. *J. Am. Chem. Soc.* **2013,** *135* (3), 955-958.

17. So, M. C.; Wiederrecht, G. P.; Mondloch, J. E.; Hupp, J. T.; Farha, O. K., Metal-organic framework materials for light-harvesting and energy transfer. *Chem. Commun. (Cambridge, U. K.)* **2015,** *51* (17), 3501-3510.

18. Wang, C.; Wang, J.-L.; Lin, W., Elucidating Molecular Iridium Water Oxidation Catalysts Using Metal-Organic Frameworks: A Comprehensive Structural, Catalytic, Spectroscopic, and Kinetic Study. *J. Am. Chem. Soc.* **2012,** *134* (48), 19895-19908.

19. Zhang, Z.-M.; Zhang, T.; Wang, C.; Lin, Z.; Long, L.-S.; Lin, W., Photosensitizing Metal-Organic Framework Enabling Visible-Light-Driven Proton Reduction by a Wells-Dawson-Type Polyoxometalate. *J. Am. Chem. Soc.* **2015,** *137* (9), 3197-3200.

20. Yang, S.; Lin, X.; Blake, A. J.; Walker, G. S.; Hubberstey, P.; Champness, N. R.; Schroeder, M., Cation-induced kinetic trapping and enhanced hydrogen adsorption in a modulated anionic metal-organic framework. *Nat. Chem.* **2009,** *1* (6), 487-493, S487/1-S487/20.

21. Sun, C.-Y.; Wang, X.-L.; Zhang, X.; Qin, C.; Li, P.; Su, Z.-M.; Zhu, D.-X.; Shan, G.-G.; Shao, K.-Z.; Wu, H.; Li, J., Efficient and tunable white-light emission of metal-organic frameworks by iridium-complex encapsulation. *Nat. Commun.* **2013,** *4*, 3717/1-3717/8.

22. Thompson, D. W.; Fleming, C. N.; Myron, B. D.; Meyer, T. J., Rigid medium stabilization of metal-to-ligand charge transfer excited states. *J. Phys. Chem. B* **2007,** *111* (24), 6930-6941.

23. Borfecchia, E.; Garino, C.; Salassa, L.; Ruiu, T.; Gianolio, D.; Zhang, X.; Attenkofer, K.; Chen, L. X.; Gobetto, R.; Sadler, P. J.; Lamberti, C., X-ray transient absorption structural characterization of the 3MLCT triplet excited state of cis-[Ru(bpy)2(py)2]2+. *Dalton Trans.* **2013,** *42* (18), 6564-6571.

24. Sato, T.; Nozawa, S.; Tomita, A.; Hoshino, M.; Koshihara, S.-y.; Fujii, H.; Adachi, S.-i., Coordination and Electronic Structure of Ruthenium(II)-tris-2,2'-bipyridine in the Triplet

Metal-to-Ligand Charge-Transfer Excited State Observed by Picosecond Time-Resolved Ru K-Edge XAFS. *J. Phys. Chem. C* **2012,** *116* (27), 14232-14236.

25. Hitchcock, P. B.; Seddon, K. R.; Turp, J. E.; Yousif, Y. Z.; Zora, J. A.; Constable, E. C.; Wernberg, O., Cis-Bis(2,2'-bipyridine)bis(pyridine)ruthenium(II) salts: a spectroscopic and structural study. *J. Chem. Soc., Dalton Trans.* **1988,** (7), 1837-42.

CHAPTER 5

Cobalt Terpyridine Metal-Organic Layers as a Source for Ultra-Small Cobalt Nanoparticles Active for Proton Reduction in Acidic Media

5.1 Introduction

Efficient hydrogen evolution through electrolysis is a promising solution for sustainable energy production.[1, 2] Cheap catalysts with fast reaction kinetics and long-term stability are required for the industrial implementation of hydrogen production. Historically, platinum-based catalysts are among the state-of-the-art catalysts for hydrogen evolution reaction (HER) and one of a few materials to meet these requirements.[3, 4] However, the scarcity of platinum in the Earth's crust prohibits industrial scale hydrogen production. Hence, the development of novel catalysts based on earth-abundant metals such as Fe[5], Co[6], Ni[7], and Mo[8] or metal-free catalysts[9] have gathered intensive research interests in recent years.

Progress in electrocatalytic HER has been reported for a variety of nanoparticle systems consisting of earth-abundant metals in aqueous solutions.[10-13] Of particular interest was the work of Artero[14, 15] as well as Saveant[16], who showed that cobalt nanoparticles active for hydrogen evolution at modest overpotentials can be synthesized directly from cobalt salts or compounds in the presence of acids. These nanoparticles show modest onset potentials, respectable current densities, and good stability during the HER reaction. It was our group's hope to stabilize ultra-small nanoparticles through the use of sigma-donating complexes to improve the efficiency and atom economy of the HER reaction.

Our group recently pioneered a new class of 2-D metal-organic frameworks referred to as metal-organic layers (MOLs). The metal-organic layers utilized in this paper are comprised of 4'-(4-carboxyphenyl)-[2,2':6',2"-terpyridin]-4'-yl)-5,5"-dicarboxylic acid (H_3TPY) ligands and

hafnium SBUs of the formula [$Hf_6(u_3\text{-}O)(u_3\text{-}OH)(carboxylate)_6(formate)_6$].[17] The capping of the SBU with formic acid along the triangular faces of the octahedral SBU allows for the terpyridine ligand to attach along the same equatorial plane necessary to impart a two-dimensional structure. Furthermore, the strong Lewis-acid Lewis-base interaction between the carboxylates of the terpyridine ligand and the Hf(IV) atoms results in an aqueous stable framework necessary for aqueous proton reduction. The MOL structure lends itself nicely to electrocatalysis unlike traditional MOFs. Their 2-D nature results in a high surface energy which can be passivated through the interaction to the electrode surface, placing all the catalytically relevant sites within close proximity to the electrode surface and improving atom efficiency.

Cobalt terpyridine complexes have previously been shown to be active for proton reduction.[18, 19] However, all of these examples require multiple chelating ligands or polymer films necessary to stabilize the labile cobalt atom and are limited by poor solubility in aqueous environments. We hoped to take advantage of the labile nature of the cobalt center within mono-terpyridine compounds to form cobalt nanoparticles active for proton reduction. By constructing a cobalt terpyridine MOL support passively tethered to an electrode surface, we hoped to promote reduction of the metal to form cobalt nanoparticles. It is our hope that the MOL matrix can limit nanoparticle diffusion away from the electrode surface, via sigma bonding interactions and sterics, therby forming ultra-small cobalt nanoparticles active for the HER at sufficiently reductive potentials.

5.2 Results and Discussion

5.2.1 Material Characterization

Unmetalated TPY MOL was prepared by dissolving H_3TPY and $HfCl_4$ in DMF with trace amounts of water and formic acid and subsequently heating the mixture at 120 ˚C for three days. The MOL was then cleaned and metalated with $Co(NO)_3$ in DMF at 60 ˚C overnight to yield the MOL CoTPY. Both the TPY and CoTPY MOL samples show identical PXRD patterns in agreement with literature precedent,[17] with the two diffraction peaks at 5.27 and 8.71 2θ representing the 10 and 11 diffraction peaks of the MOL (Figure 5-1). The morphology of CoTPY was further analyzed with TEM (Figure 5-2) and shows large thin crystalline sheets with sizes ranging from 100-500 nm with high degree of ribboning and agglomeration due to the high surface energy of the 2-D surface. AFM images (Figure 5-3) of the species showed the MOL thickness to be 1.2 nm, corresponding well with the height of the theoretical model of the Hf_6 SBU, confirming the two-dimensional structure of CoTPY. To confirm the uptake of cobalt into TPY, UV-VS spectroscopy was employed. A color change from grey to green is observed after metalation with cobalt nitrate due to the emergence of a metal-to-ligand charge transfer band that can be directly observed at 345 nm (Figure 5-4).

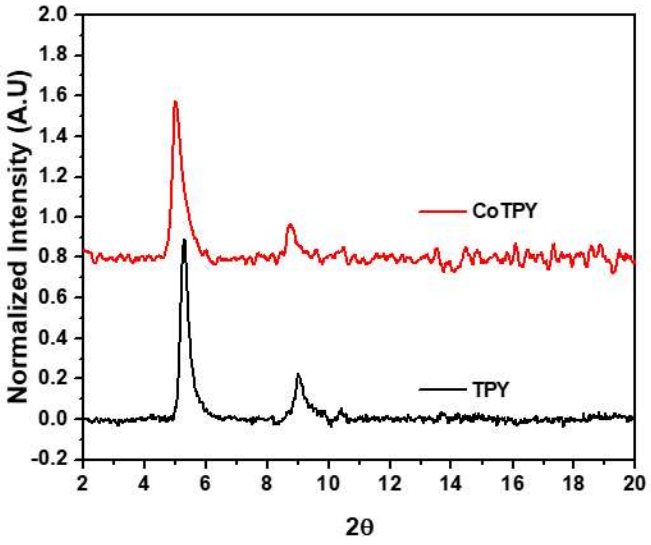

Figure 5-1. The PXRD spectra of the TPY-MOL both with (red) and without (black) incorporation of cobalt.

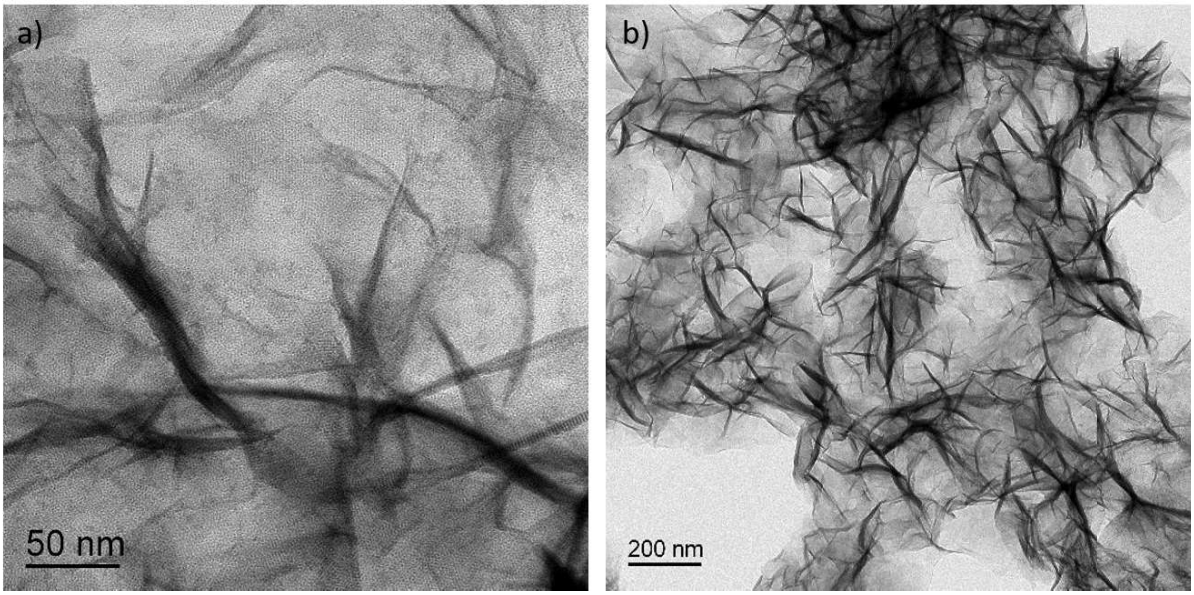

Figure 5-2. TEM images of CoTPY after synthesis.

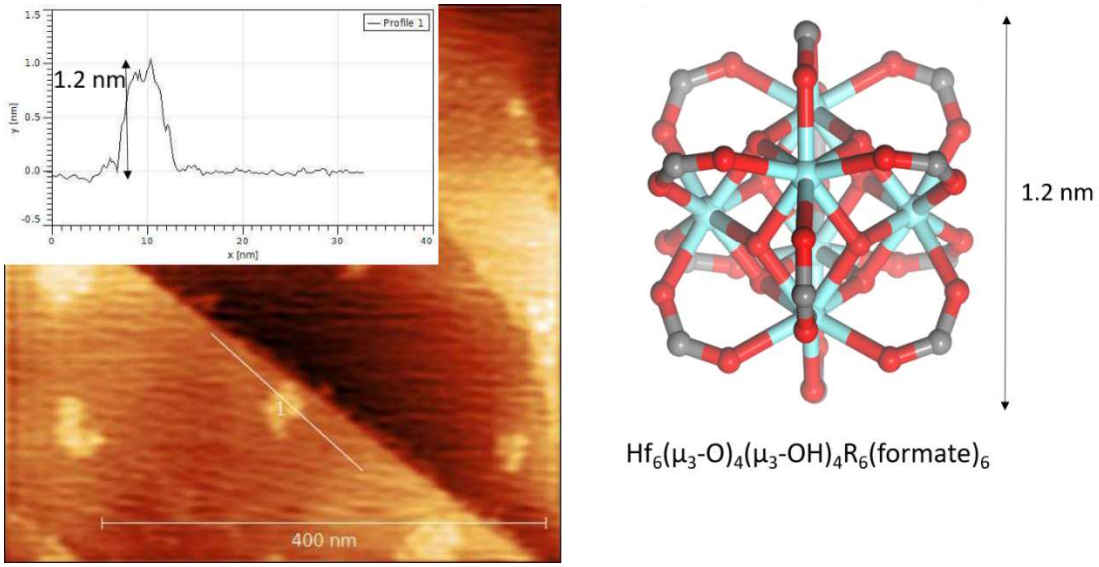

Figure 5-3. AFM images (left) reveal CoTPY to be made up of 1.2 nm tall sheets in agreement with the theoretical height of a single the Hf_6 SBU (right).

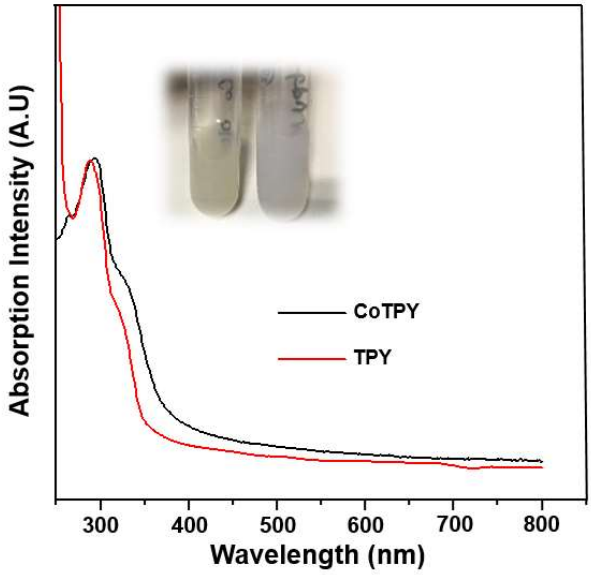

Figure 5-4. The UV-VIS spectra of TPY (Red) and CoTPY (black) in DMF. A picture of the two dispersions (left = CoTPY, right = TPY) clearly shows a color change indicative of metalation (inlay).

5.2.2 Electrochemical Results

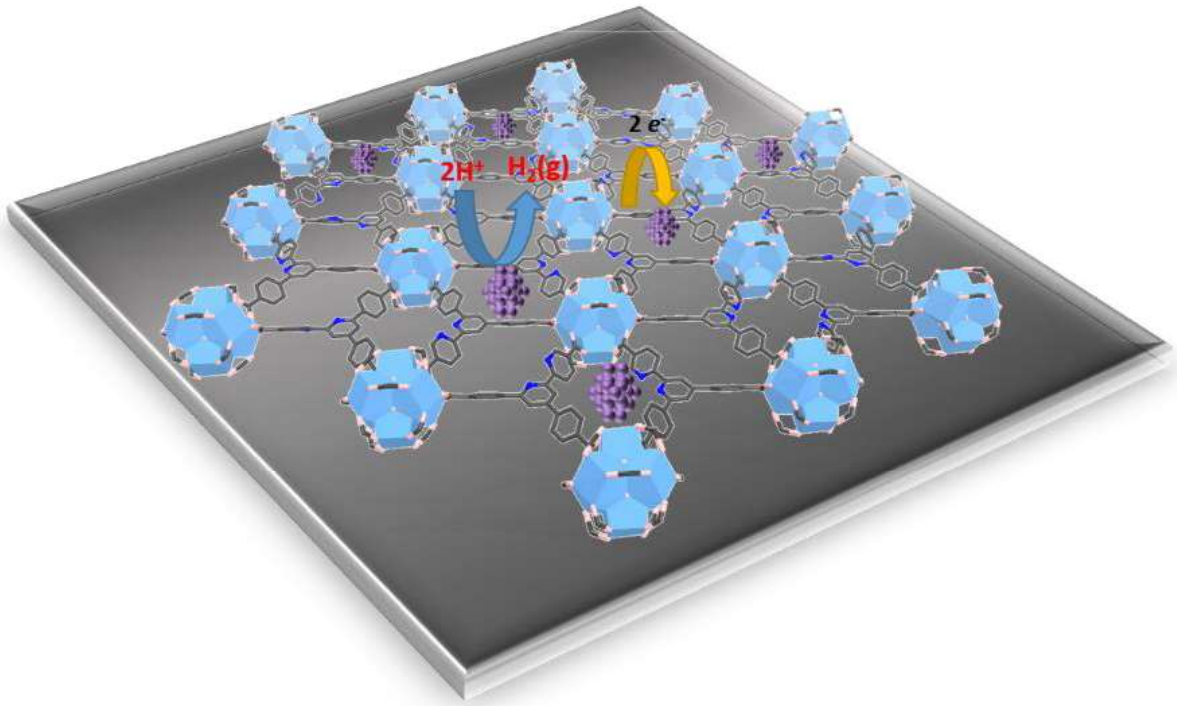

Scheme 5-1. The representation of the TPY MOL trapping cobalt nanoparticles to carry out proton reduction. Colors: Teal - Hafnium, Pink - Oxygen, Blue - Nitrogen, Grey- Carbon, Purple - Cobalt.

To carry out electrochemical experiments, the MOL was dropcasted onto a 1.5 cm^2 glassy carbon electrode and spincoated at 3000 RPM. The average cobalt loading was quantified via ICP-MS and found to be 14.5 nmol. This correlates with 134.4 layers of MOL assuming complete surface coverage and 75% cobalt metalation for each terpyridine.

Initially the MOL system shows limited activity for proton reduction, showing minimal improvement when placed over a pristine glassy carbon electrode. However, the material activates when subjected to a continuous negative potential in acidic media (Figure 5-5). For our experiments, all MOL samples were activated at -1.0 V vs. the Ag/AgCl electrode for fifteen minutes in pH 1 $HClO_4$ (*aq*). This activation procedure results in a significant increase in current

density as well as a decrease in the onset potential of over 200 mV for proton reduction in acidic media, corresponding to a Tafel slope as low as 195 mv/decade. The observed increase in current density and decrease in overpotential after activation are robust and persist even after washing the electrode surface (Figure 5-6). The activation is likely the formation of cobalt nanoparticles. Cobalt ions reduced in the presence of an acid have previously been demonstrated to be effective HER catalysts.[14, 16] Furthermore, the inherent lability of first row transition metals bound to terpyridine moieties in acidic environments provides an abundant cobalt source for cobalt nanoparticle formation. Comparison of CV traces before and after activation also show a loss of a reductive peak at -0.57 V vs. NHE (Figure 5-6). This peak coincides with the Co(II/I) reduction potential of cobalt terpyridine species observed in our studies as well as reported in the literature,[20] directly supporting the assertion that the cobalt atom is no longer coordinated to the terpyridine ligands. With neither the glassy carbon electrode nor the terpyridine ligand demonstrated to be effective proton reductive catalysts (the first reduction potential of terpyridine is -1.45 V vs. NHE), it can be inferred that nanoparticle formation from the reduction of ions is the only possible source of activity. Hf nanoparticle formation was ruled out from ICP-MS studies as only 0.7% of the Hf in the MOL sample was found to have leached from the MOL sample into solution.

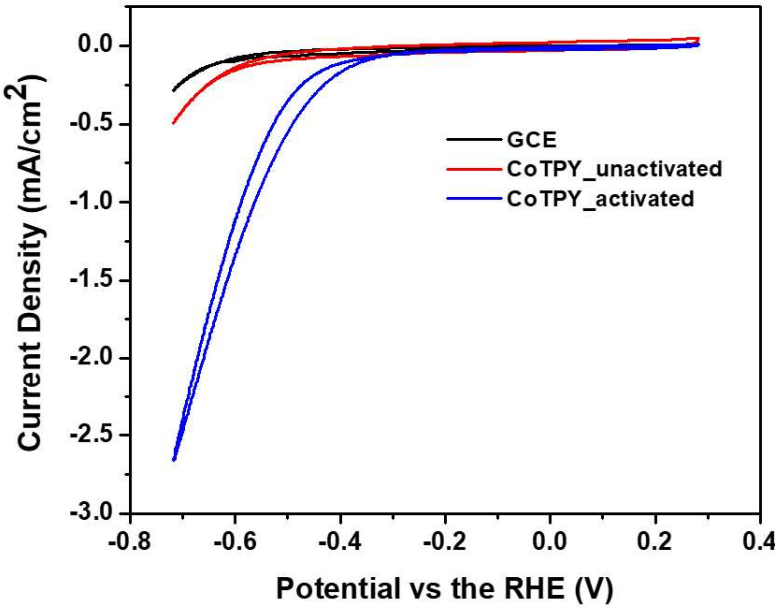

Figure 5-5. The CV traces of the CoTPY MOL both before (red) and after (blue) bulk electrolysis at η = 715 mV in pH 1 perchloric acid.

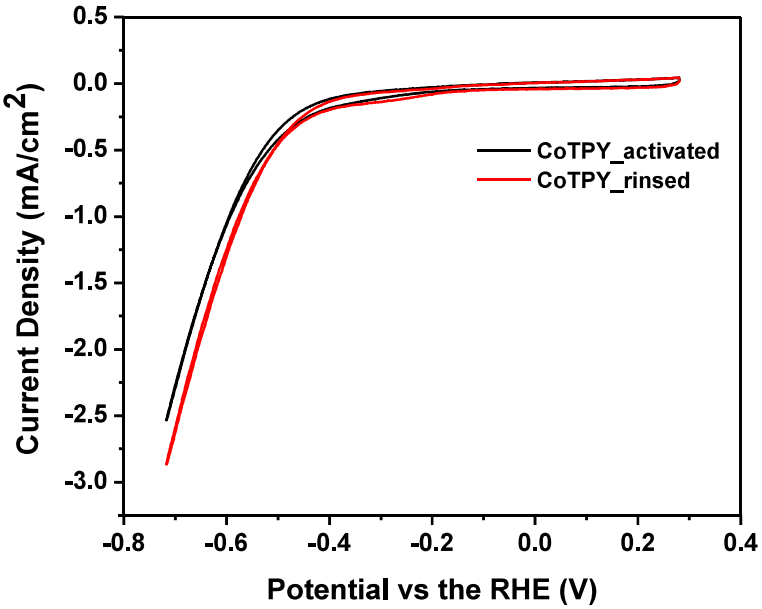

Figure 5-6. The rinse test of activated CoTPY in pH 1 perchloric acid.

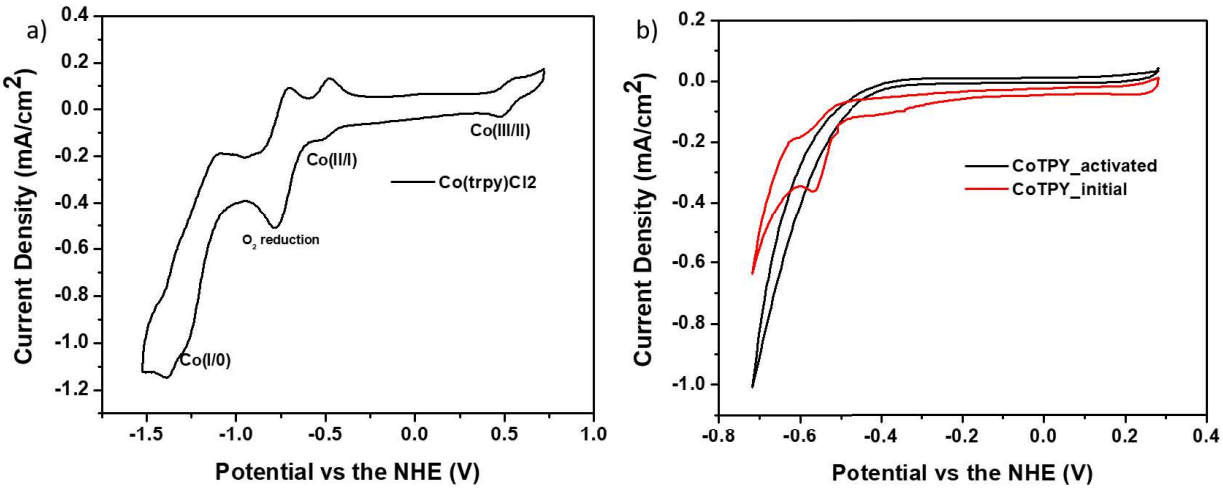

Figure 5-7. a) The CV trace of the $Co(tpy)Cl_2$ in ACN with 0.1 M $TBAPF_6$ as an electrolyte. B) The Co(II/I) reduction peak disappears after the CoTPY material is subjected to 715 mV overpotential vs the RHE for 15 minutes.

Bulk electrolysis reactions of CoTPY were performed in a U-shaped cell with a teflon membrane separating the anodic and oxidative half reactions. Cathodic proton reduction was carried out on a glassy carbon electron which was spincoated with CoTPY MOL at 3000 rpm and allowed to dry prior. Electrochemical analysis was performed with 0.1 M degassed $HClO_4$ (aq) solution against an Ag/AgCl electrode with a glassy carbon counter electrode unless stated otherwise. Both half reactions were subjected to stirring at 400 rpm under a nitrogen atmosphere.

The activated material showed an impressive efficiency for hydrogen production during bulk electrolysis in acidic conditions. Turnover frequencies (TOF) of up to 4300 hr^{-1} were recorded at an overpotential of 715 mV while TOFs of up to 450 hr^{-1} occur at the more modest overpotential of 515mV in pH 1 perchloric acid. Both of these values coincide with Faradaic efficiencies of over 93%. The activated sample retains good efficacy over time with near 100% Faradaic efficiency observed for at least one half hour of electrolysis at 715 mV or 515 mV overpotential (Figure 5-8, Table 5-1). However, as electrolysis continues, there is an associated drop off in TOF and Faradaic

efficiency. This is likely a result of a loss of cobalt nanoparticles from the surface of the electrode leading to the direct reduction of the terpyridine ligand, SBU, or other impurities. After one hour of electrolysis, it was found that up to 63 % of the available cobalt leaches into solution during electrocatalytic conditions via ICP-MS analysis.

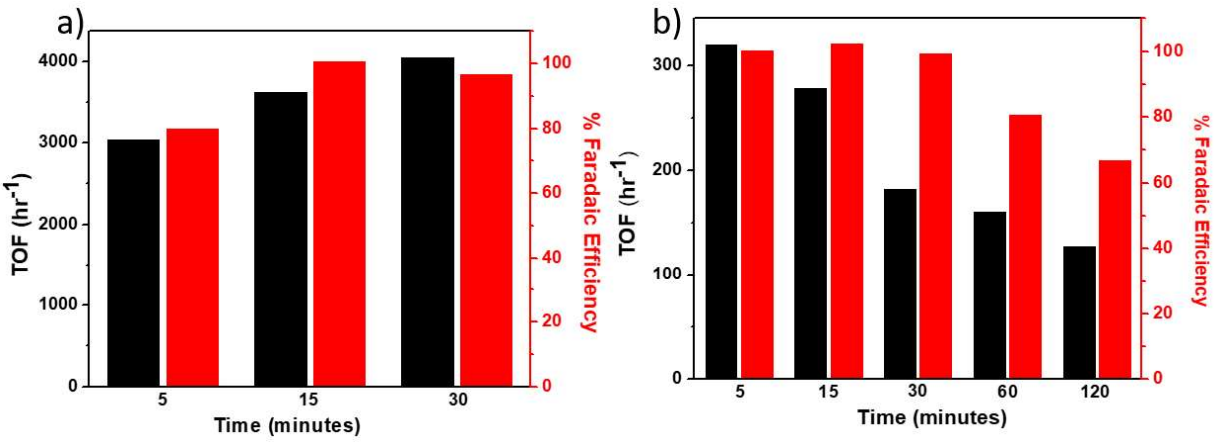

Figure 5-8. The TOF (based on Co atoms) and Faradaic Efficiency of CoTPY at different time points at a) 715 mV and b) 515 mV overpotential vs the RHE in pH 1 perchloric acid.

Table 5-1. The average bulk electrolysis results of CoTPY in pH 1 perchloric acid.

Potential vs NHE (V)	Average TOF (hr^{-1})	Average % F.E
715	2567	93.62
515	383	97.79

The high activity for proton reduction makes the CoTPY system an attractive material to carry out total water splitting. When coupled with a Pt counter electrode, the system is capable of complete water splitting at an overpotential of 715 mV with near 100% Faradaic Efficiency at the platinum anode and 84% F.E at the CoTPY/GCE cathode, (Figure 5.9) correlating to a TOF of 2135 hr^{-1}.

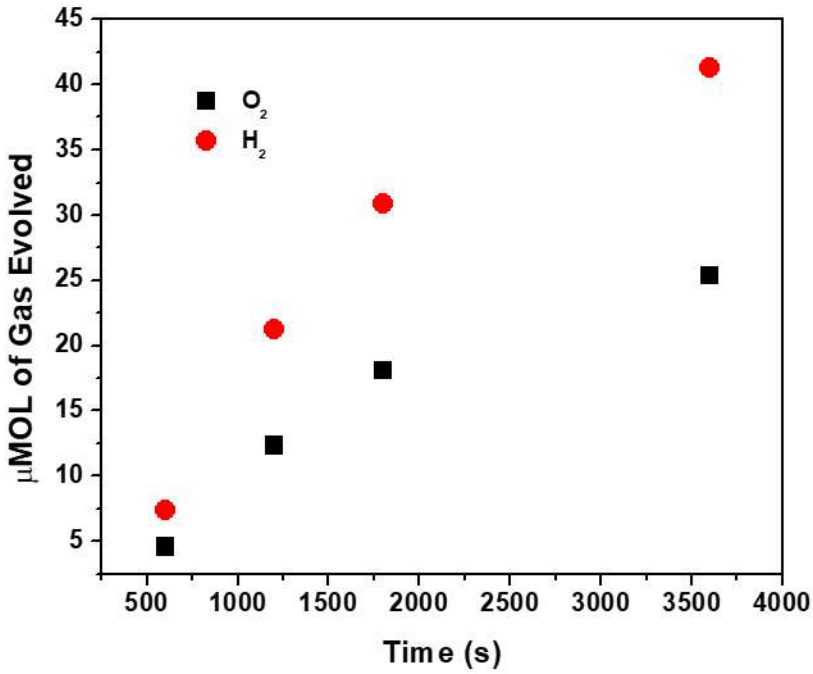

Figure 5-9. Hydrogen and oxygen production from the CoTYP/GCE cathode and Pt anode in pH 1 perchlooric acid at η = 715 mV.

At an overpotential of 715 mV, the CoTPY MOL system vastly outperforms its homogenous analogs. The $Co(trpy)Cl_2$ system obtains a TOF of 24.2 hr^{-1} (as determined by foot of the wave analysis) with a Faradaic Efficiency of 76%. Like the homogenous analogue, the unmetalated TPY MOL shows hydrogen production, likely from the reduction of trace ions in solution, of about a third of that of the cobalt metalated species with a Faradaic efficiency of 73% at 715 mV of overpotential (Figure 5-10). When $CoCl_2$ salts are placed under the same bulk electrolysis conditions as our MOL sample, a similar activation, onset potential, and current density are seen, indicating nanoparticle formation. However, the MOL samples outperform the cobalt nanoparticles consistently, even at significantly higher cobalt concentrations (Table 5-2). We hypothesize that ultra-small cobalt clusters are being formed on the surface of the electrode due to the low molarity of cobalt on the surface (about 10nmol) coupled with the strong donating effects

of the imine groups in terpyridine and the steric effects of the MOL. This provides not only more surface area for catalysis but also leads to higher energy surfaces and faster kinetics as the trapped nanoparticles in CoTPY are not limited by diffusion.

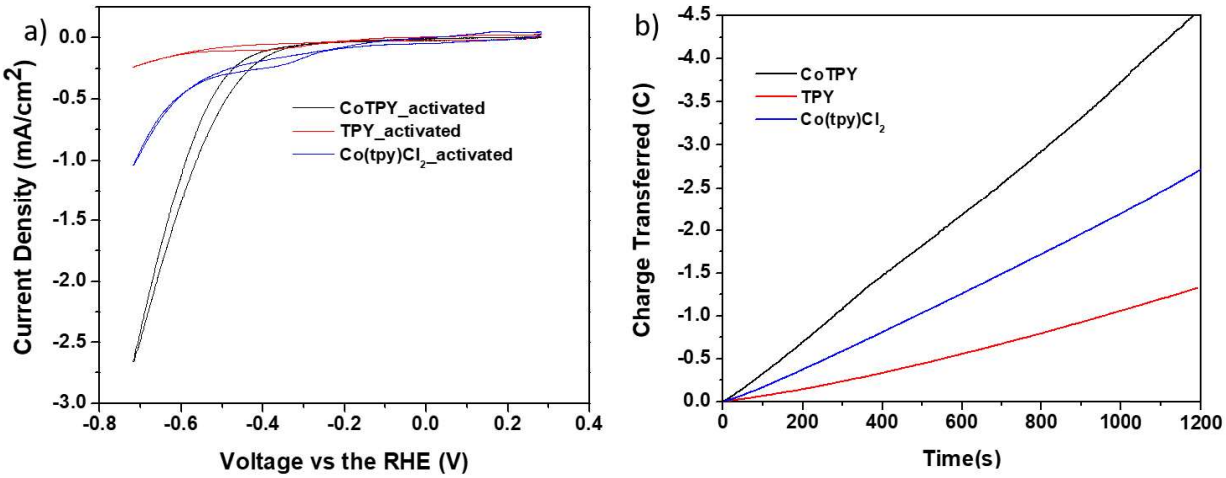

Figure 5-10. a) The CV traces of the activated CoTPY and its controls in pH 1 perchloric acid. b) The bulk electrolysis results of CoTPY and its controls in pH 1 perchloric acid at η = 715 mV.

Table 5-2. The HER results of CoTPY versus its controls in pH 1 perchloric acid after 30 minutes of bulk electrolysis at η = 715 mV.

Sample	Co Concentration (ppb)*	μMOL H_2	Charge (C)	%F.E
$Co(NO_3)_2$	200	6.51	1.59	79.05
$Co(NO_3)_2$	5000	6.15	1.48	79.93
$Co(NO_3)_2$	59000	8.57	1.89	87.43
GCE	0	4.60	1.5	59.39
Co(tpy) $(NO_3)_2$	59000	9.67	2.46	75.98
Co(tpy) $(NO_3)_2$	59000	0.57	1.21	9.13
CoTPY	142	14.43	2.91	95.57

*Concentration of the CoTPY sample was based on the total amount of cobalt on the surface of the electrode.

Evidence for nanoparticle formation is observed from a series of spectroscopic, electrochemical, and imaging techniques. The IR spectra of the MOL structure before and after electrolysis shows

a discrepancy with a peak at 1110 cm^{-1} only not-observed in the inactive species. This peak is also present in the TPY MOL system prior to metalation and is representative of C-N stretching within the terpyridine molecule, which is slightly perturbed as a result of the effective mass of the bound cobalt center in the inactive sample (Figure 5-11a). The presence of nanoparticles is also indirectly supported by the loss of measured current density upon the addition of mercury to the CoTPY/GCE cathode in an attempt to poison the nanoparticles (Figure 5-11b). Nanoparticle formation in the CoTPY system was directly observed under reaction conditions in which the loading of CoTPY was increased by one-thousand times and bulk electrolysis was run. When TEM images of the CoTPY suspension were taken after electrolysis in comparison to those of $Co(NO_3)_2$, uniformly distributed 5 nm cobalt nanoparticles trapped in the MOL matrix were observed (Figure 5-12). The homogenous sample however, had fewer observed nanoparticles with non-uniform sizes and shapes ranging from 5 nm to 20 nm (Figure 5-12b).

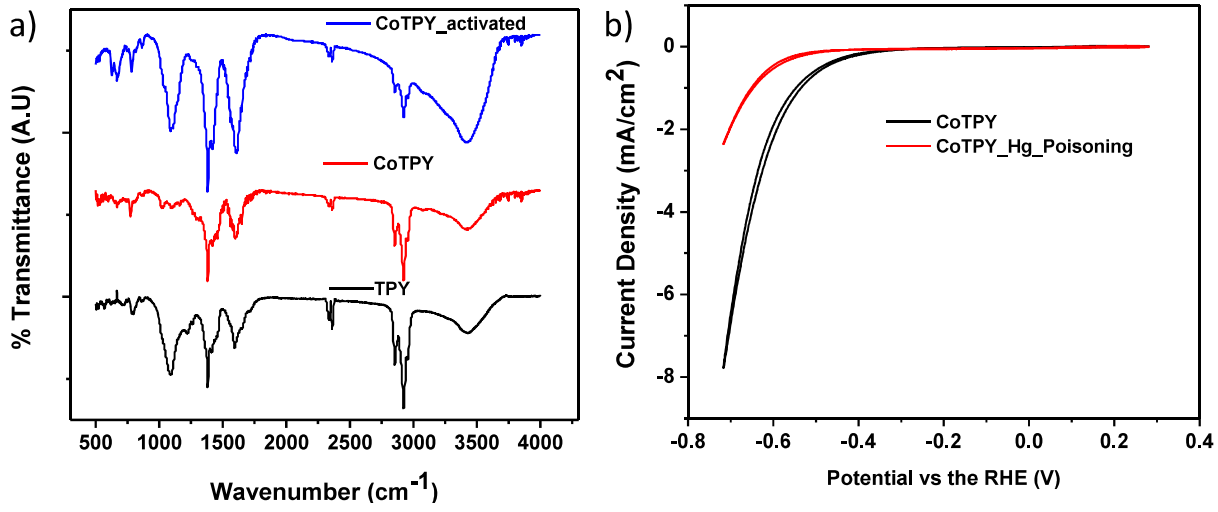

Figure 5-11. a) The FTIR spectra of unactivated CoTPY, unactivated TPY, and activated CoTPY b) The mercury poisoning experiment of the CoTPY electrode surface in pH 1 perchloric acid compared to the activated material prior to the addition of mercury.

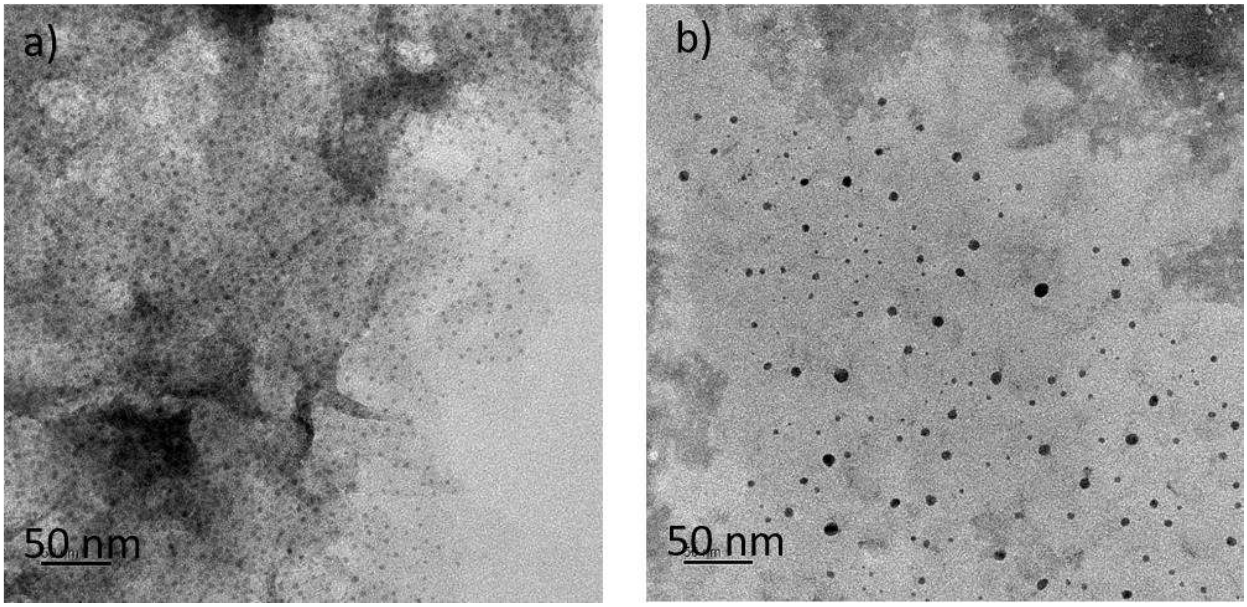

Figure 5-12. a) TEM images of highly concentrated CoTPY (0.1 mM w.r.t. Co) shows that the cobalt centers are reduced down into uniform nanoparticles within the MOL matrix at a reducing potential of η = 715 mV in perchloric acid. b) The TEM image of 0.1 mM $Co(NO_3)_2$ shows fewer nanoparticles of highly variable size and shape within the suspension upon reduction at the same conditions.

Because of the facile growth of the nanoparticle assembly, we decided to test the efficacy of other metal centers within the MOL, specifically iron. Being slightly more electron deficient than cobalt, iron-terpyridine (FeTPY) is more stable in acidic environments than cobalt, however, both are nearly completely demetalated at pH 1 as determined from ICP-MS. The iron sample shows similar onset potential and activation behavior relative to CoTPY but shows worse activity. This behavior is seen in both the CV traces as well as in the bulk electrolysis results. The iron sample produced half as much hydrogen as the cobalt species at η = 715 mV and had a Faradaic Efficiency of 64%. The drop in Faradaic Efficiency was hypothesized to result from direct reduction of the perchlorate iron by chlorine, as iron nanoparticles have been previously shown to be active for this reduction.[21]

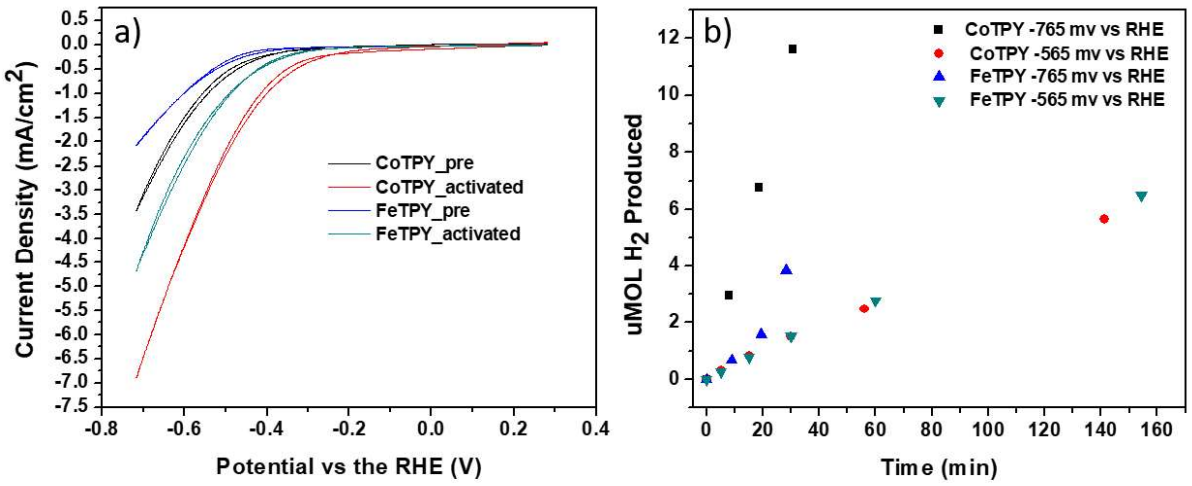

Figure 5-13. a) The CV traces of CoTPY compared to that of FeTPY in pH 1 perchloric acid before and after activation. b) The HER results of bulk electrolysis for CoTPY and FeTPY at varying overpotentials in pH 1 perchloric acid.

5.3 Conclusion

The use of MOLs as electrocatalysts opens new avenues for the classes and subclasses of metal-organic frameworks. The CoTPY was shown to be an effective cobalt source for nanoparticle formation as well as an effective membrane to confine, both sterically and through weak chemical interactions, the nanoparticles in close proximity to the electrode surface while simultaneously preventing aggregation. As a result, we were able to obtain a water- and air-stable cobalt catalyst capable of fast proton reduction at moderate over potentials that outperforms its homogenous counterparts and unmetalated heterogeneous counterparts.

5.4 Methodologies

5.4.1 Electrochemical Methods:

All electrochemical experiments were performed using a Pine Instruments WaveDriver potentiostat (Model AFP2). Non-catalytic experimental techniques were performed in acetonitrile degassed with nitrogen for at least thirty minutes with 0.1 M $TBAPF_6$ serving as the electrolyte.

Aqueous experiments were performed in pH 1 perchloric acid solution degassed with nitrogen for at least thirty minutes. If the pH was increased, the electrolyte concentration was maintained at 0.1 $[ClO_4]^-$ using potassium perchlorate. Cyclic voltammetry (CV) measurements were performed in a standard three-electrode cell with a glassy carbon electrode (0.4 cm diameter) serving as the working electrode, silver chloride serving as the reference electrode (Calculated at 0.223 V vs NHE from the $Fe(CN)_6$ redox couple), and a GCE counter electrode. Scan rates were collected at 100 mV s^{-1} unless stated otherwise and all experiments were collected underneath a nitrogen atmosphere. Controlled potential electrolysis was performed in the same setup as the CV except the solution was stirred at 400 RPM to prevent bubbles from obscuring the working electrode surface.

5.4.2 GC Quantification:

All gas chromatography (GC) measurements were obtained using an Agilent 7890B GC system. 300 µL of headspace (measured to be 177 mL) of the reaction vessel was injected post controlled potential electrolysis.

5.4.3 ICP-MS Characterization:

ICP-MS data was obtained with an Agilent 7700x ICP-MS and analyzed using ICP-MS MassHunter version B01.03. Samples were diluted in a 2% HNO_3 matrix and analyzed with a ^{159}Tb internal standard against a 12-point standard curve over the range from 0.1 ppb to 500 ppb. The correlation was >0.9997 for all analyses of interest. Data collection was performed in Spectrum Mode with five replicates per sample and 100 sweeps per replicate.

5.5 Synthetic Procedures

5.5.1 Synthesis of Ligands

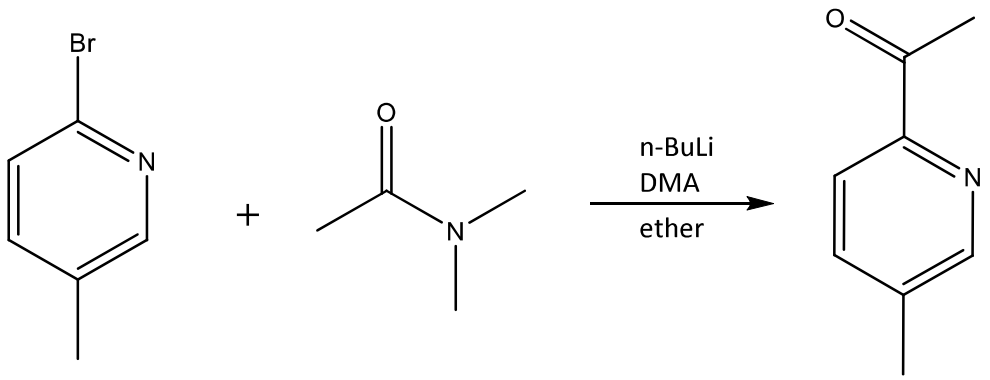

Scheme 5-2. The synthesis of 1-(5-methylpyridin-2-yl)ethanone

Synthesis of -(5-methylpyridin-2-yl)ethanone: 2-bromo-5-methylpyridine (8.60 g, 50.0mmmol) was dissolved in 100 mL of dry diethyl ether and cooled to -78 ˚C. n-Butyl lithium (20 mL, 2.5 M in hexane) was added dropwise over 30 minutes and subsequently stirred for 90 minutes. Dimethylacetamide (DMA, 5mL) was then added dropwise and the solution was stirred for another three hours until it was quenched with saturated NH_4Cl (*aq*). Extraction of the aqueous layer with ether was then performed and all organic parts were combined, dried with anhydrous sodium sulfate, and filtered. After evaporation of the solvent, the crude product was subjected to column chorography on silica gel (10:90 EtOAC/CH_2Cl_2 as eluent) to afford the product (4.86 g, 36.0 mmol, 72% yield) as a transparent oil. ^{1}HNMR (500 MHz, $CDCl_3$): 8.50 (s, 1H), 7.95 (d, 1H), 6.21 (m, 1H), 2.70 (s, 3H), 2.42 (s, 3H).

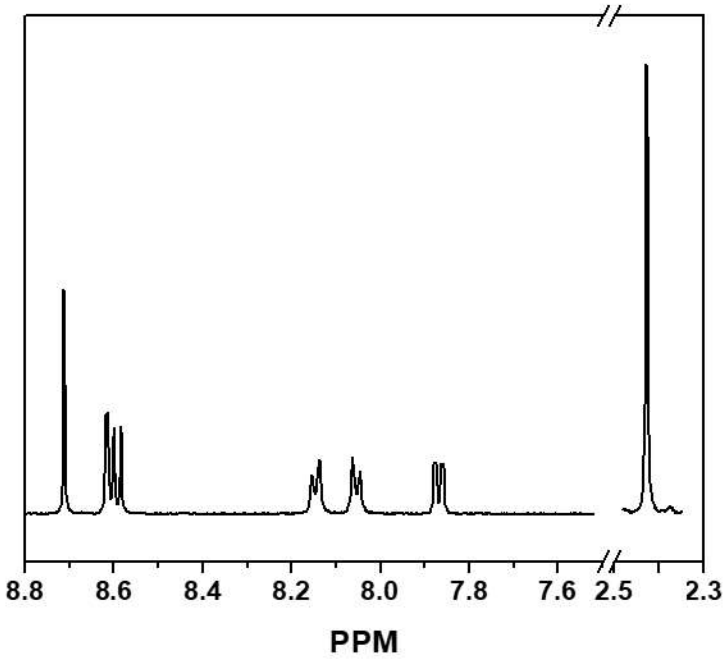

Figure 5-14. The ^{1}H-NMR of 4-(5,5”-dimethyl-[2,2’:6’,2”-terpyridin]-4’-yl)benzoic acid in $(CD_3)_2SO$.

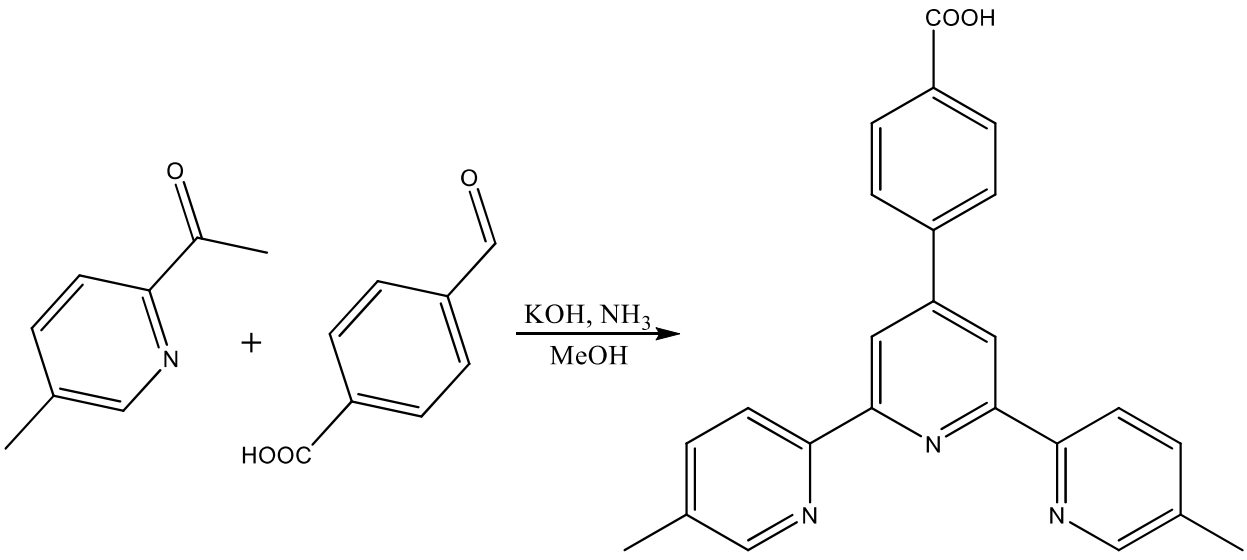

Scheme 5-3. The synthesis of 4-(5,5”-dimethyl-[2,2’:6’,2”-terpyridin]-4’-yl)benzoic acid.

Synthesis of 4-(5,5”-dimethyl-[2,2’:6’,2”-terpyridin]-4’-yl)benzoic acid: 1-(5-methylpyridin-2-yl)ethanone (3.30 g, 24,4 mmol) and 4-carboxylbenzaldehyde (1.83g, 12.2

mmol) were dissolved in MeOH (100mL) followed by the addition of 15% KOH (*aq*) (110 mL) and ammonium hydroxide (12.2 mL). The mixture was stirred at room temperature for three days. The white precipitate was separated via vacuum filtration and washed with chloroform multiple times and subsequently dissolved in MeOH:H_2O (1:1). 1M HCl was added dropwise until the solution was at pH 3 to afford a white precipitate, which was collected by filtration and washed with water to yield the product (3.26 g, 17.1 mmol 70 % yield). ^{1}HNMR (500 MHz, $(CD_3)_2SO$): 8.71 (s, 2H), 8.60 (m, 4H), 8.15 (d, 2H), 8.05 (d, 2H), 7.87 (d, 2H) and 2.43 (s, 6H). Note, it is imperative to remove all traces of metals, particularly iron, from glassware, stirring bar, and solutions.

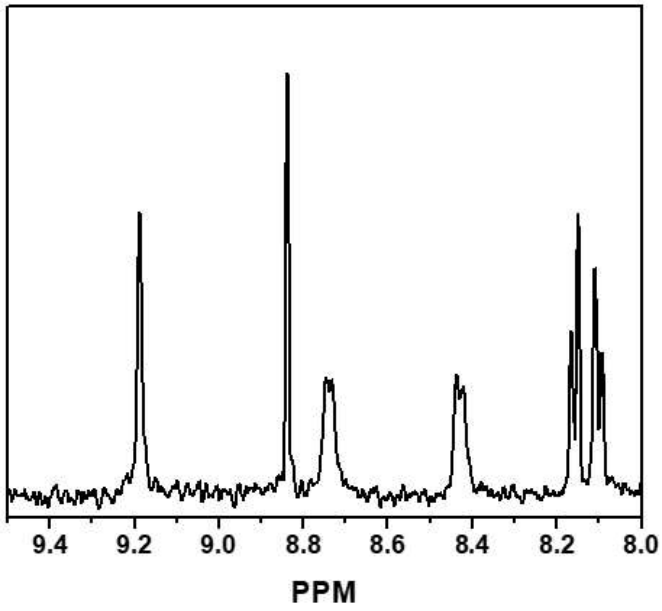

Figure 5-15. The ^{1}H-NMR of H_3TPY in $(CD_3)_2SO$.

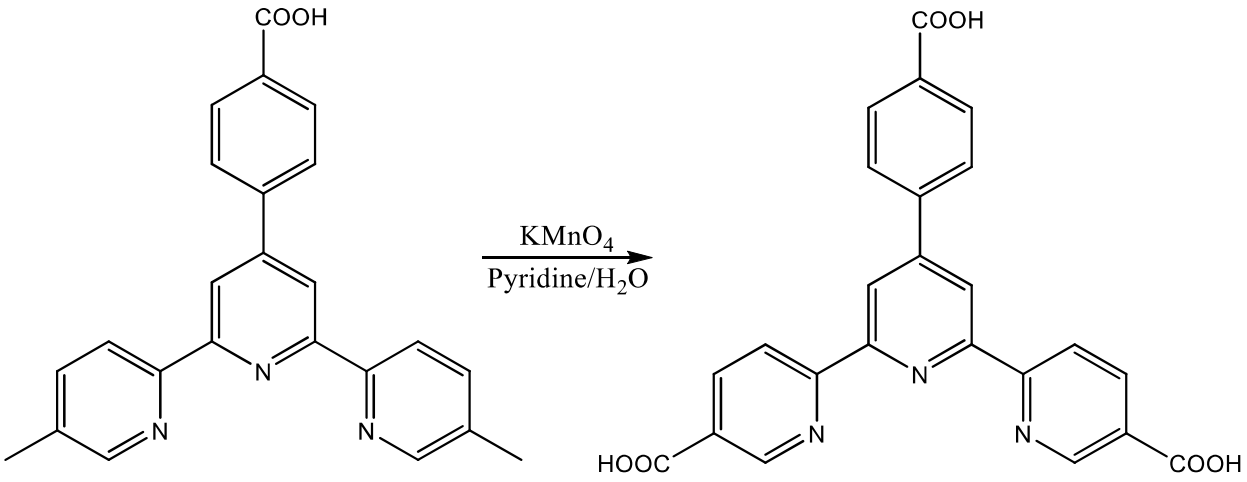

Scheme 5-4. Synthesis of 4'-(4-carboxyphenyl)-[2,2':6',2"-terpyridin]-4'-yl)-5,5"-dicarboxylic acid (H_3TPY).

Synthesis of H_3TPY: 4-(5,5"-dimethyl-[2,2':6',2"-terpyridin]-4'-yl)benzoic acid (1.00 g, 2.62 mmoll) was dissolved in pyridine:H_2O (3:1, 80 mL) followed by the addition of $KMnO_4$, (5.00g, 31.6 mmol). The reaction was heated to 100 ˚C and refluxed overnight. Additional $KMnO_4$, (2.50g, 15.8 mmol) was added into the reaction mixture and the solution was refluxed for another day to ensure complete oxidation. The solution was then cooled to room temperature, diluted with ethanol, and filtered. The filtrate was dried under rotary evaporation and dissolved in 1 M HCl until the solution was pH 3. The white precipitate was collected via filtration, washed with deionized water, and dried under vacuum to yield the product (1.04 g, 2.36 mmol, 90% yield). ^{1}HNMR (500 MHz, $(CD_3)_2SO$): 13.42 (br, 3H), 9.28 (s, 2H), 8.83 (s, 2H), 8.74 (d, 2H), 8.43 (m, 2H), 8.16 (d, 2H), and 8.10 (d, 2H).

Synthesis of $Co(tpy)Cl_2$: In the N_2 filled glovebox, a solution of terpyridine (tpy, 10 mg, 42.8umol) in THF (1 mL) was added into the solution of $CoCl_2$ (7.0 mg, 53.9 umol) in THF (2.14 mL) dropwise while being stirred. The stirring continued for 12 hours before the solid product was collected by centrifugation and washed with THF 3 times (90% yield). ESI-MS calculated for $C_{15}H_{12}Cl_2CoN_3O$: 379.0, found: 379.2.

5.5.2 Synthesis of MOLs

Synthesis of TPY-MOL: 12.5 mg of H_3TPY (28.3 μMol, 1 equivalence) and 14 mg $HfCl_4$ (43.8 μMOL, 1.54 equivalent) were dissolved in 10 mL DMF via sonication. After the subsequent addition of 500 μL of water and 750 μL of formic acid, the entire solution was heated at 120 ˚C for two days. The MOL $[Hf_6(u_3\text{-}O)_4(u_3\text{-}OH)_4(HCO_2)_6(TPY)_2]$ was obtained as a light grey solid dispersion in good yield. (~75%)

Synthesis of CoTPY MOL: $Co(NO_3)_2{\cdot}6H_2O$ (10.3 μMOL, 3 equivalents w.r.t. TPY) was dissolved in TPY/DMF suspension (4 mg/2mL, 1 equivalent based on TPY) under sonication and then heated at 60 ℃ for 12 hours. The product was washed with DMF to remove the excess Co^{2+} and dispersed in THF before use. The formula of CoTPY is $Hf_6O_4(OH)_4(HCO_2)_6]tpy_2Co_{1.7}$ determined by ICP-MS (~95%).

Synthesis of FeTPY MOL: $FeCl_3$ (10.3 μMOL, 3 equivalents w.r.t. TPY) was dissolved in TPY/DMF suspension (4 mg/2mL, 1 equivalent w.r.t. TPY) under sonication and then heated at 60 ℃ for 12 hours. The product was washed with DMF to remove the excess Fe^{3+} and dispersed in THF before use. The formula of FeTPY is $Hf_6O_4(OH)_4(HCO_2)_6]tpy_2Fe_{1.7}$ determined by ICP-MS (~95%).

5.5 References

1. Concepcion, J. J.; House, R. L.; Papanikolas, J. M.; Meyer, T. J., Chemical approaches to artificial photosynthesis. *Proceedings of the National Academy of Sciences* **2012,** *109* (39), 15560-15564.

2. Lewis, N. S.; Nocera, D. G., Powering the planet: Chemical challenges in solar energy utilization. *Proceedings of the National Academy of Sciences* **2006,** *103* (43), 15729-15735.

3. Conway, B.; Tilak, B., Interfacial processes involving electrocatalytic evolution and oxidation of H2, and the role of chemisorbed H. *Electrochimica Acta* **2002,** *47* (22), 3571-3594.

4. Wang, C.; deKrafft, K. E.; Lin, W., Pt nanoparticles@ photoactive metal–organic frameworks: efficient hydrogen evolution via synergistic photoexcitation and electron injection. *Journal of the American Chemical Society* **2012,** *134* (17), 7211-7214.

5. Becker, R.; Amirjalayer, S.; Li, P.; Woutersen, S.; Reek, J. N. H., An iron-iron hydrogenase mimic with appended electron reservoir for efficient proton reduction in aqueous media. *Science Advances* **2016,** *2* (1).

6. Jin, H.; Wang, J.; Su, D.; Wei, Z.; Pang, Z.; Wang, Y., In situ cobalt–cobalt oxide/N-doped carbon hybrids as superior bifunctional electrocatalysts for hydrogen and oxygen evolution. *J. Am. Chem. Soc* **2015,** *137* (7), 2688-2694.

7. Han, Y.; Fang, H.; Jing, H.; Sun, H.; Lei, H.; Lai, W.; Cao, R., Singly versus Doubly Reduced Nickel Porphyrins for Proton Reduction: Experimental and Theoretical Evidence for a Homolytic Hydrogen-Evolution Reaction. *Angewandte Chemie* **2016,** *128* (18), 5547-5552.

8. Jin, Y.; Wang, H.; Li, J.; Yue, X.; Han, Y.; Shen, P. K.; Cui, Y., Porous MoO2 Nanosheets as Non-noble Bifunctional Electrocatalysts for Overall Water Splitting. *Advanced Materials* **2016,** *28* (19), 3785-3790.

9. Zheng, Y.; Jiao, Y.; Zhu, Y.; Li, L. H.; Han, Y.; Chen, Y.; Du, A.; Jaroniec, M.; Qiao, S. Z., Hydrogen evolution by a metal-free electrocatalyst. *Nature communications* **2014,** *5*, 3783.

10. Kong, D.; Wang, H.; Lu, Z.; Cui, Y., CoSe2 Nanoparticles Grown on Carbon Fiber Paper: An Efficient and Stable Electrocatalyst for Hydrogen Evolution Reaction. *J. Am. Chem. Soc.* **2014,** *136* (13), 4897-4900.

11. Popczun, E. J.; McKone, J. R.; Read, C. G.; Biacchi, A. J.; Wiltrout, A. M.; Lewis, N. S.; Schaak, R. E., Nanostructured Nickel Phosphide as an Electrocatalyst for the Hydrogen Evolution Reaction. *J. Am. Chem. Soc.* **2013,** *135* (25), 9267-9270.

12. Benck, J. D.; Hellstern, T. R.; Kibsgaard, J.; Chakthranont, P.; Jaramillo, T. F., Catalyzing the Hydrogen Evolution Reaction (HER) with Molybdenum Sulfide Nanomaterials. *ACS Catal.* **2014,** *4* (11), 3957-3971.

13. Callejas, J. F.; Read, C. G.; Popczun, E. J.; McEnaney, J. M.; Schaak, R. E., Nanostructured Co2P Electrocatalyst for the Hydrogen Evolution Reaction and Direct Comparison with Morphologically Equivalent CoP. *Chem. Mater.* **2015,** *27* (10), 3769-3774.

14. Andreiadis Eugen, S.; Jacques, P.-A.; Tran Phong, D.; Leyris, A.; Chavarot-Kerlidou, M.; Jousselme, B.; Matheron, M.; Pecaut, J.; Palacin, S.; Fontecave, M.; Artero, V., Molecular engineering of a cobalt-based electrocatalytic nanomaterial for H2 evolution under fully aqueous conditions. *Nat Chem* **2013,** *5* (1), 48-53.

15. Zou, X.; Huang, X.; Goswami, A.; Silva, R.; Sathe, B. R.; Mikmekova, E.; Asefa, T., Cobalt-Embedded Nitrogen-Rich Carbon Nanotubes Efficiently Catalyze Hydrogen Evolution Reaction at All pH Values. *Angew. Chem., Int. Ed.* **2014,** *53* (17), 4372-4376.

16. Anxolabehere-Mallart, E.; Costentin, C.; Fournier, M.; Nowak, S.; Robert, M.; Saveant, J.-M., Boron-Capped Tris(glyoximato) Cobalt Clathrochelate as a Precursor for the Electrodeposition of Nanoparticles Catalyzing H2 Evolution in Water. *J. Am. Chem. Soc.* **2012,** *134* (14), 6104-6107.

17. Lin, Z.; Thacker, N. C.; Sawano, T.; Drake, T.; Ji, P.; Lan, G.; Cao, L.; Liu, S.; Wang, C.; Lin, W., Metal-organic layers stabilize earth-abundant metal-terpyridine diradical complexes for catalytic C-H activation. *Chem. Sci.* **2018,** *9* (1), 143-151.

18. Chen, X.; Ren, H.; Peng, W.; Zhang, H.; Lu, J.; Zhuang, L., Highly Efficient Molecular Cobalt Electrode for (Photo)electrochemical Hydrogen Evolution. *J. Phys. Chem. C* **2014,** *118* (36), 20791-20798.

19. Abe, T.; Kaneko, M., pH-dependent electrocatalysis for proton reduction by bis(2,2':6',2''-terpyridine) cobalt(II) complex embedded in Nafion membrane. *J. Mol. Catal. A Chem.* **2001,** *169* (1-2), 177-183.

20. Rao, J. M.; Hughes, M. C.; Macero, D. J., Voltammetry of terpyridine and terosine complexes of cobalt(II) and iron(II). *Inorg. Chim. Acta* **1976,** *16*, 231-6.

21. Cao, J.; Elliott, D.; Zhang, W.-x., Perchlorate reduction by nanoscale iron particles. *J. Nanopart. Res.* **2005,** *7* (4-5), 499-506.